Advanced covalent ceramics from organosilicon polymers for sustainable energy and environment

by

Shakir Bin Mujib

B.Sc., Bangladesh University of Engineering and Technology, 2015

AN ABSTRACT OF A DISSERTATION

submitted in partial fulfillment of the
requirements for the degree

DOCTOR OF PHILOSOPHY

Alan Levin Department of Mechanical and Nuclear Engineering
Carl R. Ice College of Engineering

KANSAS STATE UNIVERSITY
Manhattan, Kansas

2022

Abstract

Controlled thermal degradation of the liquid-phase polymers of molecular precursor-derived ceramics offer them excellent engineering properties. Amorphous ceramic phase and resistance to crystallization up to 1400 °C, high-temperature stability, and intense photoluminescence are some of the remarkable functional properties of these polymer-derived ceramics (PDCs). The ever-increasing demand of high-temperature components to increase the performance efficiency in aerospace applications pushes the industry to look for a new class of materials. Simultaneously, investigations of renewable energy sources lead to the development of efficient energy storage materials. PDC route offers a promising solution to both of these applications owing to PDC's distinct production route and functional properties.

This dissertation focuses on two aspects. Firstly, the use of silicon-based PDCs to fabricate lightweight and strong ceramic matrix composites for high-temperature applications. The efficient infiltration of carbon fibers cloths (disks) and mini-bundles with boron-modified polysilazane and hafnium-modified polysilazane preceramic polymer solutions were investigated using a lab-scale, cost-effective drop coating technique. After the successful infiltration of the fibers was confirmed, the infiltrated fibers were heat-treated at different temperatures to complete the polymer-to-ceramic conversion of the preceramic polymer matrix. The boron-modified polysilazane and hafnium-modified polysilazane coated carbon fibers were crosslinked at 180 °C, followed by pyrolysis at 800 °C in inert environments to achieve Si(B)CN/CF and Si(Hf)CN/CF CMC mini-composites, respectively. Crack and defect free ceramic matric composites were achieved. The as-fabricated mini-composites were then investigated by several techniques to determine the composites' micro-structures and properties. The effect of the boron and hafnium in the polymer-derived ceramic matrices

and micro-structural development of the final ceramic composites were characterized using scanning electron microscopy (SEM), Raman spectroscopy, Fourier-transform infrared spectroscopy (FTIR), and X-ray photoelectron spectroscopy (XPS). The Raman and FTIR spectroscopies showed the complete conversion of the polymer to ceramic phase. The elemental composition and distribution of chemical bonds in the final mini-composites were determined by XPS. The mechanical properties of the mini-composites were investigated by tensile tests. Room-temperature tensile tests showed that the Si(Hf)CN/CF sample could reach a tensile strength of 790 MPa and elastic modulus of 66.88 GPa among the composites. To determine the high-temperature stability the oxidation behavior at various temperatures were studied. The oxidation study of the mini-composites showed stability of the samples up to 1500 °C. Structural and compositional changes of the oxidized samples were also elaborately investigated by XPS and SEM analyses to understand the phase change after oxidation.

Secondly, the application of PDCs as free-standing, high capacity electrode materials for energy storage systems. Various preceramic polymer solutions were investigated to fabricate anode materials for lithium-ion batteries. Electrospinning technique was utilized to fabricate free-standing fiber mats from three different siloxanes oligomers. To achieve electrospun fiber mats, the short-chain siloxane oligomers were needed to be mixed with and additional spinning agent such as polyvinylpyrrolidone (PVP). The electrospun fiber mats were then crosslinked at 180 °C and pyrolyzed at 800 °C in Ar environment to obtain three types of SiOC ceramic fiber mats. The electron microscopy of the PDC fiber samples showed rigid surface structures with small diameters in the range of 0.2-3 µm. Raman, FTIR, XPS, and NMR spectroscopies were utilized to outline the ceramization stages of the SiOC fibers. 29Si MAS NMR spectra of the SiOC fibers revealed that mostly SiO4 bonds were formed in the amorphous ceramic phase, which indicated the formation on free carbon phase with limited amount of Si-C bonds after pyrolysis. The higher amount of free carbon along with the Si-O-C mixed bonds in the amorphous SiOC samples enabled high lithium reversibility. As a result, when utilized as LIB electrodes, the self-supporting SiOC fiber mats showed excellent specific capacity of 866 mAh $g^{-1}_{electrode}$ with a high coulombic efficiency of 72%. Even as

supercapacitor electrode, the SiOC fibers maintained 100% capacitance retention over 5000 cycles at a high current density of 3 A g^{-1}.

These two approaches for the synthesis of CMC mini-composites and electrode components using PDC materials offer promising potential for the various PDC chemistries to be utilized for both high-temperature and energy storage applications.

Advanced covalent ceramics from organosilicon polymers for sustainable energy and environment

by

Shakir Bin Mujib

B.Sc., Bangladesh University of Engineering and Technology, 2015

A DISSERTATION

submitted in partial fulfillment of the
requirements for the degree

DOCTOR OF PHILOSOPHY

Alan Levin Department of Mechanical and Nuclear Engingeering
Carl R. Ice College of Engineering

KANSAS STATE UNIVERSITY
Manhattan, Kansas

2022

Approved by:

Major Professor
Dr. Gurpreet Singh

Copyright

Abstract

Controlled thermal degradation of the liquid-phase polymers of molecular precursor-derived ceramics offer them excellent engineering properties. Amorphous ceramic phase and resistance to crystallization up to 1400 °C, high-temperature stability, and intense photoluminescence are some of the remarkable functional properties of these polymer-derived ceramics (PDCs). The ever-increasing demand of high-temperature components to increase the performance efficiency in aerospace applications pushes the industry to look for a new class of materials. Simultaneously, investigations of renewable energy sources lead to the development of efficient energy storage materials. PDC route offers a promising solution to both of these applications owing to PDC's distinct production route and functional properties.

This dissertation focuses on two aspects. Firstly, the use of silicon-based PDCs to fabricate lightweight and strong ceramic matrix composites for high-temperature applications. The efficient infiltration of carbon fibers cloths (disks) and mini-bundles with boron-modified polysilazane and hafnium-modified polysilazane preceramic polymer solutions were investigated using a lab-scale, cost-effective drop coating technique. After the successful infiltration of the fibers was confirmed, the infiltrated fibers were heat-treated at different temperatures to complete the polymer-to-ceramic conversion of the preceramic polymer matrix. The boron-modified polysilazane and hafnium-modified polysilazane coated carbon fibers were crosslinked at 180 °C, followed by pyrolysis at 800 °C in inert environments to achieve Si(B)CN/CF and Si(Hf)CN/CF CMC mini-composites, respectively. Crack and defect free ceramic matric composites were achieved. The as-fabricated mini-composites were then investigated by several techniques to determine the composites' micro-structures and properties. The effect of the boron and hafnium in the polymer-derived ceramic matrices

and micro-structural development of the final ceramic composites were characterized using scanning electron microscopy (SEM), Raman spectroscopy, Fourier-transform infrared spectroscopy (FTIR), and X-ray photoelectron spectroscopy (XPS). The Raman and FTIR spectroscopies showed the complete conversion of the polymer to ceramic phase. The elemental composition and distribution of chemical bonds in the final mini-composites were determined by XPS. The mechanical properties of the mini-composites were investigated by tensile tests. Room-temperature tensile tests showed that the Si(Hf)CN/CF sample could reach a tensile strength of 790 MPa and elastic modulus of 66.88 GPa among the composites. To determine the high-temperature stability the oxidation behavior at various temperatures were studied. The oxidation study of the mini-composites showed stability of the samples up to 1500 °C. Structural and compositional changes of the oxidized samples were also elaborately investigated by XPS and SEM analyses to understand the phase change after oxidation.

Secondly, the application of PDCs as free-standing, high capacity electrode materials for energy storage systems. Various preceramic polymer solutions were investigated to fabricate anode materials for lithium-ion batteries. Electrospinning technique was utilized to fabricate free-standing fiber mats from three different siloxanes oligomers. To achieve electrospun fiber mats, the short-chain siloxane oligomers were needed to be mixed with and additional spinning agent such as polyvinylpyrrolidone (PVP). The electrospun fiber mats were then crosslinked at 180 °C and pyrolyzed at 800 °C in Ar environment to obtain three types of SiOC ceramic fiber mats. The electron microscopy of the PDC fiber samples showed rigid surface structures with small diameters in the range of 0.2-3 µm. Raman, FTIR, XPS, and NMR spectroscopies were utilized to outline the ceramization stages of the SiOC fibers. 29Si MAS NMR spectra of the SiOC fibers revealed that mostly SiO4 bonds were formed in the amorphous ceramic phase, which indicated the formation on free carbon phase with limited amount of Si-C bonds after pyrolysis. The higher amount of free carbon along with the Si-O-C mixed bonds in the amorphous SiOC samples enabled high lithium reversibility. As a result, when utilized as LIB electrodes, the self-supporting SiOC fiber mats showed excellent specific capacity of 866 mAh $g^{-1}_{electrode}$ with a high coulombic efficiency of 72%. Even as

supercapacitor electrode, the SiOC fibers maintained 100% capacitance retention over 5000 cycles at a high current density of 3 A g^{-1}.

These two approaches for the synthesis of CMC mini-composites and electrode components using PDC materials offer promising potential for the various PDC chemistries to be utilized for both high-temperature and energy storage applications.

Table of Contents

List of Figures

List of Tables

Acknowledgments

First of all, I would like to thank my thesis advisor, Prof. Gurpreet Singh, for his continuous support, patience and guidance throughout my Ph.D. work. I am grateful for his mentorship and inspiration over the last four years.

I would like thank Prof. Christel Gervais from Sorbonne Université for her support in NMR experiments and data analysis. I also would like to express my gratitude to the following researchers for providing training on the following characterization instruments; from University of Kansas: Dr. Charles Ye (FTIR and Raman); from University of Nebraska, Lincoln: Dr. Balamurugan Balasubramanian (XPS); Dr. Xingzhong Li (HRTEM), and from Kansas State University: Dr. Dan Boyle (TEM).

Financial support from National Science Foundation (NSF) Partnerships for International Research and Education (PIRE) grant number 1743701 is gratefully acknowledged. The research was performed in part in the Nebraska Nanoscale Facility: National Nanotechnology Coordinated Infrastructure and the Nebraska Center for Materials and Nanoscience (and/or NERCF), which are supported by the National Science Foundation under Award ECCS: 2025298, and the Nebraska Research Initiative.

I am thankful to my former and current lab colleagues Dr. Zhongkan Ren, Dr. Davi Marcelo Soares, Sonjoy Dey and Mohammed Rasheed for their valuable assistance during my Ph.D. work.

Thanks to my parents, sisters, and in-laws for continuously loving and supporting me during my Ph.D. work no matter how far I am from them. Finally, I would like to thank my wife Noushin Afrin and my daughter Rosabella Mujib for their endless love and encouragement.

Dedication

I dedicate this thesis to my wife, Noushin, who has been a constant source of support and encouragement during the challenges of graduate school and life. This work is also dedicated to my daughter, Rosabella, who has been a little bundle of continuous joy since she came to our life.

Chapter 1

Introduction and motivation

One of the major concerns of the aerospace industries now-a-days is finding new materials that can withstand operational temperatures above 1500 °C while maintain the structural integrity of the vehicle. Enabling higher operational temperatures will allow the engine to have increased fuel efficiency. High heat flux in leading edges and high pressure are faced in hypersonics[1]. The temperature in these edges sometimes go over 2200 °C, which are not sustainable for the current metal alloys. As a result, scientists are pushed to review other classes of materials that can meet the thermal and structural needs of the next generation aerospace applications. Composites made with ceramic matrix can be used under high-temperature and high-pressure due to the composites' specific properties related to high-temperature resistance, high mechanical strength, resistance to corrosion, and especially thermal stability for a prolonged period time. These ceramic matrix composites (CMCs) are being considered for high-temperature environments of aerospace applications such as turbine engines, atmospheric reentry vehicles, rocket nozzles, hypersonics, etc.[1–4]. Having lightweight structure while maintaining the mechanical strength make CMCs promising class of materials for these applications.

Concurrently, energy storage technologies are critical in the sense that they are used to power an application, such as electronic devices, electric vehicles, or electric grid energy storage systems. Electrochemical energy devices utilize reversible energy storage, in which

chemical energy is converted into electrical energy and vice-versa and then repeated hundreds or thousands of times. Beyond traditional lithium-ion technology, a new generation of affordable, innovative, and lightweight battery systems will find their way into the ever-advancing era of cellphones, tablets, and laptops. Electric vehicles are going to replace the fuel power with batteries and supercapacitors to achieve better distance/amount of energy, resulting in cost-effective driving. Powerful batteries will completely revolutionize grid energy storage (e.g., customizable microgrids), and may permanently change the fundamental operation of the energy supply system. However, these ground-breaking innovations require high-performance, low-cost energy storage technologies. Following the replacement of fossil fuels with wind, solar, and stored energy, traditional lithium technologies must evolve to include electrode materials with exceptional properties as well as other charged alkali ions. Researchers have demonstrated how ceramics that are derived from polymeric precursors can provide the necessary boost toward the next-generation electrochemical energy storage.

In the early 1960s, an unusual polymer-to-ceramic conversion was used to develop silicon-based ceramic from organosilicon polymers that were denoted as polymer-derived ceramics (PDCs)[5]. Small-diameter silicon carbide-based ceramic fibers were produced, practical application of this ceramic processing route via thermolysis. Notable examples of polymer-to ceramic transformation technology include films/coatings, fibers, bulk ceramics, and non-oxide ceramics, which are all synthesized with tailored properties. PDCs offer high thermodynamic/chemical stability against electrochemical corrosion, good mechanical strength, tunable electrical conductivity and porosity and multiple sites in PDC microstructure for reversible alkali metal-ion storage, which qualify them as exceptional electrodes for electrochemical storage systems. Depending on the application, PDCs can be shaped into any desirable morphology, size, and structure, making them viable even for textile/wearable energy storage devices. On the other hand, it is nearly impossible to acquire a high-performance electrode from just a single class of material as most have only one or a few of the desired properties.

Polymer-derived ceramics (PDCs) are a class of high-temperature materials synthesized by an attractive route of thermal decomposition of polymeric precursors. Properties of PDCs

superior to conventional ceramics include a relatively lower fabrication temperature, lower degree of impurity, homogeneous disposition of the constituent elements, and relatively lower cost of fabrication[6–8]. Wide range of precursors and varying process conditions enable PDCs to be synthesized with controlled compositions and molecular structures. Programming the synthesis conditions for PDCs to engineer the functional properties of PDCs is an important feature of these materials.

Processing techniques plays a key role in achieving high performance CMCs. Also, price of the constituents (i.e., reinforcement and matrix) and processing time have an important part in determining the feasibility of the CMCs for high-temperature applications. As such, traditional ceramic processing techniques such as hot pressing, reaction sintering, powder sintering, etc. are not suitable[9]. The reinforcement materials, for example fibers, get physically and chemically damaged during these fabrication techniques of CMCs. To protect the fibers from degradation PDCs can be employed. The temperature-induced ceramization process of PDCs enable tuning microstructures of the ceramics which are not possible with the traditional ceramization techniques. The amorphous ceramic phase of the PDCs is thermally stable at very high-temperatures. Besides, the fabrication process of CMCs using PDCs can be cost-effective and use less-corrosive materials compared to tradition processes.

Previous works mainly focused on the basic knowledge of PDCs such as chemical and physical changes during the polymer-to-ceramic transformation process, the various properties such as mechanical and thermal properties, and the structures of ultimate ceramics. However, understanding the electrochemical energy storage properties of PDCs, especially Si-based PDCs, and their correlation with the molecular and electronic structures has received lesser attention. A thorough understanding of electronic behavior of PDCs will be critical for the synthesis and application of PDCs. In this work, the structures, mechanical and electrochemical behavior of polymer-derived SiCN, Si(B)CN, Si(Hf)CN, and SiOC ceramics were studied.

In summary, this Ph.D. thesis discusses on the following aspects: Chapter 2 provides a detailed literature review of the relevant areas of research and applications of PDCs in CMCs and energy storage systems. Chapter 3 details fabrication process and structural evolution

of thermally stable Si-based PDCs, namely SiCN, Si(B)CN, and Si(Hf)CN, -coated carbon fibers composites also known as ceramic matrix composites (CMCs). Chapter 4 focuses on the mechanical and electrochemical properties of these CMCs. Chapter 5 presents fabrication process and structural evolution of thermally stable SiOC fibers synthesized from three different types of polymeric precursors. Chapter 6 provides a comparative discussion on the mechanical and electrochemical properties of these SiOC fibers mentioned in Chapter 5. Lastly, concluding remarks are listed in Chapter 7. Future directions are discussed as well at the end of Chapter 7.

Chapter 2

Background and literature review

2.1 Polymer-derived ceramics (PDCs)

The polymer-derived ceramic (PDC) approach is an advanced ceramic manufacturing technique that designs or controls molecular structures of ceramic products at molecular or atomic levels[6]. Over the last 30 years there's been a significant increase in PDC-related research including PDCs for high-temperature applications[10]. PDCs synthesis route is unique as it not possible to achieve amorphous phase in ceramics using conventional ceramic synthesis techniques, such as powder sintering or chemical vapor deposition (CVD)[8]. The polymer structure converts to amorphous microstructure in PDCs during pyrolysis with nanodomains ranging from 1 to 3 nm, that corresponds to superior oxidation and creep resistance up to 1500 °C. Besides, PDCs low impurity level and homogenously distributed elements greatly improve the oxidation and creep resistance of PDCs at elevated temperature[11]. In addition, by chemically modifying the polymeric precursors and or tailoring process conditions during the polymer-to-ceramic conversion the properties of PDCs can be controlled over a wide range[12].

2.1.1 Polymer precursors

Common preceramic polymers for the synthesis of Si-based PDCs include polysilane, polycarbosilane, polysiloxanes, polysilazane, polysilycarbodiimides, etc. Since the report by Yajima et al. to synthesize silicon carbide (SiC) form polycarbosilane[5], significant developments in the PDC synthesis have been achieved[8;13;14]. Therefore, complex-shaped ceramics such as fibers, coatings or porous powders can be attained form silicon-based precursors or preceramic polymers[15].

The type of preceramic polymers and their molecular structures greatly influence the composition or phase distribution as well microstructure of the final ceramic product. Thus, preceramic polymers should possess certain properties in order to achieve successful thermal decomposition into ceramics. A relatively high molecular weight of polymers can prevent volatilization of the low molecular components; suitable viscosity or rheological properties maintains the solubility thus helps in achieving desired shapes; and latent reactivity such as presence of functional groups in polymer precursors contributes to the successful cross-linking and curing process[8].

The general representation of the Si-based preceramic polymers (organosilicon polymers) is depicted in the following formula:

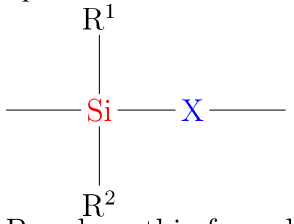

Based on this formula, two parameters can be adjusted chemically for Si-based PDCs: Firstly, X-group in the formula represents the group of the polymer backbone, which can be carbon (C), oxygen (O), nitrogen (N), or boron (B). Changing the X-group results in new classes of organosilicon polymers, for instance, X = Si correspond to poly(organosilanes), X = O poly(organosiloxanes), and X = N results in poly(organosilazanes). Secondly, R^n represents the side groups. These organic side groups plays an important role in solubility, chemical and thermal stability, as well as rheological, optical, and electronic properties of the polymers[16].

A simplified formula chart for the different classes of organosilicon polymers is shown in Figure 2.1. In this thesis, emphasis is given to silicon carbonitride (SiCN) and silicon oxycarbide (SiOC) ceramics, which when in polymer form corresponds to polysilazanes and polysiloxanes, respectively.

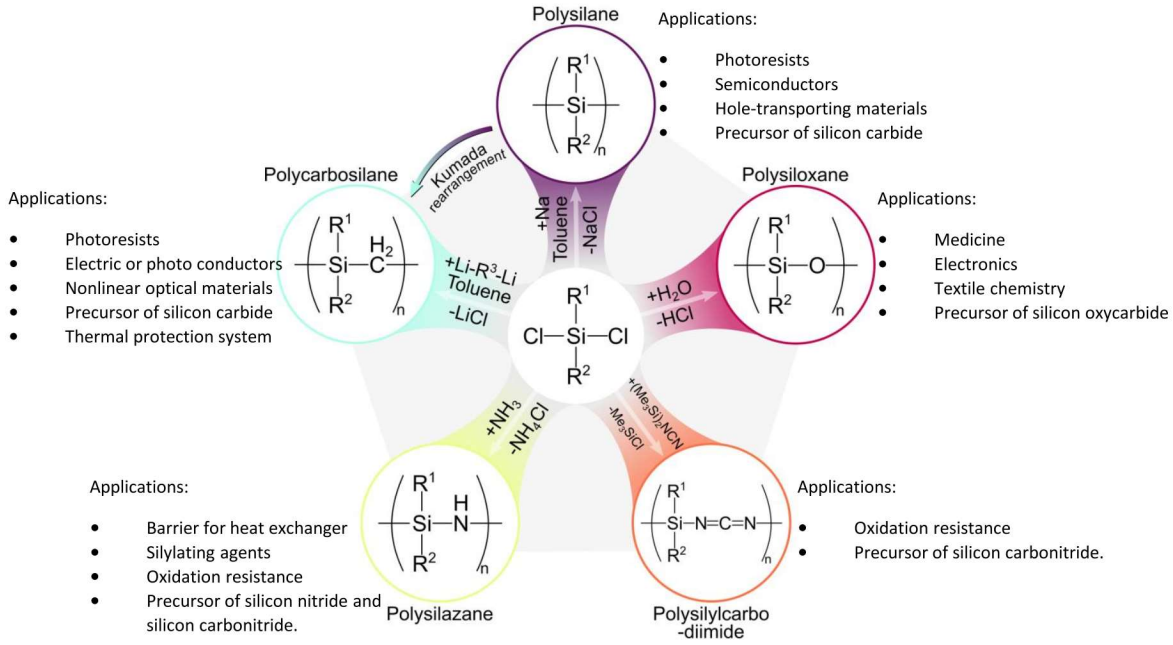

Figure 2.1: *Examples of common families of Si-based preceramic polymer, their fundamental chemical units and applications. (R^1 or R^2 = H, CH_3, $CH{=}CH_2$, etc.). Adapted from*[17].

2.1.2 Polymer-to-ceramic conversion

The polymer-to-ceramic conversion consists of two steps: (i) Cross-linking of the polymers at low temperatures (100-400 °C) leading to infusible organic/inorganic networks and, (ii) Ceramization via pyrolysis at temperatures >800 °C. Typically, upon pyrolysis amorphous ceramics are obtained, however, subsequent annealing at higher temperatures can result in (poly)crystalline materials[14]. The crosslinking process prevents the loss of low molecular weight components of the preceramic polymers and also their defragmentation during pyrolysis. In addition, conversion of preceramic polymers into infusible networks prohibits their melting during ceramization while retaining the shape of crosslinked polymers. The general

PDC synthesis processes are presented in Figure 2.2.

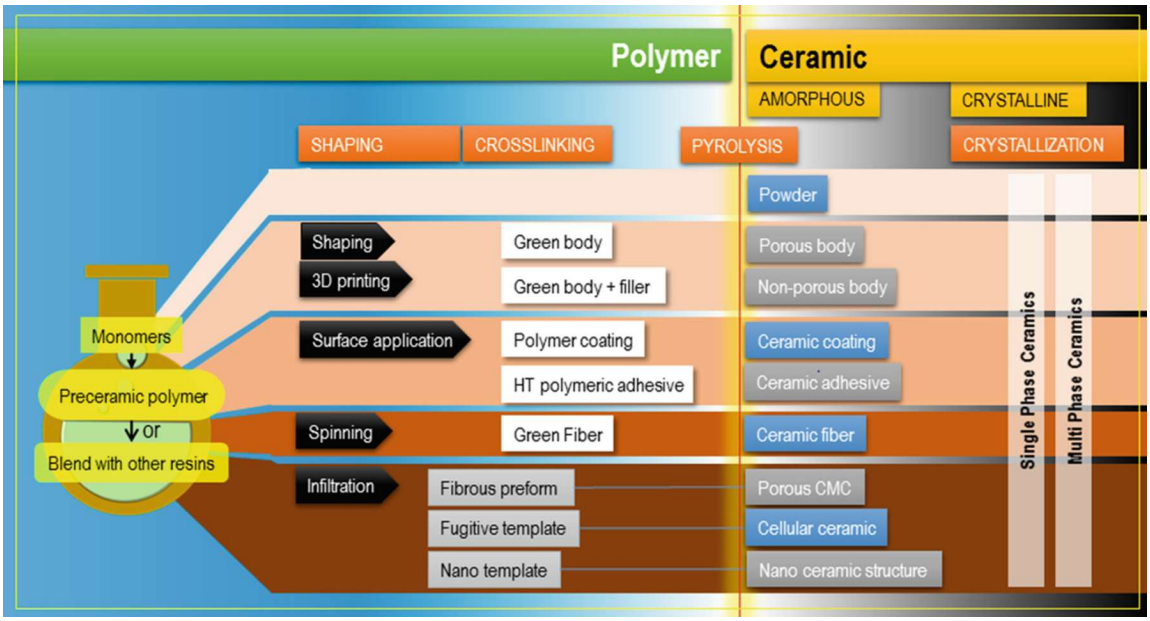

Figure 2.2: *Schematics of PDC processing route. The shaping of the preceramic polymer occurs at the crosslinking stage by thermal crosslinking usually at 100-400 °C. Organic to inorganic transition is completed at the thermal pyrolysis stage at elevated temperatures typically around 1000 °C. Reproduced with permission from*[18]*. Copyright 2020 Springer Nature Switzerland AG.*

Polysiloxanes are preceramic polymers which can be used for the synthesis of silicon oxycarbide-based ceramics upon thermal decomposition in an inert gas atmosphere[8]. In case of polysiloxanes, polymers that contain methyl or vinyl groups crosslinking is initiated thermally in the presence of peroxide. The reactions happen between the silicon-hydride (Si-H) groups and silicon-vinyl (Si-vinyl) groups. This reaction is known as hydrosilylation. For polysiloxanes, which contain alkoxy or hydroxy groups, crosslinking can be achieved via condensation of Si-OH units and in-situ hydrolysis of alkoxy groups that results in Si-O-Si bonds[14].

Polysilazanes can be cross-linked either thermally or using chemical reagents, such as catalysts and peroxides[13]. There are four major reactions that can initiate the thermal crosslinking process of polysilazanes: (i) hydrosilylation, (ii) vinyl polymerization, (iii) transamination and (iv) dehydrocoupling (Si-H/Si-H or Si-H/N-H)[12]. Hydrosilylation of polysilazanes occurs in between Si–H and vinyl groups. Dehydrocoupling reactions results in the formation

of Si–N and Si–Si bonds start at higher temperatures (typically 300 °C). Transamination processes occur at temperatures approximately from 200-400 °C and are associated with a mass loss (such as evolution of amines, ammonia or oligomeric silazanes) and lead to a decrease of the nitrogen content in the ceramic materials upon pyrolysis. The vinyl polymerization (addition) process occurs at higher temperatures (>300 °C) and involves no mass loss.

The ceramization process of the cross-linked precursors consists of the thermolysis and evolution of the organic polymers (Figure 2.2) at higher temperature of 600-1000 °C[12]. Due to the amorphous nature of the preceramic polymers as well as the subsequent amorphous ceramics, it is difficult to determine the mechanisms involved during ceramization of the precursors. However, utilization of different in-situ spectroscopic techniques such as RAMAN, FTIR, and solid-state NMR can shed some light into the complex reactions occurring during pyrolysis of preceramic polymers[8].

High-temperature (usually >1100 ∘C) environments cause the crystallization of amorphous SiCN with microstructures of mixed SiN_4-xC_x silicon tetrahedrons[19] and segregation into thermodynamically stable crystalline microstructures (e.g., SiC, Si_3N_4, C, or Si) at higher temperatures[20]. Incorporating other elements, such as B[20–23], Al[24–26], Nb[27], Zr[28–30], Ti[31;32], or Hf[23;33–35], in the Si-C-N or Si-O-C systems may greatly enhance the thermostability of ceramic products by preventing or impeding the crystallization and phase segregation of the ceramic phases in inert or oxidizing environments[8]. Initially, at the crosslinking stage, B atoms may improve the formation of the crosslinking network and increase the yield and structural density of Si(B)OC[22;23]. Upon polymer-to-ceramic conversion, doped elements may form additional phases (e.g., TiO_2, HfO_2, ZrO_2) and lead to nanocomposite-like structures of metal-oxide/amorphous ceramics[36] or dissolve into and alter the amorphous phase (e.g., Si(B)OC, Si(Al)OC) which eventually segregate into additional phases (BN, Al_2O_3) at higher temperatures. At the amorphous stage, the superior stability of the B- or Al-doped amorphous phase significantly enhances the oxidation resistance of Si(B)OC or Si(Al)OC ceramics.

2.2 Ultrahigh-temperature ceramics (UHTCs)

Ceramics are generally non-metallic, inorganic solid materials that were first utilized more than 25,000 years ago[37;38]. Ceramics are the oldest man-made materials such as pots, vessels or figurines made from clay or silica refractories[39]. In fact, the term "Ceramic" was derived from the Greek word "Keramos", which means "Pottery"[40;41]. This term since then has been used for the materials that are manufactured using the traditional ceramic manufacturing process of shaping, drying, and firing. Although, ceramics were traditionally used as structure materials, now-a-days ceramics are utilized in advanced applications such as space shuttle tile, engine components, artificial bone and tooth, etc. due to their functional and high-temperature properties[42].

Figure 2.3: *A 25000 year old Palvovian figurine called the "Venus of Vestonice". It was made with baked clay and discovered in 1920 in Dolni Vestonice of Czech Republic*[40].

Advanced ceramics are engineering ceramics with excellent mechanical, electrical, optical, magnetic properties, and oxidation or corrosion resistance. Developed in the last 100 years, the advanced ceramics are usually comprised of group IIIA or IVA elements of the periodic table, or transition metals (e. g., Ti, Mo, W, Zr) with light elements such as C, N, B, O,

etc.[37]. The wide variety of bonding type including covalent, metallic, ionic or mixed bonds enable the advanced ceramics to have adjustable chemical and physical properties[43;44]. These advanced ceramics are preferred in high-temperature applications due to their extreme heat resistance, chemical inertness, and mechanical strength at high-temperatures. Ultra-high temperature ceramics also known as UHTCs have been explored for potential utilization in aerospace, automotive, defense, and nuclear industries where extreme heat is expected. UHTCs are useful in a high working temperature environment of over 2000 °C, with melting or decomposition temperature greater than 3000 °C[45].

Currently used metal alloys are not able to go above operation temperature of 1500 °C[1]. Monolithic ceramics are stable at high-temperature; however, they are brittle. On the other hand, reinforcing high strength fiber with ceramic matrix interface can withstand the mechanical load at high-temperature. These materials are known as ceramic matrix composites (CMCs), which have exceptional properties of high heat resistance, resistance to corrosion, and lightweight structure.

2.3 Ceramic Matrix Composites (CMCs)

CMCs consists of a ceramic continuous phase, referred to as matrix and a distributed phase referred to as reinforcement[46;47]. Varieties of CMC matrices and reinforcement exist. Introducing different reinforcements such as fibers, fabrics, platelets, whiskers, or particulates into the ceramic matrix contributes to the toughening of CMCs., which prevents sudden crack development and catastrophic failure. Chemical compatibility and properties of the reinforcement and matrix have significant influence on the performance of the CMCs[48]. Different reinforcements have different role in the composites. It is necessary to select the proper reinforcement since catastrophic failure may happen due to lack of toughness and brittle ceramic matrix. *This is one of the scopes of this thesis. One of the purposes of this study is to determine compatible reinforcement and matrix components for fabricating CMCs, which can withstand significant mechanical loading.*

There are different types of fiber architecture currently being developed or used in CMCs.

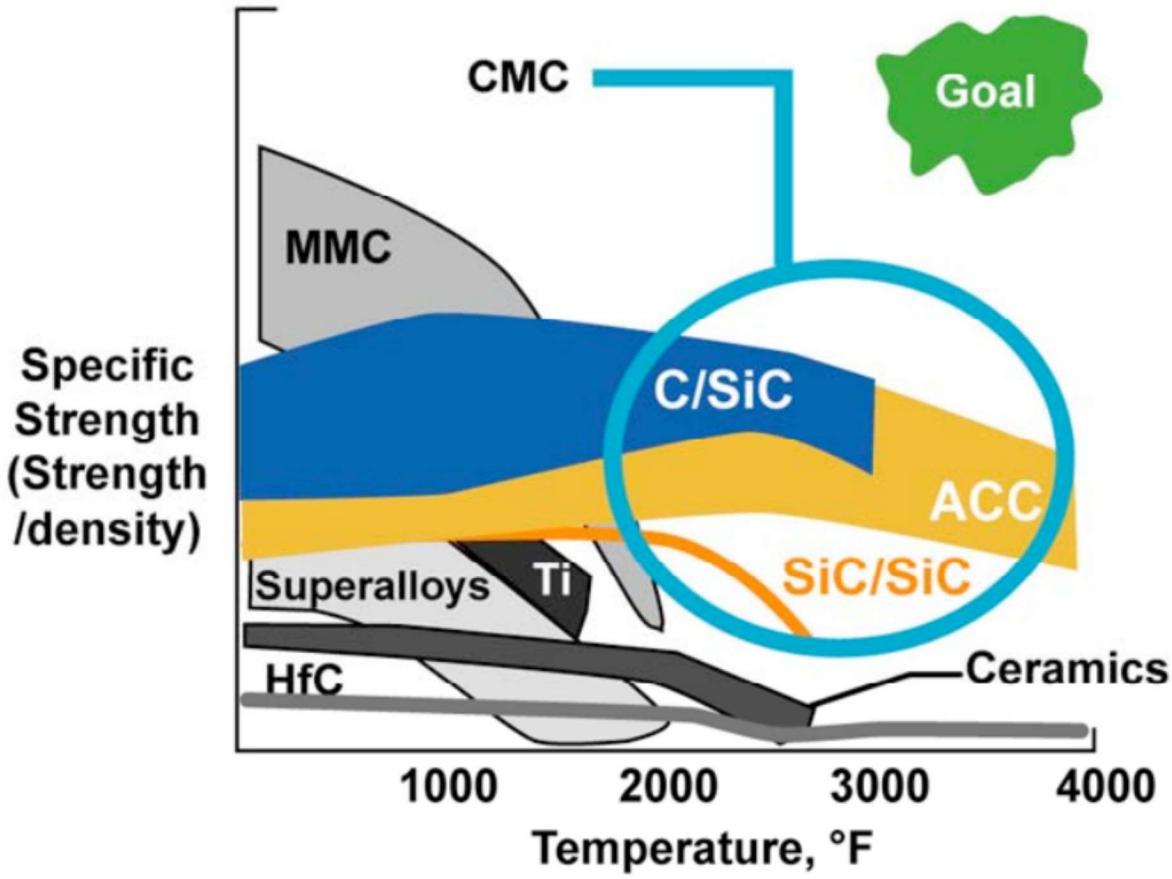

Figure 2.4: *Specific strength of several classes of materials as a function of temperature*[46].

Fiber reinforced ceramic matrix composites are driving the development of the CMCs for high-temperature applications. The fiber/matrix interface plays a crucial role in the crack deflection and composite mechanical behavior. Fiber debonding, fracture, and fiber pull-out are significantly important in governing the toughness of the CMCs. In addition, in case of CMCs, the reinforcement fibers should also have high-temperature stability, creep resistance and oxidation stability.

The common reinforcement fibers for CMCs are carbon, silicon carbide (SiC), alumina (Al_2O_3), as well as glass fibers. Currently available commercial CMCs (fiber/matrix) are: C/C, C/SiC, SiC/SiC, Al_2O_3/Al_2O_3. Continuous fibers are favored more than chopped fibers and whiskers in manufacturing high-temperature CMCs[9;49;50]. Disintegration of fiber phase at higher temperature, inhomogeneous distribution of the fibers due to high aspect

ratio and strong fiber bonding with the matrix interface create difficulties in achieving high-temperature applications for chopped fiber reinforcement[51]. Additional coatings can be used on the fibers to introduce weak fiber/matrix interface; however, this adds more restrictions in manufacturing CMCs in terms of time, cost, and machinability. As a result, using continuous fiber reinforcement remain the most promising approach in manufacturing high-temperature CMCs.

The CMCs was first introduced in 1960s by Crivelli-Visconti and Cooper[52], when they reinforced carbon fibers with pure silica matrix. The authors reported that the large difference in Young's modulus in between carbon fiber and silica matrix assured that greater part of the load will be carried by the fibers. In addition, the thermal expansion co-efficient of the fiber and matrix were in the similar range, which allowed to manufacture the CMC at high-temperature. In this study, it was shown that the weak interface in fiber/matrix bonding provided higher strength and toughness than the strongly bonded fiber/matrix interface. The cracks formed in the well bonded matrix propagated to fibers and weakened the composite. The results reported by this study are presented in Figure 2.5.

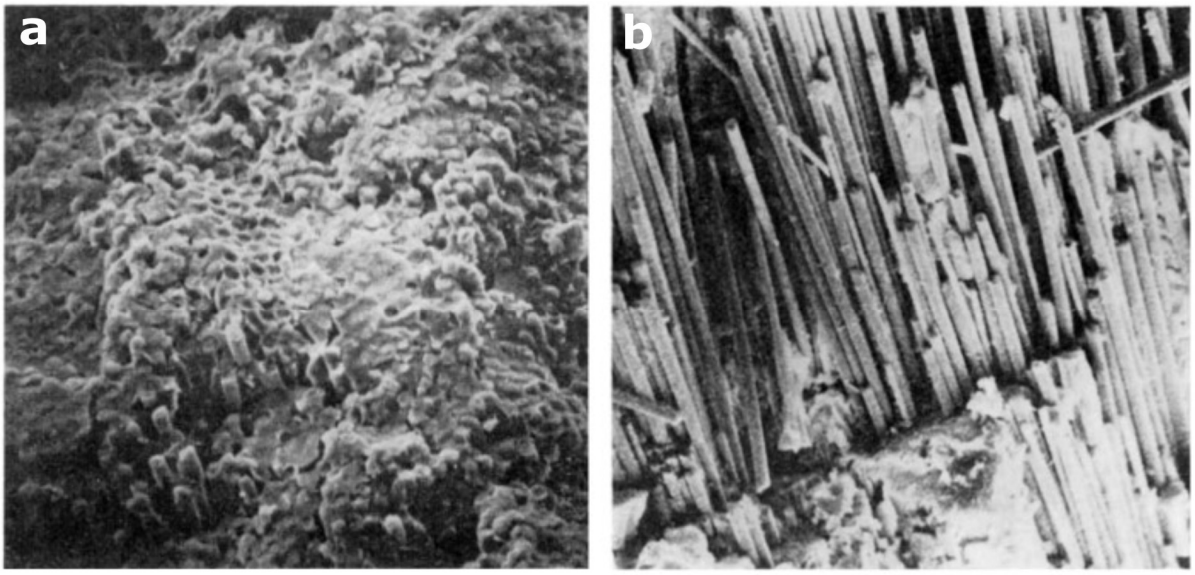

Figure 2.5: *First reported CMCs by Crivelli-Visconti and Cooper. It was shown that CMCs with strong bonding in fiber/matix interface had lower strenght and toughness than the weakly bonded composites. Fracture surface of (a) the strong fiber/matrix interface and (b) weakly bonded fiber/matrix interface*[52].

In 1970s several researchers proposed to strengthen the properties of silicon nitride (Si_3N_4) matrix by reinforcing with the SiC fibers[53–56]. Sambell and Briggs utilized carbon fiber reinforcement with alumina, magnesia, borosilicate glass, lithia alumino-silicate, and soda-lime glass[54;55]. According to this study, mismatch in thermal coefficients of the fiber and matrix resulted in localized matrix cracking, composites with randomly distributed fibers had lower strength than the composites with continuous fibers, and the reinforced ceramics had higher strength at high-temperatures than the ceramics. Later, SiC fibers in glass and SiC matrix were investigated for high temperature applications such as jet engines and reentry vehicles[57;58]. The current areas of the CMC research are focused on the spatial and structural design of the CMCs as well as functional properties and applications such as bearing structures, brake components, and aerothermal structural materials. Some of the major manufacturing processes of CMCs using different infiltration techniques are discussed in the following sections.

2.4 CMC manufacturing techniques

2.4.1 Polymer infiltration and pyrolysis (PIP)

Polymer infiltration and pyrolysis, also known as PIP, is an attractive and efficient technique to fabricate CMCs[59]. A low-viscosity polymer solution is infiltrated into a ceramic reinforcement such as fibers or fabric and then heated in inert environments to covert the polymer into a ceramic. Since liquid polymer is used and pyrolyzed to fabricate ceramic matrix, PDCs are the matrix components in this technique. During the pyrolysis the matrix can experience 20-80% volumetric shrinkage depending on the polymer amount[49]. As a result, multiple infiltration-pyrolysis or PIP cycles might be needed to achieve the desired densification of the matrix in the CMCs.

The advantages of PIP are that ceramic matrices can be formed at relatively lower temperatures and matrix composition and microstructures can be controlled[60]. A wide range of matrix material may be fabricated, and the low-temperature synthesis process may lower

fiber damage. PIP is mainly used to fabricate composites with Si-based ceramic matrices such as SiC, Si_3N_4, SiCN, etc.[61–64]. However, multiple PIP cycle may increase fabrication time and cost. The presence of porosity in the matrix also affects the mechanical strength of the composites. *This is another scope of this thesis study, where a thin coating of preceramic polymer solutions is applied to the carbon fiber reinforcement to avoid long fabrication time and cost and reduce the cracks in the ceramic matrix. The absence of large cracks in the matrix provides sufficient strength to the composites and prevents the fibers from being exposed to extreme heat during oxidation tests.*

In 1990s, Donato et al. patented the liquid infiltration of ceramic polymeric precursors to produce CMCs[65]. They described the process of repeated infiltration large fiber cloths with preceramic polymers to achieve high density CMC, preferably SiC/SiC. Since then a wide range of research has been published on the PIP process to manufacture CMCs. Single-source precursor synthesis for SiC/HfC_xN_{1-x} has been studied by Wen et al., where they have used polycarbosilane (SMP10) with tetrakis (dimethlamido)hafnium to fabricate Hf-based UHTCs[66]. In another study, Li et al. used Zr-based polymeric precursor to fabricate C/ZrC CMCs for high-temperature applications[67]. PIP process are attractive due to the possibility of producing large-size, complex and lightweight structures that can withstand above 1000 °C. Specially, C/SiC composites produced by PIP are suitable for thermal protection systems (TPS) and propulsion components in aerospace technologies. Figure 2.6 shows test of C/SiC subscale nozzle extensions and combustion chambers manufactured by Astrium Company[2;3]. These components were fabricated for a Ariane 5 main engine Vulcain, using PIP process and tested for high-temperature applications at different conditions.

2.4.2 Reactive melt infiltration (RMI)

In reactive metal infiltration (RMI) process, molten metals or metal alloys are used to infiltrate porous preform reinforcement and upon reactions a ceramic phase is created[68;69]. The porous preforms are usually densified before using either CVD or slurry impregnation[49;70]. This is done to introduce skeleton for the metal infiltration. Contact angle between the

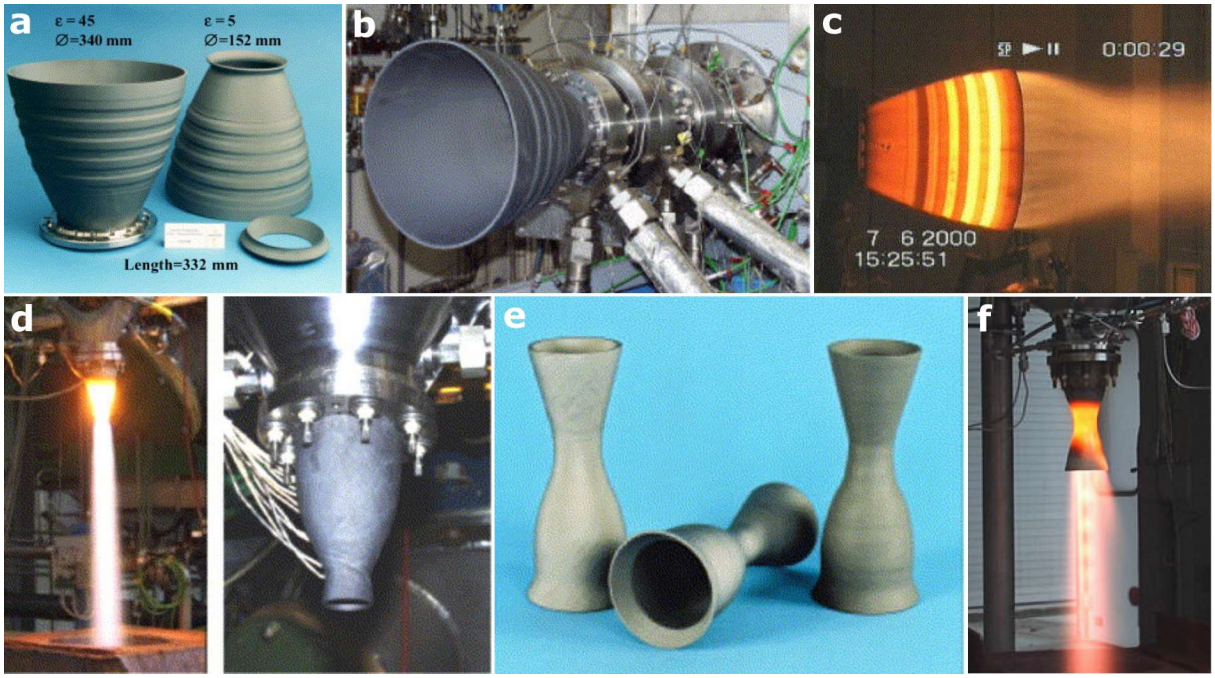

Figure 2.6: *Examples of PIP-derived C/SiC composite nozzle extensions and combustion chamber. (a) Vulcain subscale (1:5) C/SiC nozzle extensions manufactured by PIP process. (b) Vulcain subscale nozzle on test bench in Ottobrunn. (c) Vulcain subscale nozzle during 40 bar hot-firing test. During the hot-firing test, temperatures up to 2300K were measured on the hot-gas side by means of thermography. (d) C/SiC combustion chamber during the hot-firing test. Maximum wall temperatures of up to 1700 °C were determined. (e) Modified C/SiC combustion chambers coated with different layers. (f) Modified C/SiC combustion chamber during the hot-firing test. The test time amounted to 5700 s in a combustion-chamber pressure of 11 bars. Adapted from*[2].

molten metal and preform, metal viscosity, surface tension and high capillary force are necessary for successful infiltration[71;72].

Several RMI process has been reported to fabricate UHTCs. According to Schulte-Fischedick et al.[73], silicon melt can diffuse through the already formed SiC. Several nucleation sites are formed when silicon melt reacts with carbon, which contributes to the formation of fine-grained SiC structure. Upon reacting with the carbon Usually, ZrC, ZrB_2, Zr_2Cu, Si-Hf alloy, Si-Ti alloy based molten metals are used for the RMI[69;74;75]. For example, Kutemeyer et al. used Zr-based intermetallic compound with boron powder to infiltrate carbon fibers, which were partially densified with polycarbosilane precursor[?] . Kubota et al. fabricated a ZrB_2/SiC/ZrC matrix using a molten silicon infiltration[76]. They reported that higher ZrC

content in the sample contributed to higher amount of ZrS_2 in the final ceramic. As a result, samples with ZrS_2 phase showed improved performance at a high-temperature of 1800 °C.

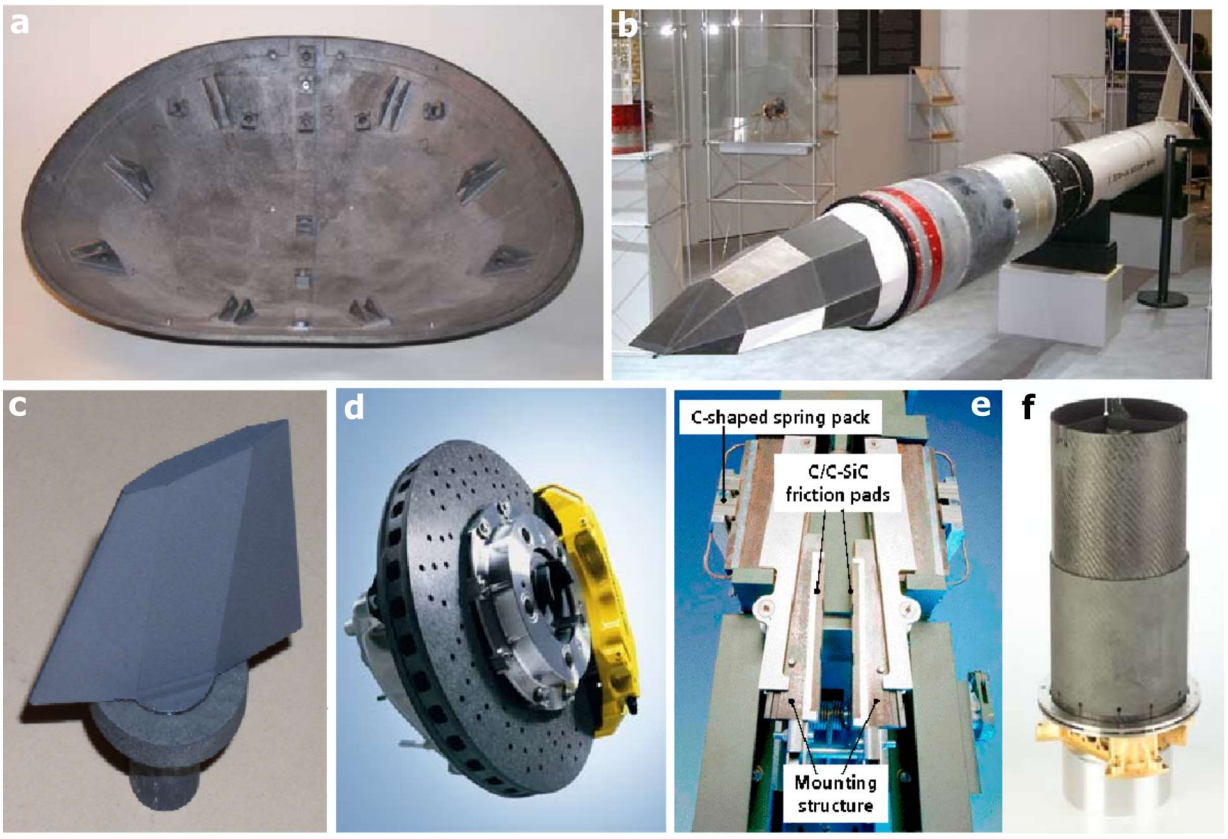

Figure 2.7: *Examples of carbon fiber reinforced SiC composites manufactured by RMI technique. (a) A C/SiC Nose cap (ca. 740 x 640 x 170 mm³; t ca. 6 mm; m ca. 7 kg, DLR) for X 38 aircraft. Rear side showing in situ joint load bearing elements. (b) Facetted C/SiC TPS structure, built up by flat panels, mounted on a rocket system. (c) Jet vane and sealing ring for thrust vector control of missiles. (d) Porsche Ceramic Brake Disk (PCCB) based on C/SiC composite. (e) Emergency brake system foe elevators made with C/C-SiC brake pads. (f) In-situ joint telescope tube for the laser communication terminal in the satellite TerraSAR-X manufactured by Zeiss Optroniks. Adpated from*[77].

The advantages of RMI are that the process is cost-effective, require short period of time and composites may have high thermal conductivity (40 W/mK). However, there are also some drawbacks such as high-temperature of the infiltration process may damage the fibers, presence of residual Si in the matrix, low mechanical strength, and modulus of the composites, etc.

2.4.3 Chemical vapor infiltration (CVI)

A gaseous chemical precursor is infiltrate into a fiber preform in chemical vapor infiltration (CVI) process. The fiber preform is heated usually at temperatures above 800 °C in a furnace, where the fiber is exposed to precursor gas[78]. The precursor gas vapor usually contains a mixture of H_2 and hydrocarbon such methyltrichlorosilane (CH_3SiCl_3) for SiC ceramic matrix. It is necessary to ensure the penetration of gas into the inner layers of the preform. In the CVI process, the diffusion rate is controlled by controlling the temperature and pressure of the process[79]. In case of SiC, volume ratio of H_2 to CH_3SiCl_3 plays a role in the infiltration as well. In lower temperatures and pressures, a higher ratio of H_2 to CH_3SiCl_3 is required to achieve stoichiometric SiC infiltration[80].

CVI-derived SiC matrix can withstand temperatures over 2300 °C in vacuum or inert environment[51–56]. Other studies have reported using carbide phases such ZrC, HfC and TaC as the precursor gas for CVI[81;82]. One study report to have used radio frequency CVI (RF-CVI) to infiltrate a partially dense carbon fiber preform with pyrolytic carbon[83]. The preform was partially densified with vacuum infiltration of ZrB_2. Achieving a uniform distribution of precursor vapor in the center and surface of the preform is essential. That's why, CVI process is sometimes followed by other infiltration process such as PIP or RMI. Such an example is shown in Figure 2.10, where a porous C/C composite was first prepared by CVI process and followed by RMI process to manufacture a C/SiC composite. This C/SiC composite was made by NPU in China as aircraft brake material.

2.5 Additive manufacturing of PDCs

Additive manufacturing, specifically, 3D printing has been an attractive technique in recent years to fabricate PDCs due to the technique's ability to control the architecture of the final ceramic product by computer aided design[85;86]. Several 3D printing techniques have been successfully utilized for example stereolithography (SLA), direct ink writing (DIW) and powder-based printing (PB) for the fabrication of PDCs. For example, Eckel et al. used SLA

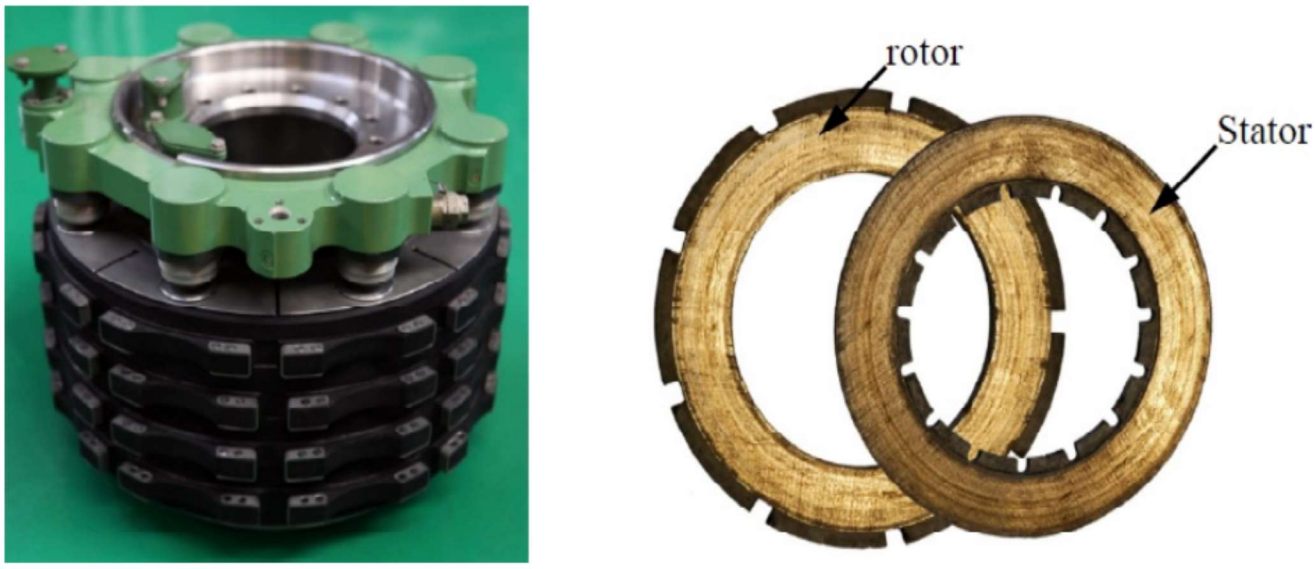

Figure 2.8: *Next-generation C/SiC Brake Materials for aircraft application manufactured using CVI and RMI techniques. Collected from*[84].

to fabricate SiOC ceramic from a mixture of polysiloxanes and free-radical photo initiator[87]. They used SLA to 3D print different complex structures such as honeycomb, corkscrew and then pyrolyzed them at 1000 °C in argon environment to convert into SiOC ceramics. Among the SiOC structures honeycomb showed relatively high compressive strength of 160 MPa and thermal stability up to 1300 °C. For SLA printing, preceramic polymer decides the final ceramic component whereas the photo initiator works as a shape modifier.

In another study, Li et al. introduced digital light processing (DLP) 3D printing technology to manufacture Si(B)CN ceramic structures from polyborosilazane[88]. The printed structures were pyrolyzed at various temperatures and maintained the shape after pyrolysis. The pyrolyzed samples showed minimal weight loss of 0.35% at 1500 °C in air. The Si(B)CN samples also showed a maximum hardness of approx. 8 GPa in the nanoindentation test. Zocca et al. utilized PB technology to 3D print a Kagome structure form polysiloxanes[89]. First the preceramic polymer solution is dried and ball-milled to powder followed by layer-by-layer deposition of the powder to print the structure. Later the green structure was pyrolyzed at 1000 °C to convert it to SiOC ceramic. Pierin et al. manufacture SiOC ceramics via DIW technique from polysiloxanes ink[90]. The ink was derived from polymethyl-

silsexquioxane mixed with silicon resin solid particles to achieve the proper viscosity. After pyrolysis the SiOC structure retained its shape and showed a compressive strength of 2.5 MPa. Franchin et al. showed that DIW could be utilized to fabricate CMC structure[91]. A mixture of preceramic polymer with chopped fibers were used to formulate the ink. The rheology of the ink was controlled by the ratio of fiber to preceramic polymer. It was shown that shear stress generated at the nozzle tip controlled the orientation of the fibers in the printed structure. The pyrolyzed CMC structure showed a porosity of 75% with a compressive strength of 4 MPa. Due to the ease of use and controllability of shapes the organosilicon PDCs show the great potential to be used in 3D printing. Some examples of 3D printed silicon-based ceramics are presented in Figure 2.11.

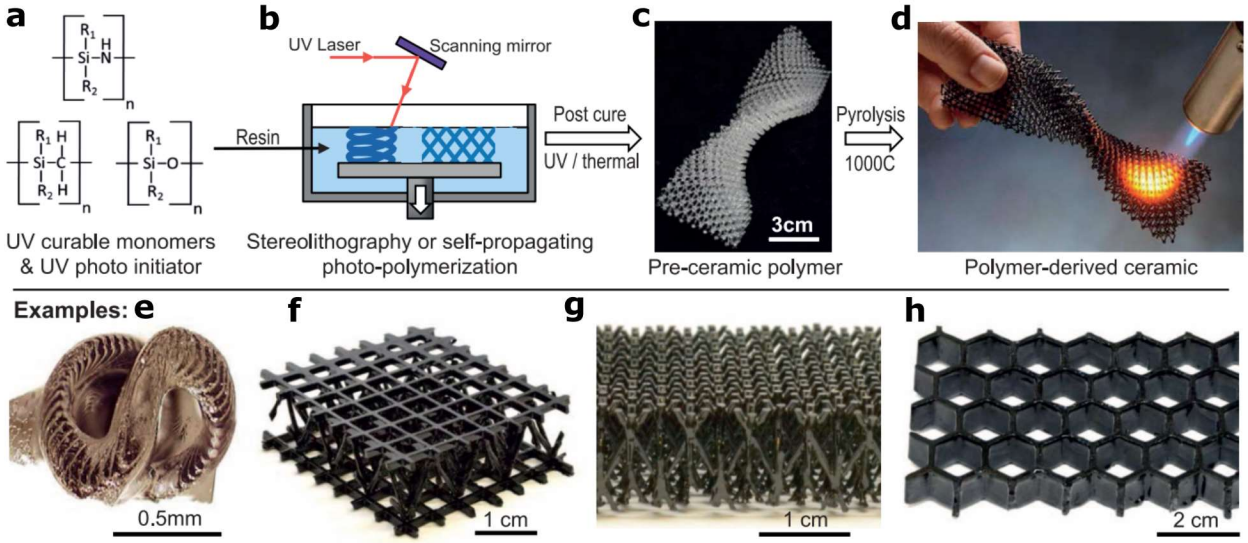

Figure 2.9: *Additive manufacturing of polymer-derived ceramics. (a) UV-curable organosilicon preceramic monomers are mixed with photo initiator. (b) The resin is exposed with UV light in a SLA 3D printer or through a patterned mask. (c) A preceramic polymer part is obtained. (d) Pyrolysis converts the polymer into a ceramic. Examples: (e) SLA 3D printed corkscrew. (f, g) self-propagating photopolymer waveguide technology (SPPW) formed microlattices. (h) Honeycomb structure. Reproduced with permission from Ref.[87], Copyright 2016 American Association for the Advancement of Science.*

2.6 Energy storage

Batteries are the most common form of energy storage devices to date. The origin of battery can be traced back to the Parthian empire (247 B.C.-224 A.D.), when the "Baghdad Battery" was discovered in 1936 during an archeological excavation near Baghdad[92]. Alessandro Volta initiated the modern battery history by developing "Volta Cell", which contained alternating copper and zinc plates separated by cardboards[93]. With the invention of lead-acid battery, the world has seen the emerge of rechargeable energy storage technologies in 1859[93]. The next major breakthrough in the field of battery was the introduction of Li-ion batteries (LIBs), which was proposed by Whittingham in 1972, transformed into a successful development by Goodenough in 1980s, and commercialized by Sony in 1990s[94].

Despite significant evolution from the Volta cell to LIBs as well as supercapacitor devices, each of these technologies still falls behind the demands of industry. EESS technologies and progress of material science dictates that there is a need of essential elements to overcome the challenge of supplying a stable energy. In the last decade, continuous progress has been made towards this goal through the development of advanced electrode active materials. Thus, high-energy rechargeable batteries (e.g., LIBs) and high-power supercapacitors are being researched. However, to replace commercial needs of fossil fuel for stable and continuous energy supply, each of these stand-alone technologies has to show significant advancement toward energy storage. As shown in Figure 2.10, the LIB industy is expected to grow over 30% per year until 2030. However, this strong demand will also increase the need of LIB raw materials. combining the high power characteristics of supercapacitors with the high energy content of rechargeable batteries may improve the performance of hybrid energy storage devices towards the diagonal target.

2.6.1 Lithium-ion battery (LIB)

LIB consists of a positive electrode (cathode) and a negative electrode (anode) separated by an electronic insulating separator (barrier), an electrolyte, as well as current collectors and a casing as shown in Figure 2.11. The separator prevents instant self-discharge and

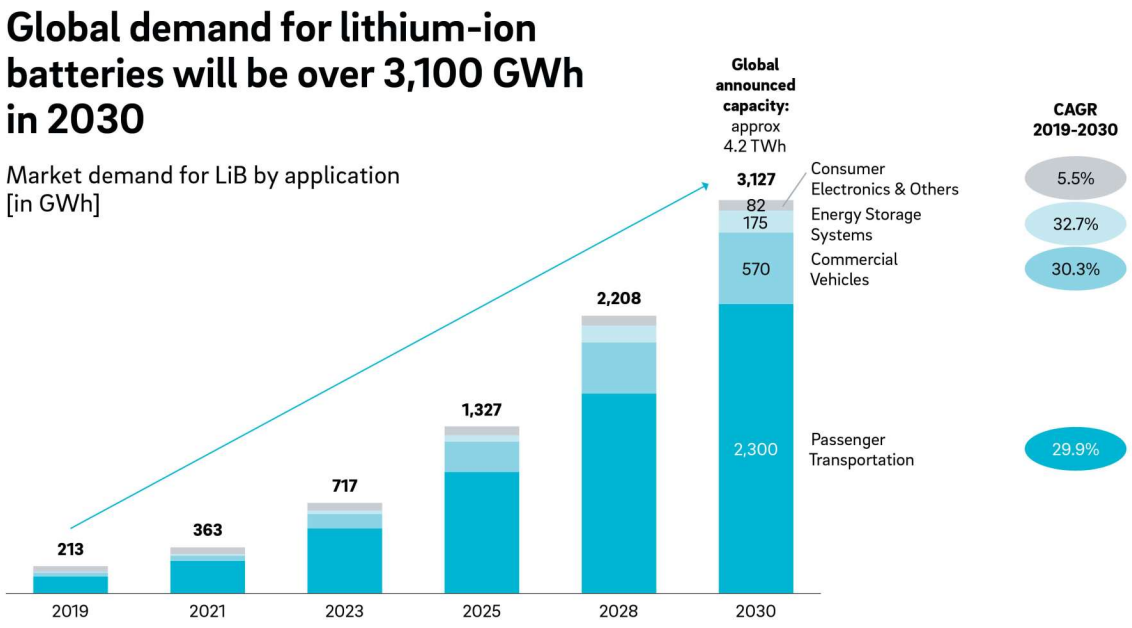

Figure 2.10: *Global market demand for LIB by application in GWh. Reproduced with permission from*[95]*. Copyright 2022 Roland Berger.*

electrical short circuits between the two electrodes, while allows the Li^+ ions shuttling back and forth between the anode and cathode through a chemically stable liquid but restricts the movements of electrons. The chemically stable liquid that works as a host of the Li^+ ions is known as electrolyte, which consists of lithium salts dissolved in an organic solvent[96].

When LIB shown in Figure 2.11 is charged, Li^+ ions are stored in the anode (graphite + SiO_x in this case). Li^+ ions will move from anode to cathode if the circuit is kept closed without applying any external voltage, which is known as cell discharging and cell voltage will decrease to zero gradually. At the same time, anode will lose electron, while cathode gains electron. As a result, the oxidation number of anode will increase. Due to the high resistance of the electrolyte and separator, these electrons are forced to flow through an external circuit; therefore, powering the load (e.g., remote control, lamp, etc.). It is worth noting that during the discharge process in a LIB, Li^+ ions move towards the cathode (lithium transition metal oxide depicted by Figure 2.11) in order to keep the charge neutrality. During charging of cell, Li^+ ions move back to the anode from cathode, which is achieve by an applied voltage. Potential versus capacity chart of the cathode and anode materials considered for LIBs is

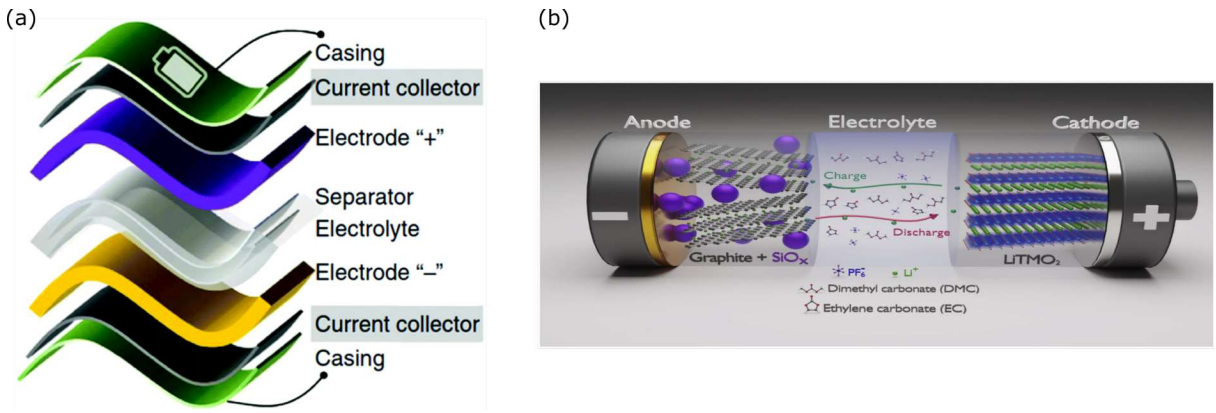

Figure 2.11: *(a) Components of typical energy storage cell. Reproduced with permission from*[97]*. Copyright 2016 Springer Nature. (b) Schematic illustration of the state-of-the-art lithium-ion battery chemistry with a composite of graphite and SiOx as active material for the negative electrode (note that SiOx is not present in all commercial cells), a (layered) lithium transition metal oxide (LiTMO2; TM = Ni, Mn, Co, and potentially other metals) as active material for the positive electrode, and a liquid electrolyte based on organic carbonates as solvents and LiPF6 as conducting salt; the electrolyte commonly comprises moreover a set of additives and potentially also additional solvents and lithium salts. Reproduced with permission from*[98]*. Copyright 2020 Elsevier B.V.*

presented in Figure 2.12.

As the discharge is a spontaneous process, the open cell voltage can be determined by equation 2.1.

$$voltage = -\frac{\mu^c - \mu^a}{z.F} = -\frac{\Delta G_r}{z.F} \tag{2.1}$$

Where in equation 2.1, $_c$ and $_a$ are the chemical potentials of cathode and anode electrodes, respectively, z is the valence of working ion (+1 for Li^+), F corresponds to Faraday constant (96,485 C mol^{-1}), and G_r is the Gibbs free energy of reaction.

2.6.2 Supercapacitor

Supercapacitor is another class of electrochemical energy storage systems (EESS). The origin of capacitor is attributed to the invention of "Leyden Jar" in 1745[100]. The first electrolyte capacitor was patented in 1896, where a high-purity etched aluminum foil was attached with aluminum dioxide as a dielectric. The concept of electrochemical double-layer capacitor (EDLC) was patented by General Electric in 1957, which had porous carbon material coated

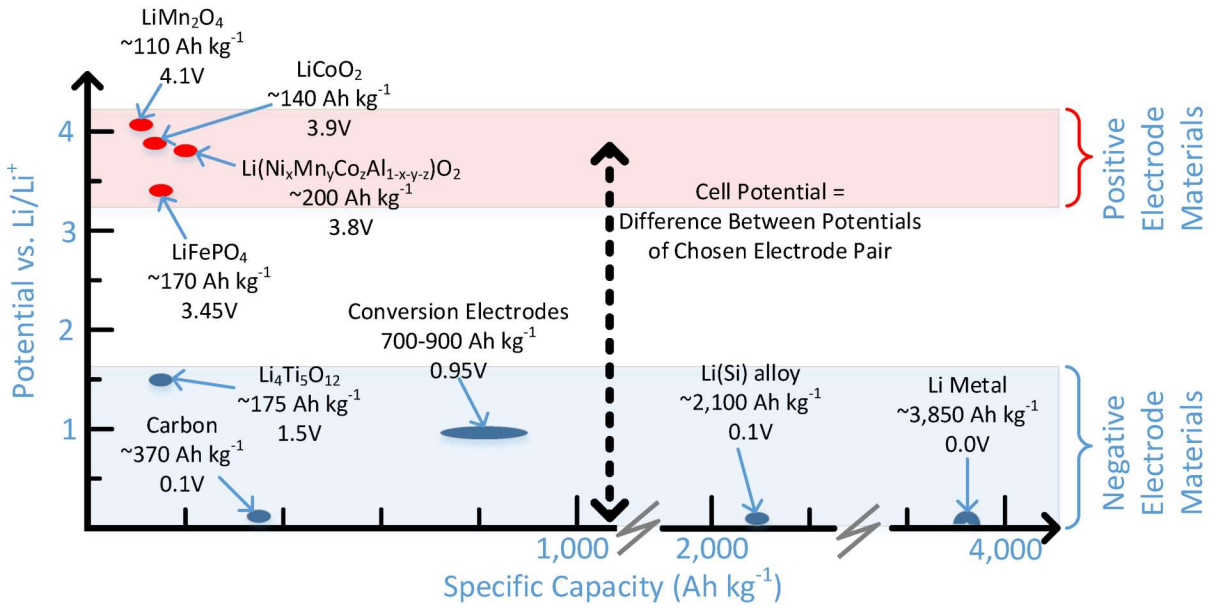

Figure 2.12: *A summary of some present and future electrode chemistry options for Li-ion batteries. The proposed capacity of the Li(Si) is 50% of the theoretical capacity of the material, similar to the case found for some of the positive electrode materials. Reproduced with permission from*[99]*. Copyright 2019 MDPI*

on metallic current collector'[101]. However, Nippon Electric Corporation (NEC) commercially introduced EDLC in 1971. It was NEC, who introduced the term "supercapacitor" for EDLC, where they developed a low-power device for memory bcakup applications[102]. The pseudo-capacitor concept was reported by Trasatti and Buzzanca for the first time in 1971, that opened up a new possibility for improved capacitance in supercapacitors[103].

Supercapacitors (also known as electrochemical capacitors or ultracapacitors) are different from conventional capacitor. Conventional capacitors are electrostatic capacitors, which use thin insulating dielectrics between two parallel plates as shown in 2.13(a). Supercapacitors consist of two electrodes separated by an ion-permeable separator (such as glass, ceramic, plastic, cardboard or paper) and an electrolyte that ionically connects the two electrodes. In a supercapacitor, the charge is stored either at the electrode/electrolyte interface by separation of charge in a Helmholtz double layer (known as electrochemical double layer capacitance or EDLC) or by charge-transfer via Faradaic redox reactions (known as pseudo-capacitance)[104]. Supercapacitors are considered to be high-power (W) systems, whereas the

batteries are considered to have high-energy (Wh) systems.

The energy storage mechanism in EDLCs is based on the electrolyte ion adsorption/ desorption on the interface of the electrode active materials and electrolyte as shown in Figure 2.13(b). Using an electronically conducting electrode material with highly accessible surface area is essential in achieving high capacitance in EDLCs. Nanostructured carbon-based materials have good electrical conductivity and posses high specific surface area, which make these materials promising choice for EDLCs[105]. In EDLCs, no Fardaic reaction happens in the electrode/electrolyte interface and no electrochemical reaction takes place in the bulk of the materials. In case of pseudocapacitors as shown in Figure 2.13, Faradaic redox reaction takes place at or near the surface of the electrode materials. There is another type of hybrid energy storage systems such as lithium-ion capacitor (LIC), where both EDLC and Faradaic reactions are used to store the charges (Figure 2.13(d)).

The non-electrode components such as the current collectors, separators and binders aid in sufficient electronic wiring within the electrode. However, the critical discussion of this thesis is focused on a selected set of electrode active materials (i.e. PDCs).

2.7 PDCs in energy storage[1]

EESS are critical for sustainable and environmentally-friendly alternative energy sources. In the last few decades, many scientific research studies have focused on developing high capacity rechargeable devices with long life cycles. The challenge for researchers has been to develop small, light-weight systems that have high energy and power densities during their long cycling time to accommodate real-life applications. In this regard, polymer-derive ceramics (PDCs) have emerged as the electrode materials of choice for secondary batteries to replace traditional graphite-based electrodes.

The unique polymer-to-ceramic route of PDCs has shown promise for electrochemical energy storage applications due to their high chemical stability in corrosive environments,

[1]Reprinted from Mujib, S. B., and Singh, G. (2022). Polymer derived SiOC and SiCN ceramics for electrochemical energy storage: A perspective.*International Journal of Ceramic Engineering Science*, 4(1), 4-9.

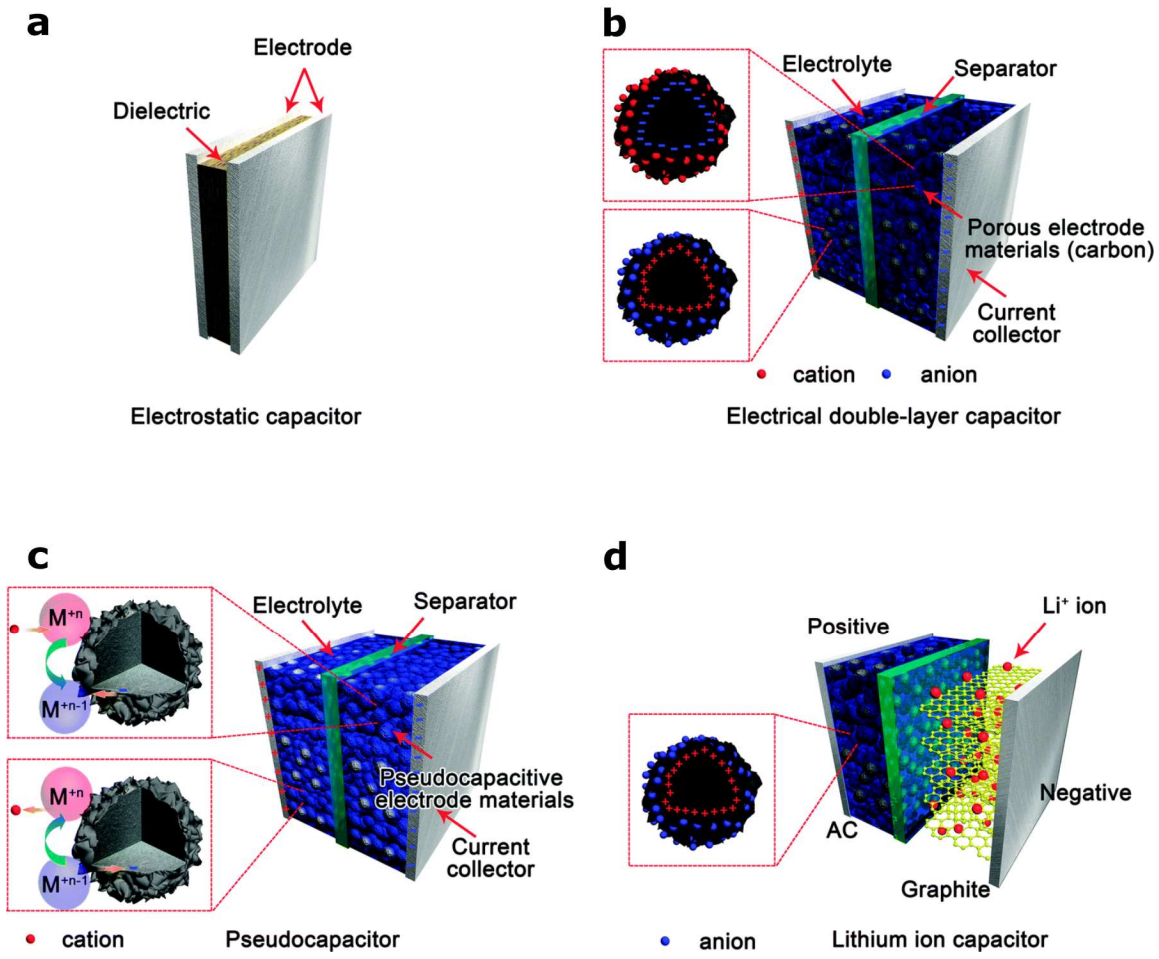

Figure 2.13: *Schematic diagram of (a) an electrostatic capacitor, (b) an electric double-layer capacitor, (c) a pseudocapacitor, and (d) a hybrid-capacitor. Reproduced with permission from*[106]*. Copyright 2015 The Royal Society of Chemistry.*

thermodynamic stability in high-temperature environments, high creep resistance, and tunable molecular structure, meaning the final ceramic has controllable porosity and electronic conductivity[107]. In addition, PDCs can be easily fabricated to many desirable shapes and structures (e.g., fibers, coatings, ceramic matrix composites, MEMS etc.) as demanded by the application[5–8;10]. Also, variable processing parameters, such as pyrolysis temperature and environment, provide significant property variation in the PDCs, which has made PDCs promising electrode materials for rechargeable metal-ion batteries and supercapacitors.

The electrochemical properties of ceramics derived from a molecular precursor were first introduced by Dahn et al. in the 1990s[11;12]. For the following two decades, researchers have

diligently studied PDCs' ability to reversibly intercalate metal-ions. The mixed bond structure in the final amorphous ceramic and the conducting carbon phase, especially in silicon-based PDCs, control the electrochemical properties of PDCs in reversible storge systems[13–15]. PDC performance as electrodes in electrochemical energy storage devices has also been investigated systematically using various fabrication techniques. In addition to conventional bulk powder-based film, thinner films fabricated by depositing preceramic polymer onto a current collector, followed by pyrolysis, have shown promise to achieve high storage capacity of PDC electrodes[16]. The used of additive manufacturing technology to fabricate complex and lightweight PDC electrodes has also been reported[108], and electrospinning technique has been utilized to fabricate flexible, wearable, cloth-like PDC electrodes to achieve outstanding electrochemical performance[19]. All these techniques enable the hierarchical porosity and intrinsic conductivity in the PDCs, which can successfully buffer volume changes of the electrode during charge/discharge cycles. The following sections describe the electrochemical performances of various PDCs synthesized using different techniques in metal-ion batteries.

2.8 PDCs in lithium-ion batteries

LIBs extensively utilize Si-based nanostructures due to their favorable properties towards lithium storage, (e.g., high theoretical capacity of 4200 mAh g^{-1}, which is almost ten-fold higher than traditional graphite electrodes[20;21]) and because Si has low charge/discharge potential (0.5 V vs. Li/Li^{+})[22]. However, the formation of Li-Si alloy is less reversible in room temperature, and Li insertion into Si results in 400% volume expansion of the Si lattice[23;24], which contributes to electrode pulverization, reduced electrical contact, and severe capacity fading. One of the ways to overcome this problem is to utilize Si-based PDCs instead of Si in its bulk form. Current state-of-the-art applications of Si-based PDCs can store lithium reversibly in the potential range of 0-3 V and provide a specific capacity of 900 mAh g^{-1} with a high coulombic efficiency of 99%. In addition, the porous microstructure of PDCs provides high surface area, and structural stability during lithiation and delithiation. Among several alternatives, silicon oxycarbide, derived from polysiloxanes, and silicon carbonitride,

derived from polysilazane, are the most promising PDCs as electrode materials. The most common synthetic process of SiOC and SiCN, and their charge-storage mechanism is shown in Figure 2.14(a-b).

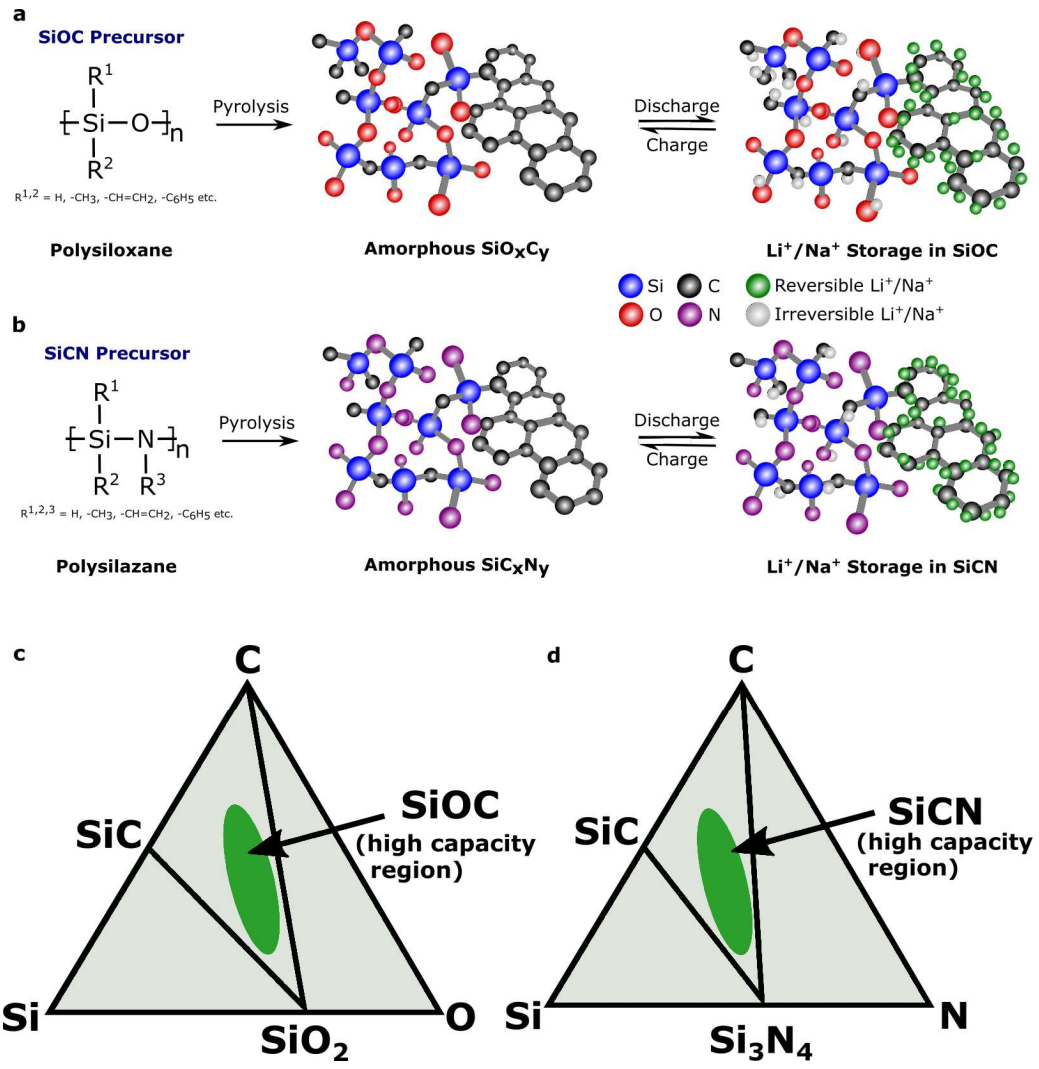

Figure 2.14: *The most common precursors used for synthesis of polymer-derived (a) SiOC and (b) SiCN and their microstructures. Schematic representation of SiOC and SiCN as active electrode materials in EESS. The green Li^+/Na+ ions stored reversibly in the systems, whereas gray Li^+/Na+ ions are captured irreversibly. The phase diagram of (c) SiOC and (d) SiCN ternary systems. The high capacity occurs towards the green shaded area in the center of the pyramids.*

2.8.1 SiOC system

Silicon oxycarbide (SiOC) is a ternary Si-based ceramic system, that is composed of a mixed network of Si tetrahedrally bonded to carbon and oxygen atoms and a segregated carbon phase (free C) to form an amorphous ceramic structure. The presence of mixed bonds and free C in the structure prevents crystallization of the silica phase and controls oxidation resistance[25]. Maximum capacity is achieved in the amorphous ceramic phase as shown in Figure 2.14(c), where the SiO_2 and SiC mixed bonds co-exist with the free C domains.

Since Wilson et al. reported bulk SiOC as potential anode material in LIBs in 1994[11], continuous efforts have been made to apply SiOC anodes for Li^+ ion storage. Wilson et al. showed that amorphous SiOC derived from two different polysiloxanes achieved a specific capacity near 600 mAh g^{-1} when the majority of capacity were below 1.0 V vs Li/Li^+. In 1997, Xing et al. studied over 60 siloxane polymers to derive various compositions of SiOC samples at a temperature of 1000 °C[12]. They showed that the presence of carbon in amorphous SiOC is necessary to provide a path for Li^+ ions and electrons and to reversibly react with lithium. Xue et al. showed that irreversible capacity, associated with the first-cycle charge/discharge of a SiOC electrode in LIBs, increased with the increase of silicon and oxygen contents[26].

Dibandjo et al. studied the lithium insertion/extraction properties of dense and porous SiOC ceramics[27]. Porous SiOC was achieved by etching dense SiOC using a 20 vol% hydrofluoric acid (HF) solution. The initial cycles were run at a current density of 18 mA g^{-1}, and then the current density was increased to 36 mA g^{-1}. Although both dense and porous SiOC provided >600 mAh g^{-1} as first cycle capacities, the porous sample showed a stable electrochemical response up to 30 cycles while the dense sample capacity dropped to zero after 10 cycles. Kaspar et al. studied the influence of pyrolysis temperature ranging from 900 to 2000 °C[28;29]. Results showed that increasing temperatures caused the free C phase to organize toward ordered configurations, and amorphous SiOC resulted in SiC crystals. In addition, decomposition of the SiOC network at increased temperature decreased the stability of the free C phase. As a result, the reversible capacity dropped from 660 mAh g^{-1} at

900 °C to 80 mAh g^{-1} at 2000 °C.

Ahn et al. utilized the coulometric titration technique to study hysteresis in SiOC ceramics[30]. They measured the polarization potential of hysteresis to be 250-500 mV, which occurred at the anode-electrolyte interface and was proportional to the cycling rate. Coating the active SiOC with a few layers of alumina shifted the hysteresis curve by 50 mV, indicating that hysteresis was due to the kinetics and thermodynamic limitations of Li^+ ions diffusion in the SiOC system. Kaspar et al. showed that the presence of carbon influences electrical conductivity and thus capacity of the SiOC electrode in LIBs[31]. Materials with carbon content ¡20 wt.% showed electrical conductivity of 3*10-8 S m^{-1}, and their initial capacity faded rapidly with cycling. However, materials with higher C contents had up to 2.2 S m^{-1} electrical conductivity and demonstrated stable specific capacity of 500 mAh g^{-1} after 60 cycles.

Sun et al. incorporated the first-principles theoretical approach to study lithium storage in SiOC[32]. They suggested a two-step process: Li^+ ions are first absorbed in the nanovoids, and then they get absorbed in SiOC tetrahedral units, free C phase, and defects. Figure 2.15(a) shows the supercell model of carbon-rich SiOC with boundary condition. The unit cell containing the Si, O, and C atoms with the nanovoids are shown in Figure 2.15(b). The formation of energy and volumetric strain of SiOC as a function of Li concentration during two-step lithiation are shown in Figures 2.15(c) and (d). In the segregated C phase charge transfer occurred in the defects and edge of five or seven carbon rings, whereas in the SiOC system charge transfer occurred primarily around the oxygen and carbon atoms. The red line indicates lithiation in nanovoids, whereas the blue line shows lithiation in SiOC units and carbon phase.

2.8.2 SiCN system

The silicon carbonitride (SiCN) is another ternary Si-based ceramic system, that includes Si, bonded to carbon and nitrogen atoms and a segregated carbon phase. Similar to SiOC, the high capacity of the SiCN is achieved towards the center of the amorphous ceramic phase as

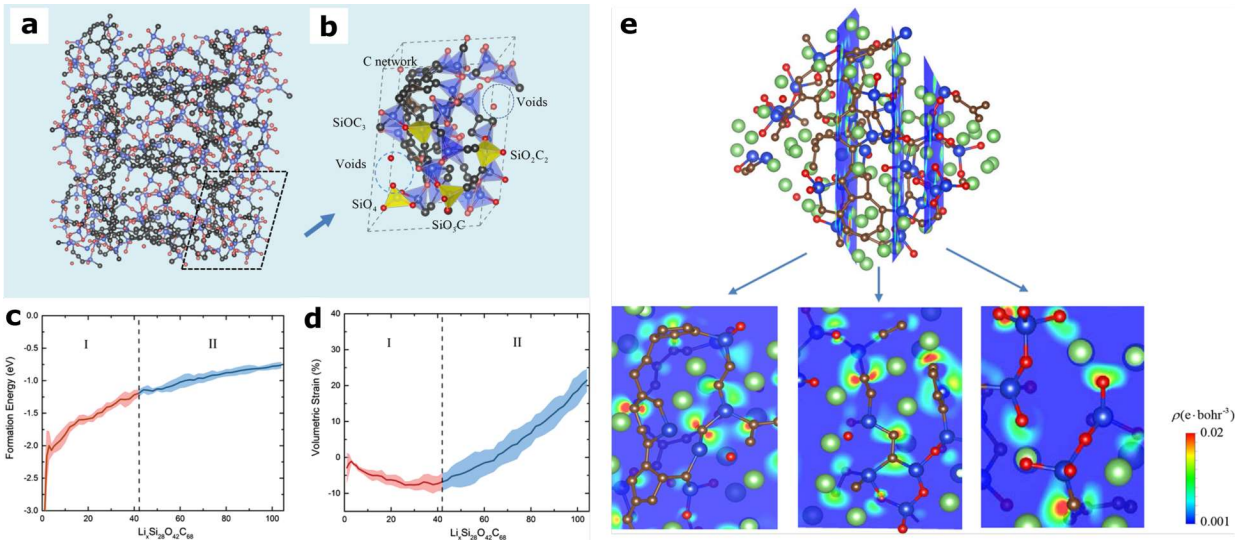

Figure 2.15: *Lithium storage mechanism in SiOC system. (a) Supercell atomic model of SiOC, containing SiO_xC_{4-x}, segregated C phase, and nanovoids. (b) Unit cell of SiOC shows a series of SiO_4, SiO_3C, SiO_2C_2, and $SiOC_3$ tetrahedral units. The gray atoms indicate the segregated C phase which forms the backbone of the network. (c) Formation energy of SiOC during lithiation in Li_xSiOC, and (d) volumetric strain as a function of Li concentration during two-step lithiation. (e) Charge-density map in different regions of $Li_{66}Si_{28}O_{42}C_{68}$. Most of the charge transfer takes place in the O atoms and unsaturated C atoms. Reproduced with permission from*[32]*. Copyright 2017 American Chemical Society.*

shown in Figure 2.14(d). Liebau-Kunzmann et al. were among the first to suggest the use of SiCN as potential anode for LIBs[33]. They synthesized lithium-containing SiCN via lithiation of polysilazane. Li bonded to C and N in the SiCN system were found after pyrolysis at 1100 °C. Their results affirmed the potential use of a SiCN anode in LIBs.

Su et al. investigated the electrochemical properties of SiCN in LIBs, where SiCN were obtained at various pyrolysis temperature[34]. Results showed that amorphous SiCN obtained at 1000-1300 °C had a free C phase and showed a high first cycle capacity of 608-754 mAh g^{-1}. However, the SiCN derived at 600-800 °C contained organic groups, and the SiCN derived at 1400-1500 °C contained SiC crystallites, which exhibited much lower specific capacities than the amorphous SiCN. Graczyk-Zajac et al. studied the performance of SiCN in LIBs derived from polysilazane at five temperatures: 1100, 1300, 1500, 1700, and 2000 °C[35]. Pyrolysis of the SiCN samples at different temperatures produced two types of carbon in the structure: non-graphitic disordered carbon and turbostratic carbon. Increasing the temper-

ature over 1500 °C contributed to the formation of the -SiC phase, which decreased capacity at higher temperature (>1500 °C). The authors showed that carbon-rich SiCN prepared at 1300 °C exhibited the highest capacity of 300 mAh g^{-1}. Liu et al. studied the variation of pyrolysis environment using Ar and H_2 environments[36]. The H_2 atmosphere demonstrated higher carbon content and reversible capacity. DVB was used with polysilazane as an additional carbon source, the carbon content increased from 9.9 wt.% to 49.3 wt.%, resulting in increased specific capacity from 136 mAh g^{-1} to 574 mAh g^{-1} for SiCN as an anode in LIBs.

Feng et al. investigated five different polymer precursors to synthesize SiCN with various carbon contents[92]. They also studied the carbon contribution in SiCN materials during lithiation/delithiation and the reason for capacity fading. Results showed that the di-n-octyldichlorosilane synthesized poly-silyl-carbodiimide sample provided the highest carbon content, with the highest reversible capacity of 826.7 mAh g^{-1} after 100 cycles with >97% coulombic efficiency. The outstanding electrochemical performance of this SiCN anode was due to the formation of a stable solid electrolyte interface (SEI) layer on the anode surface, which prevented electrode cracking during lithiation/delithiation. Increased carbon content also resulted in high electrical conductivity and electrochemically reactive sites.

2.8.3 PDC/nanomaterial composites

PDC-based anodes such as SiOC and SiCN pose several drawbacks when used on their own as powder-based, thin film, amorphous, or crystalline electrodes in LIBs. High first-cycle loss, voltage hysteresis, and capacity decay are the primary disadvantages of using bare PDC materials as electrodes. Therefore, researchers have introduced nanomaterials, especially graphene or carbon nanotubes (CNTs), into PDCs to synthesize nanomaterial-based composite electrode materials. These PDC-nanomaterials composites offer reduced ionic diffusion length, high electronic mobility, and high aspect ratio[107]. For example, Konno et al. synthesized a SiOC/exfoliated graphite composite and studied the electrochemical performance in LIBs[93]. As an anode, this composite material delivered a reversible capacity of 625

mAh g^{-1} with a first cycle loss of 30%. The composite samples were pyrolyzed at 1000-1300 °C and all the samples showed stable performance at a high current density of 100 mA g^{-1}. Wu et al. embedded SiOC nanolayers directly into graphite to synthesize a SiOC/graphite composite electrode[94]. The graphite acted as a support to enhance the structural stability and electrical conductivity of the composite and decreased the diffusion path for lithium. The synthesis process of the composite electrode is shown in FigureFigure 2.16(a). TEM image in FigureFigure 2.16(b) shows the SiOC nanolayers randomly distributed on the surface of 200-300 nm size graphite substrates. As a result, the composite anode showed almost 100% capacity retention as shown in Figure 2.16(c), even after cycling at 5000 mA g^{-1}, while the electrode showed a diffusion coefficient of 2*10-10 cm^2 s_{-1} and delivered a reversible capacity of 500 mAh g^{-1} over 1000 cycles at a current density of 2000 mA g^{-1} (Figure 2.16(d)).

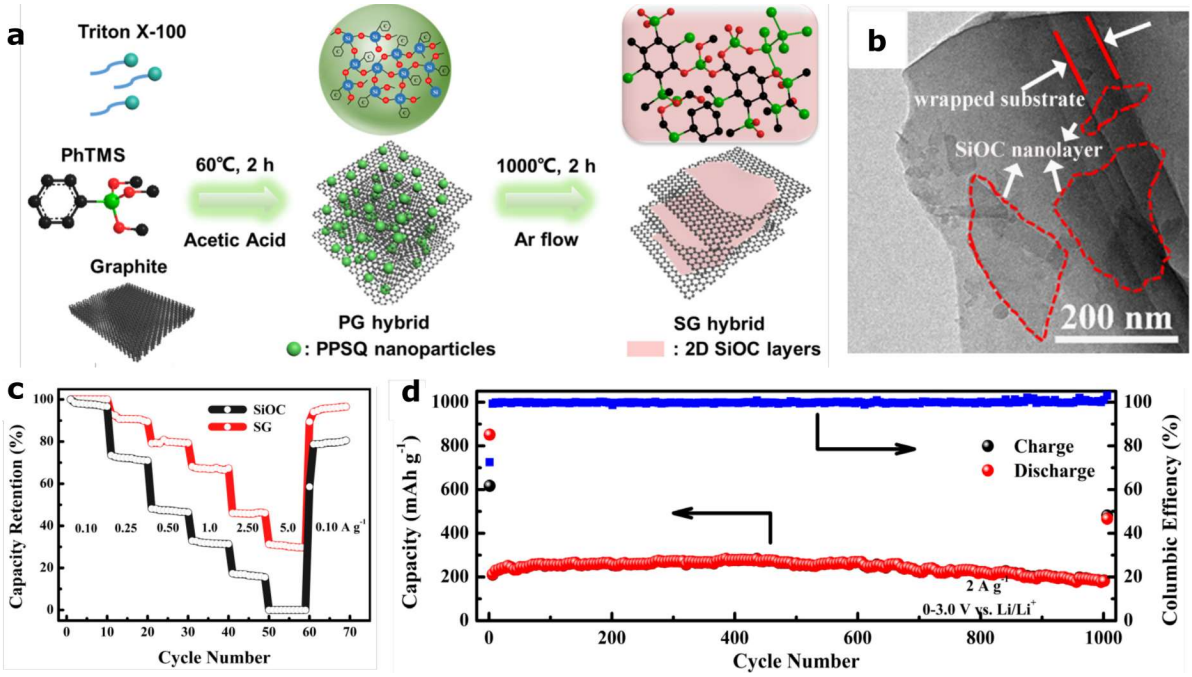

Figure 2.16: *Electrochemical performance of SiOC/graphite composite anode in LIBs. (a) Schematic shows the synthesis process of SiOC nanolayers directly-embedded in graphite. (b) HRTEM image of SiOC/graphite nanocomposite showing the SiOC nanolayers on graphite substrate. (c) Rate capability of SiOC and SiOC/graphite anodes in LIBs. (e) Cycling stability performance of SiOC/graphite anode shows excellent cycleability of the electrode even at a higher current density of 2 A g^{-1}. Reproduced with permission from[94]. Copyright 2019 Elsevier B.V.*

Feng et al. introduced CNTs into SiCN by pyrolyzing polysilylethylenediamine with

multi-walled CNTs at 1000 °C[96]. The as-synthesized SiCN/CNT composite, which was used as anode material in LIBs, delivered a high discharge capacity of 1176.6 mAh g^{-1} at a current density of 0.2 mA cm^{-2}. The 3D network of CNTs provided an enhanced electrical conductivity and a stable structure to the composite electrode. The electrochemical performance of the SiCN/CNT composite was much higher than the capacity of pure SiCN, CNTs, and commercial graphite electrodes.

David et al. coated an aluminum-modified polysilazane on the surface of CNTs to synthesize a Si(Al)CN/CNTs composite electrode material[97]. The as-prepared composite electrode showed high rate capability and cycling stability as LIB anode, due to the enhanced electrical conductivity (by 7 times compared to SiCN), when SiCN interfaced with aluminum and CNTs. The Si(Al)CN/CNT electrode exhibited stable specific capacity of 577 mAh g^{-1} at a current density of 100 mAh g^{-1} and 400 mAh g^{-1} at an extreme current density of 10,000 mA g^{-1}. Huang et al. integrated MnO nanoparticles into a SiOC matrix to investigate the electrochemical performance of SiOC/MnO electrodes[98]. MnO has high theoretical capacity (755 mAh g^{-1}), low volage hysteresis (<0.8 V), and low plateau voltage (1.032 V) in LIBs. Introducing MnO into the SiOC ceramic resulted in stable performance with high capacity. The SiOC/MnO composite anode in LIBs delivered a high reversible capacity of 770 mAh g^{-1} at a current density of 100 mA g^{-1} after 200 cycles. In another study, Idrees et al. introduced nitrogen sulfur dual-doped graphene sheets (NSGs) into the Si(B)CN[109]. NSGs were introduced into pyrolyzed Si(B)CN using the ball milling technique. When tested as an anode in LIBs, the as-prepared Si(B)CN/NSG composite exhibited a high specific capacity of 785 mAh g^{-1} after 800 cycles at a current density of 450 mA g^{-1}. The intrinsic defects of NSGs provided enhanced active sites to the composite electrode and improved the electrochemical performance.

In summary, PDCs are unique compounds with tunable compositions and variable properties. Negligible capacity fading for C-rich PDCs at higher current in LIBs, and ability to accommodate Li^+ ions in the amorphous PDC structure, are some of the major advantages of using PDCs in EESS. However, there are some drawbacks in using PDC anodes such as high processing temperature, high voltage hysteresis and high first-cycle capacity loss

etc. A greater understanding and control of the phase distribution/composition during the synthesis of PDCs will help to effectively utilize them in energy storage devices.

Chapter 3

Fabrication of PDC/Carbon fiber ceramic mini-composites

3.1 Preview

In this study, the potential of polymer-derived ceramic matrix composites (CMCs) is demonstrated by addition of thin ceramic coatings on carbon fiber (CF) bundles. Boron- and hafnium- modified polysilazane liquid precursors were used to wet the surface of fibers to synthesize Si(B)CN/CF and Si(Hf)CN/CF CMC mini-composites, respectively. Nearly completely dense and defect free ceramic matrix were obtained.

3.2 Introduction

Ceramic matrix composites (CMCs) are suitable candidates for aerospace and aircraft components (hypersonics, turbine engines, atmospheric re-entry vehicles, and rocket nozzles) due to their low density, high limit of damage tolerance and improved reliability[110–112]. Hypersonic flights introduce high heat fluxes, whereas turbine engine blades and rocket nozzles require new materials to increase operational temperatures while maintaining a lightweight structure[113–115]. Temperatures in specific regions of these flights can surpass 1500 °C, which

cannot be sustained by current metal alloys without active cooling[1]. CMCs are capable of satisfying the high-temperature requirements in a lightweight structural form for aerospace applications[116;117].

Ceramic monoliths and conventional ceramics such as SiC or Si_3N_4, manufactured via powder processing technology, have shown exceptional oxidation resistance above 1000 °C in a low density form[118]. However, the brittle nature of these ceramics prevents machining. On the other hand, Si-based polymeric precursors, commonly known as poly(organosilazanes), poly(carbosilane) and poly(organosiloxane) transform into complex ceramic materials such as SiCN, SiC, and SiOC upon controlled thermal decomposition[119–121]. These covalently bonded molecular precursor-derived ceramics (PDCs) differ from traditional ceramics because PDCs have processing flexibility that allows to achieve desired shape, control of nano-structure of the final ceramic product by tuning the precursor chemistry, low processing temperature, and the ease of composites fabrication[122]. In addition, elemental doping and the addition of fillers, including B[123], Al[124], ZrO_2[125], TiO_2[126], and HfO_2[127], is possible for PDCs. Depending on the elemental configurations Si-based PDCs can be used in various high-temperature applications involving coatings, sensors, reinforcement, or matrices[128].

Previous works have primarily studied liquid-precursors synthesized from multiple sources to fabricate quaternary ceramics[129–132], and reported various elaborate techniques to fabricate ceramic composites such as PIP[131;133], mechanical alloying and hot-press sintering[134], spark plasma sintering[135] etc. The current work aimed to study the efficacy of the infiltration process of carbon fibers (CFs) cloth or mini-bundles of CFs by single-source liquid-phase precursors of Si(B)CN and Si(Hf)CN, and the effect on the morphology and micro-structure of the mini-composites. Here, a polysilazane-based precursor was mixed with boron-, and hafnium-containing precursors to synthesize Si(B)CN and Si(Hf)CN polymeric precursors, respectively. The homogenous solutions of the precursors were then allowed to infiltrate carbon fiber cloth via a drop-coating process mimicking a lab-scale polymer infiltration process, and then crosslinked and pyrolyzed to achieve Si(B)CN/CF and Si(Hf)CN/CF ceramic mini-composites. For comparison purposes, SiCN/CF mini-composites were also fabricated using the polysilazane precursor. Several characterization techniques, such as scanning elec-

tron microscopy (SEM), Raman and Fourier-transform infrared (FTIR) spectroscopy, X-ray photoelectron spectroscopy (XPS) were used to evaluate the polymer-to-ceramic evolution and micro-structures in SiCN/CF, Si(B)C/CF and Si(Hf)CN/CF ceramic composites.

3.3 Experimental

3.3.1 Materials

A commercially available carbon fiber cloth was used in this study as the reinforcement phase: 6K, 2x2 Twill Weave Carbon Fiber (Fibre Glast Developments Corporation, USA). According to the manufacturer, the fiber has a thickness of 0.017 inches and a weight of 10.9 oz/sq yd.

The polysilazane ceramic precursor, $Ceraset^{TM}$ PSZ 20 was obtained from Clariant Corporation, USA. Trimethyl borate (TMB) (98 %, MW 103.91 g mol^{-1}) and hafnium isopropoxide isopropanol (C12H28HfO4) (99.9 %, MW 414.84 g mol^{-1}) were purchased from Sigma Aldrich, USA. For the preparation of coating solutions, isopropanol (99.9 %, MW 60.096 g mol^{-1}) from Fisher Scientific, USA was also used as the solvent.

3.3.2 Preparation and optimization of preceramic polymer precursor for Si(B)CN and Si(Hf)CN ceramic

Si(B)CN-preceramic polymer: Boron-modified silazane was prepared following procedures described in a patent by authors[136]. Boron reagent TMB was added in a drop-wise manner to poly(ureamethylvinyl)silazane (commercial name: CerasetTM) in a large beaker at a slow rate of 1 mL min^{-1} while the Poly(ureamethylvinyl)silazane was stirred at 300 rpm overnight. The overall concentration of boron reagent to Ceraset was approximately 1:1 wt. %. The preceramic polymer's rheology sufficiently allowed wetting of the carbon fibers.

Si(Hf)CN-preceramic polymer: Hf-modified silazane was prepared following a similar procedure as described in the previous section. Because the rheology, polymer-to-ceramic

yield, and the optimum loading of Hf in polysilazane was not known, a study involving three different mass ratios of Hf reagent to polysilazane was conducted. As shown in the results in Figures 3.1 and 3.2, the 3:1 mass loading of Hf reagent in polysilazane lead to the pre-ceramic polymer reaching a saturation limit. Any further additions of Hf-reagent led to precipitation in the polysilazane (Figure 3.1(c)).

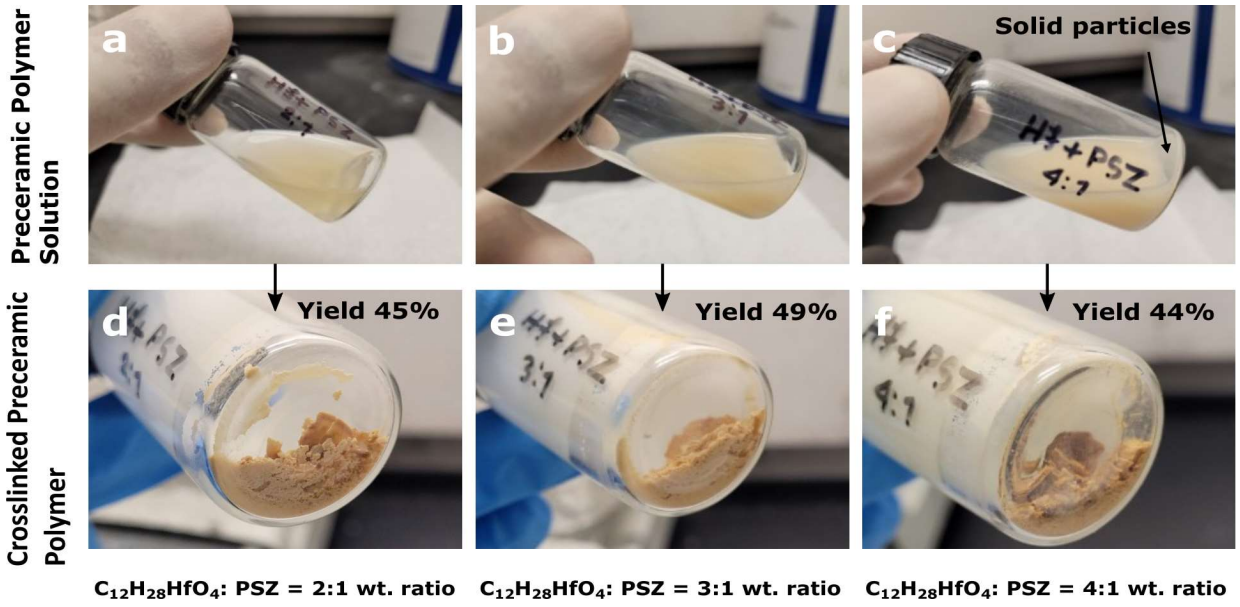

Figure 3.1: *Digital camera images: (a-c) Solubility of Hafnium Isopropoxide Isopropanol in Polysilazane (PSZ) with different concentrations (top) and (d-f) their corresponding crosslinked powders (bottom). Yield represents preceramic precursor solution to crosslinked polymer conversion*

3.3.3 Preparation of PDC/CF ceramic mini-composites

Circles with approximate diameters of 19 mm were cut from the CF cloth (approx. 100 mg) with a metal punch. The pre-ceramic polymer solutions (polysilazane, B-modified silazane for Si(B)CN ceramic , and Hf-modified silazane for Si(Hf)CN ceramic) were then injected using pipettes (approx. 30 mg) to infiltrate the CF circular discs entirely. Consequently, approximately 0.25 mL of preceramic polymer was used for approximately 25 mg of CFs. Then, the samples were cross-linked in air (300°C, 8 hours in an oven) or Ar (180°C, 16 hours in a glovebox). Next, the samples were pyrolyzed in an N_2 atmosphere at 800°C for 30 min,

Figure 3.2: *Digital camera image of the optimized Hf-modified polysilazane from (a) preceramic polymer precursor to (c) ceramic Si(Hf)CN powder. Yield represents the polymer-to-ceramic conversion (by mass).*

resulting in PDC/CF ceramic mini-composites (cited as CMCs) as shown in Figures 3.3(a) and (b).

The as-fabricated PDC/CF CMCs are shown in Figure 3.4. The preceramic polymer coated fibers were crosslinked in two different environment- in air at 300 °C and in Ar environment at 180 °C to achieve ideal ceramic coatings and yield on the carbon fibers. Crosslinking in Ar provided the best result in terms of ceramic yield from the polymeric precursor. As a result, further experiments were conducted only on samples fabricated in an inert environment. Polymer-to-ceramic conversion yield (by weight) of various CMC samples are presented in Table 3.1.

Table 3.1: *Conversion yield of coated samples by weight from polymer-to-ceramic stage.*

Pyrolyzed samples	Wt. Yield (%)
SiCN/CF (XL in air)	88
Si(B)CN/CF (XL in air)	72
Si(Hf)CN/CF (XL in air)	41
SiCN/CF (XL in Ar)	89
Si(B)CN/CF (XL in Ar)	94
Si(Hf)CN/CF (XL in Ar)	98

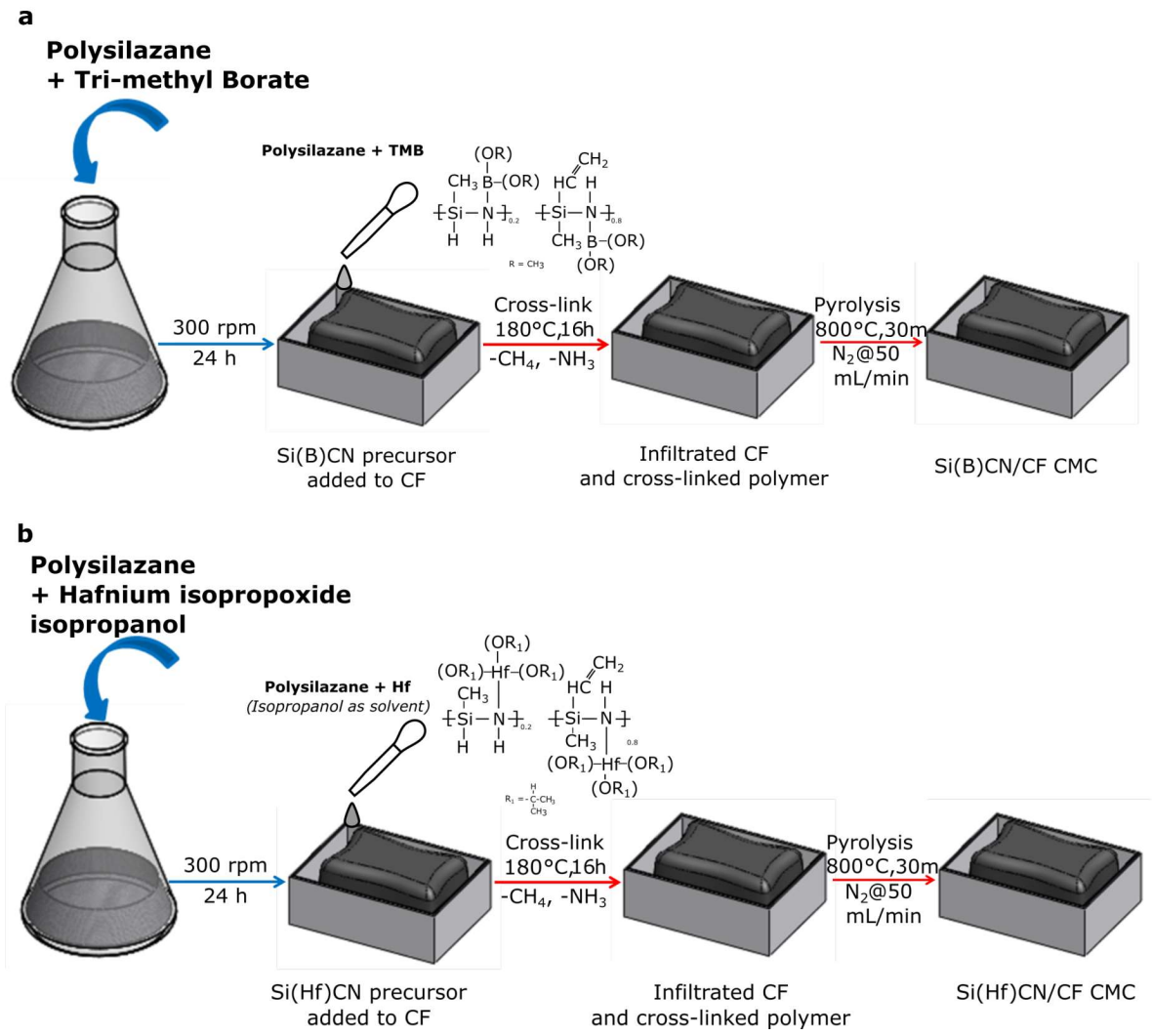

Figure 3.3: *Schematics show coating, crosslinking, and pyrolysis process of PDC/CF CMC mini-composites. (a) Synthesis process of Si(B)CN/CF, and (b) Si(Hf)CN/CF ceramic mini-composites.*

3.3.4 Characterization techniques

This study utilized several characterization techniques to determine the morphology, composition, and chemical compositions of the samples at various stages of fabrication of the CMC mini-composites. The surface morphology of the samples was studied using SEM on a Carl Zeiss EVO MA10 system with incident voltage of 5 kV.

The surface composition was analyzed by XPS using a Thermo Scientific Al Kα+ ion beam (beam energy = 1486.6 eV and spot size = 400 µm). An initial sputtering with Ar^+

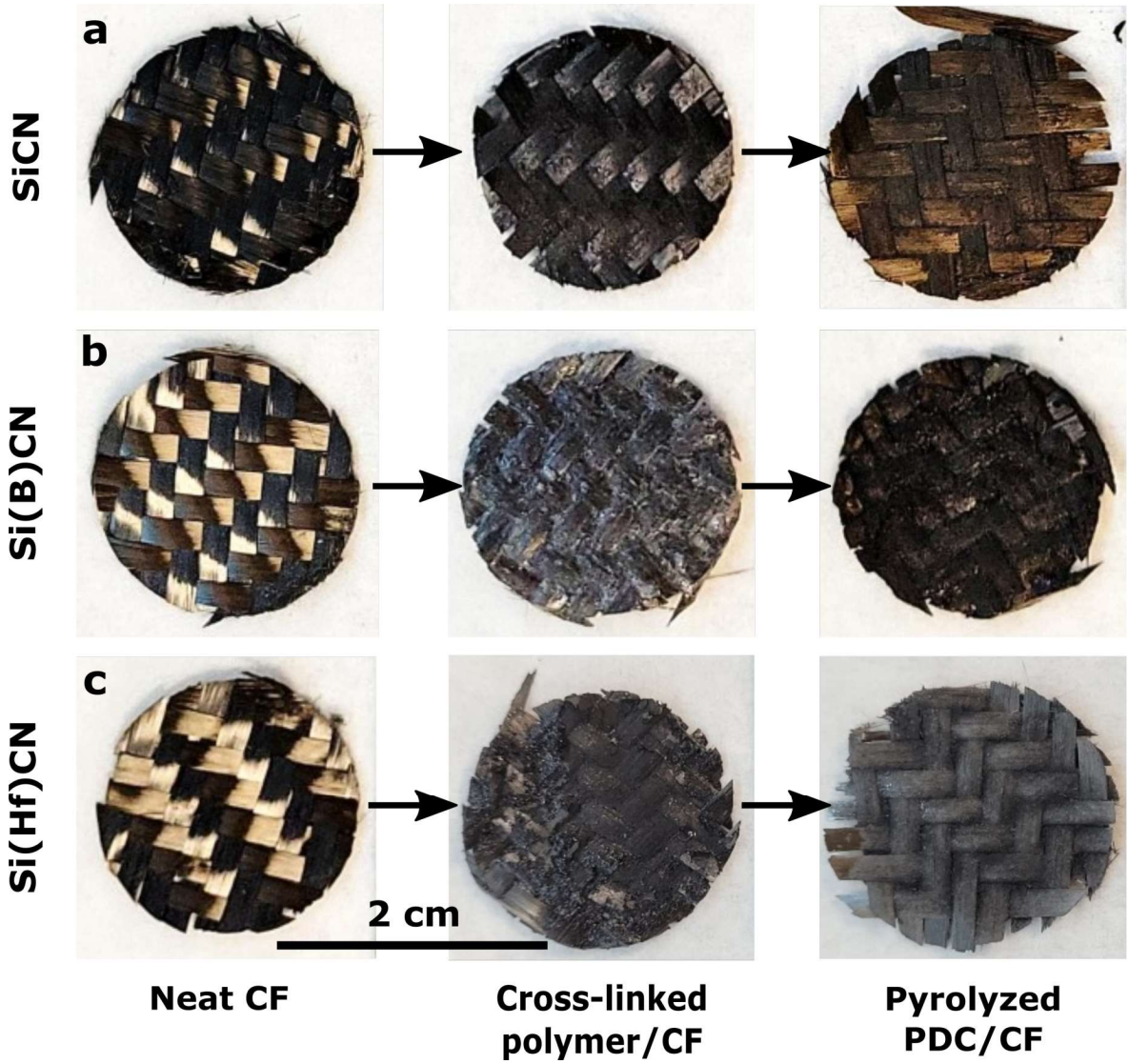

Figure 3.4: *Digital camera images of CFs coated with (a) polysilazane, (b) boron-modified polysilazane, and (c) hafnium-modified polysilazane before coating, after cross-linking and after pyrolysis. Crosslinking is done at 180 °C in Ar environment and pyrolysis is done at 800 °C in N_2 environment.*

at 3.0 keV for 2 min was performed on the surface of the ceramic coated fibers to remove the surface contamination.

Molecular structure and chemical evolutions of the CMCs were determined via Raman spectroscopy and FTIR. A confocal micro-Raman microscope (Horiba Jobin Yvon LabRam ARAMIS) equipped with a HeNe laser source (632.8 nm) was used to conduct Raman analysis in the range of 800 to 2000 cm^{-1} to determine the carbon vibrational modes. The

presence and evolution of various chemical functional groups of the silazane precursors in the composites were investigated using a Perkin Elmer Spectrum 400 FTIR spectrometer in the range of 500 to 2500 cm^{-1}.

3.4 Experimental

SEM micrographs of the CMC mini-composites revealed the surface features and coating thickness of the samples. SEM images of SiCN/CF, Si(B)CN/CF, and Si(Hf)CN/CF ceramic composite samples are shown in Figure 3.5. Figure 3.5(a) compares the uncoated CFs and individual fiber specimen before the ceramic coating; the CMC samples showed shiny, uniform, and continuous ceramic coatings on the surfaces. As shown in Figure 3.5(b), the SiCN coated fibers after pyrolysis were clearly discernible from the uncoated fibers before pyrolysis and the Si(B)CN coating had a smooth, continuous surface free from defects, as shown in Figure 3.5(c). However, for Si(Hf)CN coated fibers (Figure 3.5(d)), ceramic coatings were observed to stick out of the fiber surface coatings after pyrolysis, which is the result of an excessive deposit of preceramic polymers into the CF disc during coating process. For uncoated CFs, the average fiber diameter was measured to be 6 to 7 µm. For SiCN/CF, Si(B)CN/CF, and Si(Hf)CN/CF CMCs the average dimeter was 7-8, 9-12, and 7-8 µm, respectively.

Raman spectra of the CMC samples showed the presence of carbon domains to evaluate corresponding microstructures in the composite materials. As shown in Figure 3.6, the D and G vibrational bands at 1342 and 1600 cm^{-1}, respectively, suggested the presence of "free carbon" structures. The D peaks indicated disordered bands that originated in structural defects and aromatic rings, whereas G peaks were associated with in-plane stretching of sp^2-hybridized carbon atoms[137]. However, the D and G peaks were not pronounced in the Si(Hf)CN/CF sample. This phenomenon was attributed to the strong fluorescence background that was produced under the visible laser source (HeNe 632.8 nm). XPS analysis was later performed to confirm the presence of carbon domains in the Si(Hf)CN/CF sample.

FTIR spectra in Figure 3.7(a-b) shows the characteristic absorption bands of the polymer-

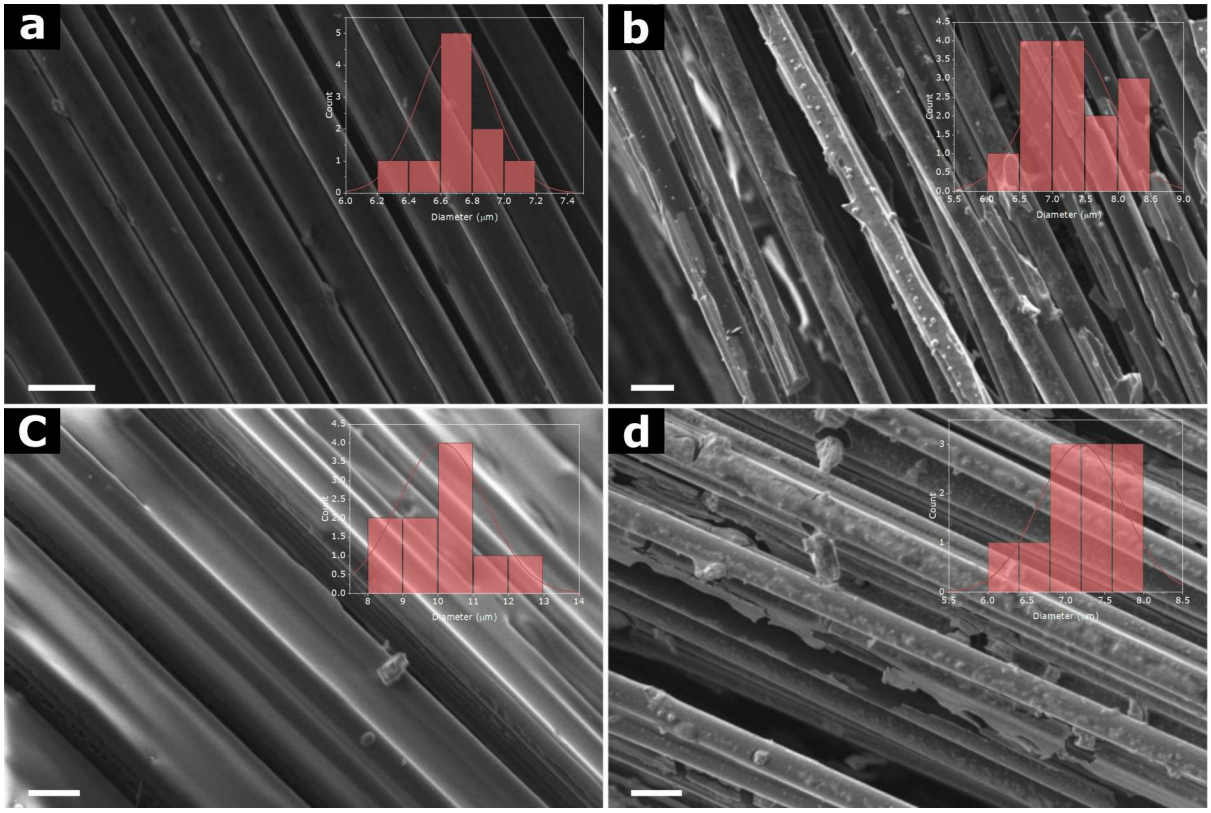

Figure 3.5: *SEM images of CFs with individual fibers before and after ceramic coatings. (a) Uncoated CFs, (b) continuous SiCN coating on the CFs, (c) comparatively thicker ceramic coating (2-4 µm) of Si(B)CN/CF, (c) protruding ceramic coatings for Si(Hf)CN/CF indicate excess amount of preceramic polymers are infused during coating process. The scale bar is 10 µm.*

to-ceramic conversions of the SiCN/CF, Si(B)CN/CF, and Si(Hf)CN/CF samples. For the crosslinked samples in Figure 3.7(a), the peaks at 1060 cm^{-1} and 1260 cm^{-1} corresponded to the stretching of Si-O-Si and Si-CH_3, respectively, in the CMCs[138]. These peaks indicated the presence of Si precursors in the composite samples. For Si(B)CN/CF and Si(Hf)CN/CF samples, the decreased Si-CH_3 and Si_2N-H (1175 cm^{-1}) peak intensities were contributed to the increased crosslinking of the samples at 180 °C . A broad peak of B-N functional group formed in the Si(B)CN/CF sample, and became more intense after pyrolysis (Figure 3.7(b))[139]. A characteristic absorption band of Hf-N-C (945 cm^{-1}) was found in the crosslinked Si(Hf)CN/CF sample, which was overlapped with the Si-CH_3 peaks 10. After pyrolysis, the CMC samples showed two main peaks of Si-O (1060 cm^{-1}) and Si-C (800 cm^{-1}) as presented in Figure 3.7(b). The presence of these two obvious peaks in all the sam-

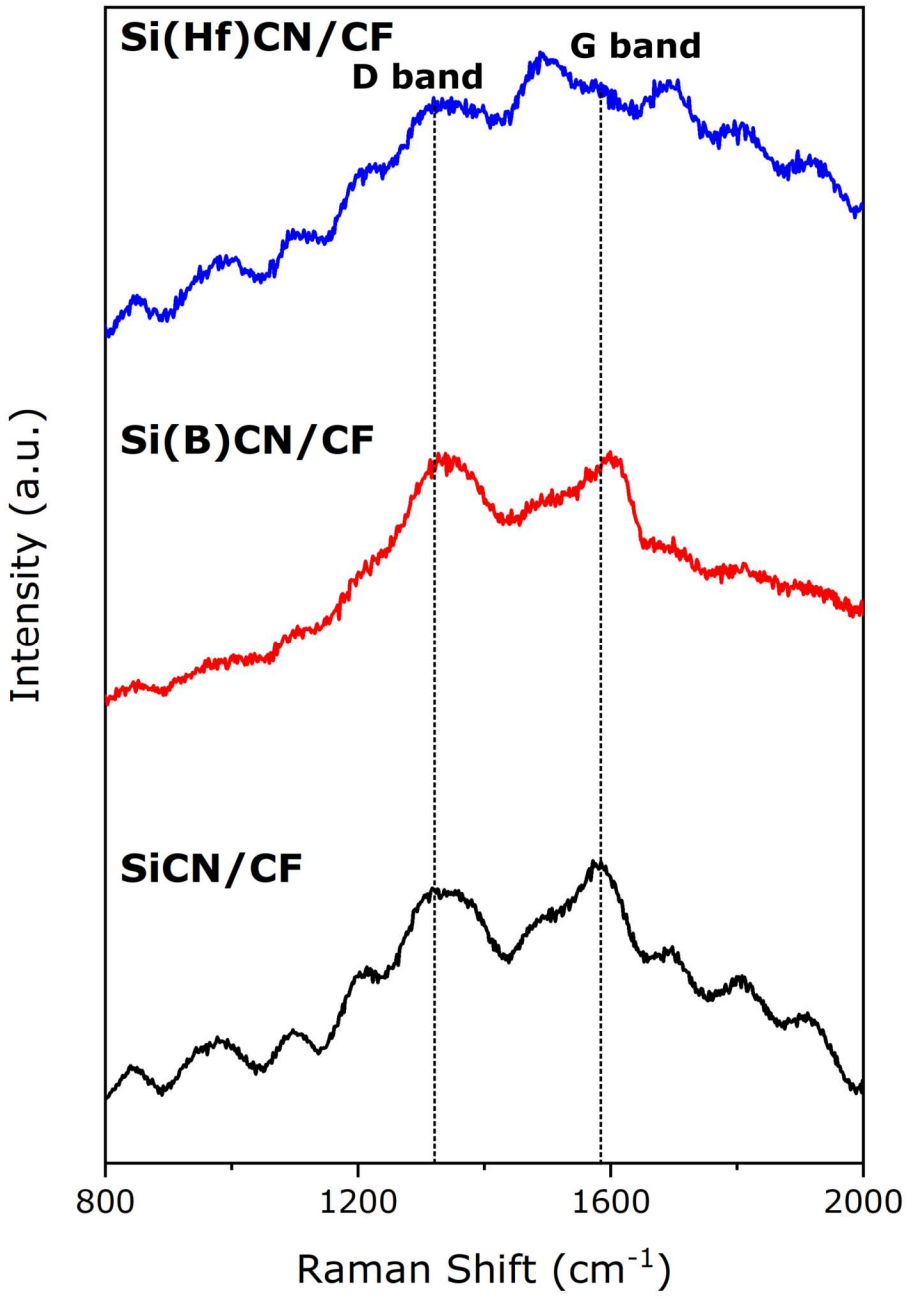

Figure 3.6: *Comparison of Raman spectra for the CMC samples. SiCN/CF, Si(B)CN/CF, and Si(Hf)CN/CF samples show carbon D and G bonds, suggesting the presence of ceramic coatings.*

ples confirmed the existence of ceramic coatings in the composites[140;141]. All characteristic bands of the H-containing functional groups also disappeared indicating the conversion of polymer coatings to ceramic materials.

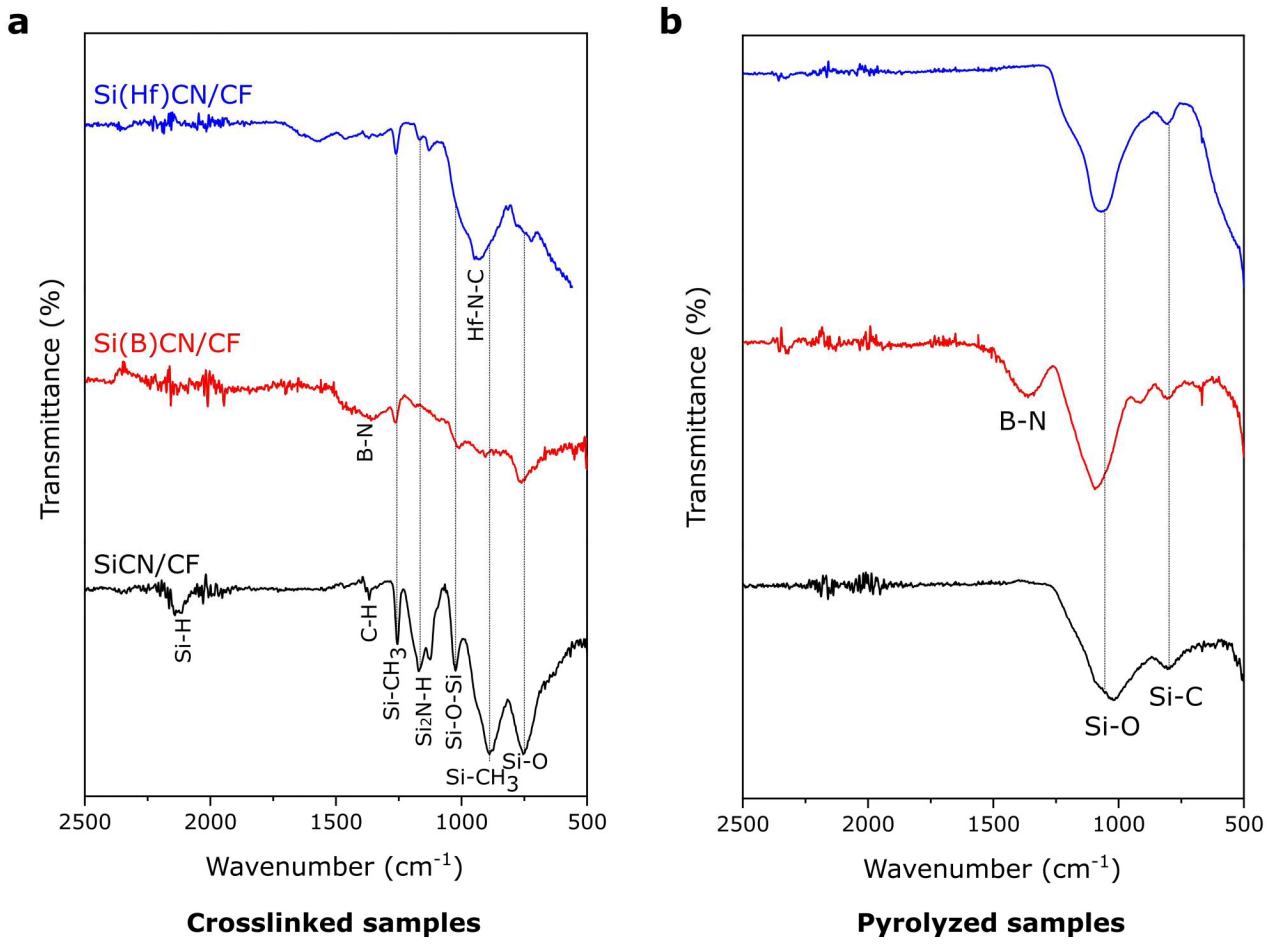

Figure 3.7: *FTIR spectra of ceramic composites after (a) crosslinking, and (b) pyrolysis show the evolution of chemical bonds in the ceramic coatings from the polymer to pyrolyzed stages.*

XPS was performed to determine the elemental composition of the CMC samples and to characterize bonding of the molecules present in the samples. As presented in Figure 3.8, XPS survey scan showed Si2p, C1s, and O1s peaks in all the samples, thereby confirming the presence of ceramic coating on the CFs. An additional B1s peak was found for the Si(B)CN/CF samples, but the N1s peak intensity was suppressed in the survey scan of Si(B)CN/CF. For the Si(Hf)CN/CF sample, the Hf-peaks confirmed the presence of Si(Hf)CN coating on the

CFs. Surface compositions of the CMC samples were determined by integrating the area under the respective elemental peaks and presented in Table 3.2.

Table 3.2: *Elemental composition (at.%) of the CMC mini-composites determined by XPS*

Pyrolyzed samples	Si	C	N	O	B	Hf
SiCN/CF	41.33	9.84	1.32	47.51	-	-
Si(B)CN/CF	40.34	6.84	0.55	49.00	3.27	-
Si(Hf)CN/CF	28.63	13.56	1.51	48.12	-	8.18

Figure 3.9 shows the bonding of various elements in the CMC samples. Fitted peaks under the Si2p (Figures 3.9(a), (e), (j)) for all the samples primarily showed the presence of Si-N (102.4 eV) and Si-C (100.8 eV) bonds, which confirmed the uniform distribution of ceramic coatings on the surface of the CFs. A minimal amount of Si was bonded to the oxygen. Low intensity of the C-Si (284.0 eV) bond under the C1s peak in SiCN/CF (Figure 3.9(b)) and Si(B)CN/CF (Figure 3.9(f)) were attributed to the low carbon content of the samples. In addition, C-C (284.9 eV) and C=O (286.4 eV) were observed in the C1s band[142]. The intense peaks for C-C suggested that most of the carbon phase in the ceramic coating was "free carbon". As shown in Figure 3.9(g), N1s peak in Si(B)CN/CF sample was not fitted due to the low nitrogen content in the sample, as indicated by the survey XPS. In the O1s bands (Figures 3.9(d), (h), (m)), additional peaks for B_2O_3 (533.8 eV) and HfO_2 (530.4 eV) were observed for the Si(B)CN/CF and Si(Hf)CN/CF samples, respectively. In the Si(B)CN/CF sample, boron (Figure 3.9(i)) was primarily bonded to nitrogen (B-N) and oxygen (B-O)[143]. Hf4f band (Figure 3.9(n)) was fitted with two intense peaks at 19.6 and 17.8 eV that corresponded to Hf-O-Si and Hf-O-C, respectively[144;145].

3.5 Conclusions

This study presented a scalable method to fabricate ceramic composites from single-source boron- and hafnium- modified polysilazane precursors. Electron microscopy of the Si(B)CN/CF and Si(Hf)CN/CF samples confirmed the formation of ceramic matrix on the carbon fiber

reinforcements. Raman, FTIR, and XPS characterization techniques outlined the polymer to ceramic conversion stages.

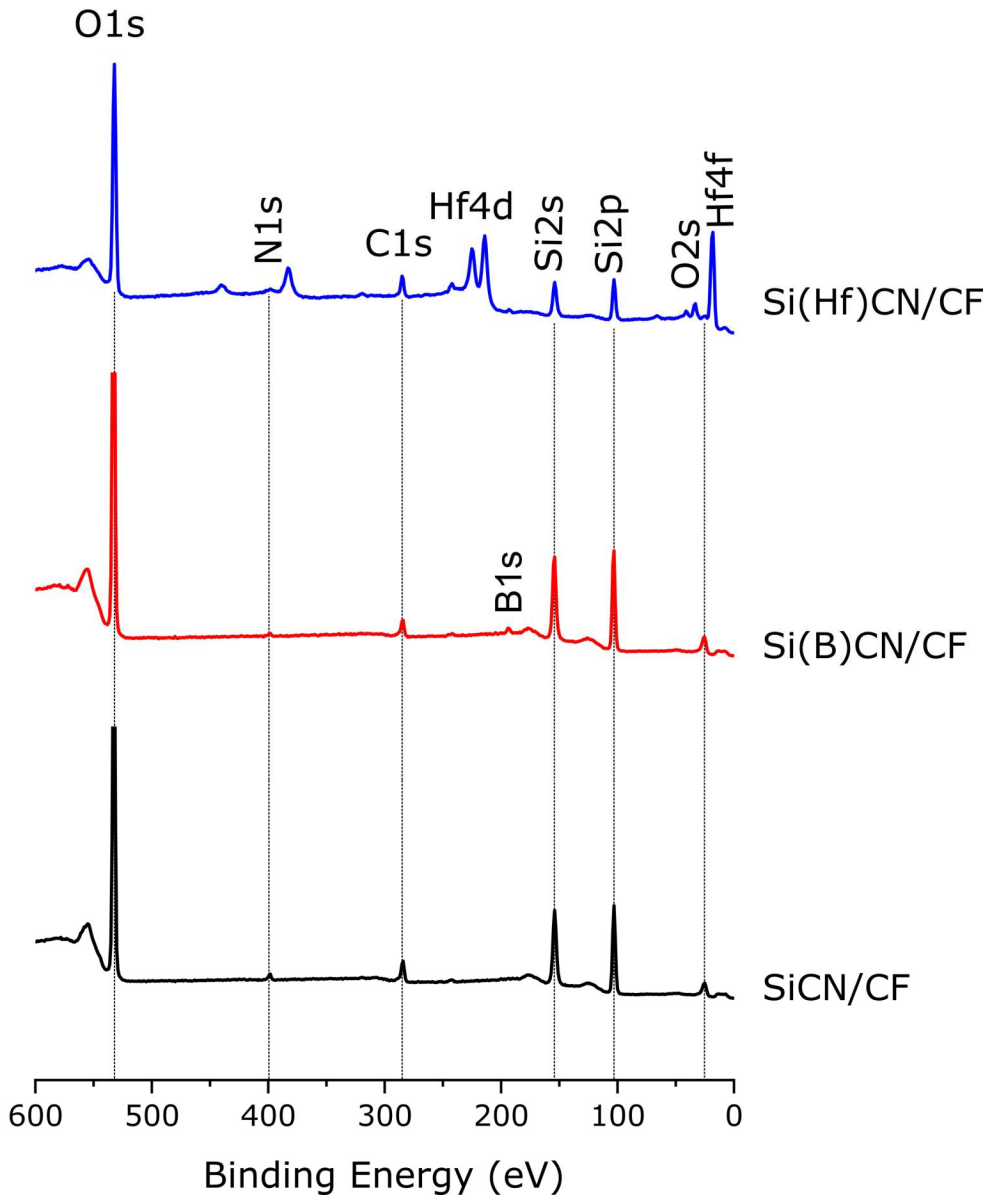

Figure 3.8: *XPS survey spectra of CMC samples. Presence of Si, B, Hf, and N confirms the Si(B)CN and Si(Hf)CN ceramic coating on the fibers. XPS of SiCN/CF coated fibers is included for comparison purposes.*

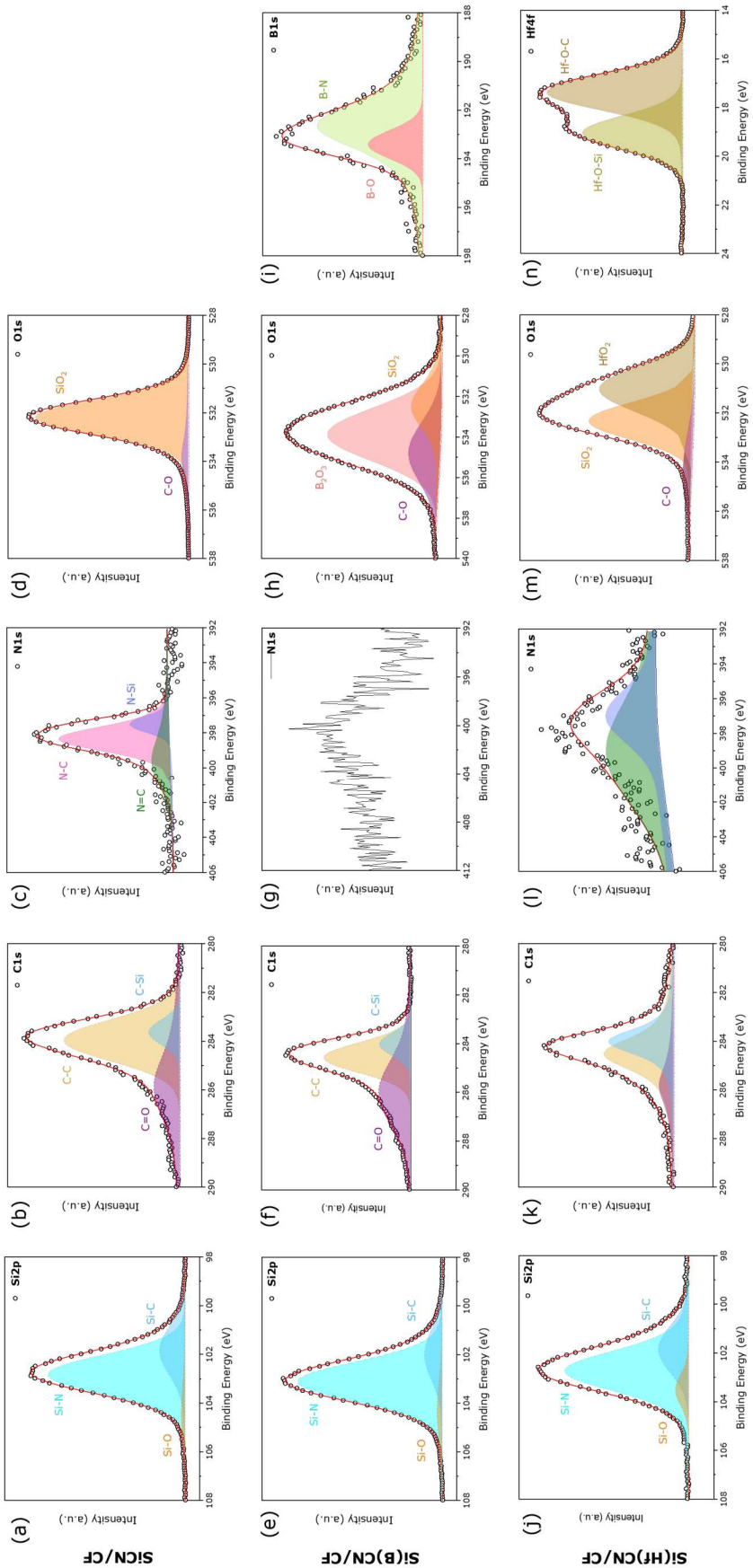

Figure 3.9: *High-resolution XPS spectra of the CMC samples for Si2p, C1s, N1s, O1s, B1s, and Hf4f. (a-d) SiCN/CF, (e-i) Si(B)CN/CF, and (j-n) Si(Hf)CN/CF.*

Chapter 4

Properties of PDC/carbon fiber ceramic-matrix composites

4.1 Preview

Nearly completely dense and defect free ceramic matrix were obtained in Chapter 3. the as-fabricated samples were then subjected to several tests to investigate mechanical properties and oxidation stability. Room-temperature tensile tests showed that the Si(Hf)CN/CF sample could reach a tensile strength of 790 MPa and elastic modulus of 66.88 GPa among the composites. Oxidation study of the mini-composites showed stability of the samples up to 1500 °C. Structural and compositional changes of the samples were also elaborately investigated by XPS and SEM analyses.

4.2 Introduction

Typically, boron-containing PDCs have much higher chemical and thermo-mechanical stability than boron-free counterparts. Although the molecular structure of Si(B)CN is not fully understood yet, the h-BN phase may increase the free activation energy for crystallization and Si-N reaction with C. Because PDCs can be conveniently prepared by controlled heat-

ing and chemical modifications of liquid-phase polymers to take any desired shape, they are useful for defense and aerospace applications[122;136;146;147]. Lee et al. incorporated polymer infiltration and pyrolysis (PIP) to synthesize Si(B)CN CMCs that were stable up to 1500 °C in Ar atmosphere[129]. Weinmann et al. used Si(B)CN ceramics from a boron-modified polysilazane precursor to show the ceramic was stable up to 2000 °C in thermogravimetric analysis (TGA) in an inert gas atmosphere[130]. According to the authors, substantial amounts of Si_3N_4 can affect the high-temperature stability due to the decomposition of Si(B)CN into N_2 and SiC. Kong et al. showed that Si(B)CN ceramics could retain the amorphous structure up to 1600 °C with a boron atomic composition of 6 to 8.5 % in the final ceramic structure[148]. Zhao et al. used sodium borohydride as a boron source to achieve Si(B)CN ceramic, which showed a dense and smooth surface after annealing at 1400 °C[131]. In this liquid-precursor approach, the poly(boro)silazane containing active group Si-H was synthesized via reactions with dichloromethylvinylsilane, hexamethyldisilazane, sodium borohydride, and dimethylchlorovinylsilane under the inert atmosphere.

Similar to Si(B)CN, ceramic composites based on Si(Hf)CN shows promising resistance at high-oxidation temperatures. Ionescu et al. reported improved thermal stability for SiOC/HfO_2 ceramic above 1000 °C compared to hafnia-free SiOC[149]. Thermal stability of the SiOC/HfO_2 nanocomposites was contributed to the in-situ formation of $HfSiO_4$ at elevated temperatures. Sun et al. also presented similar phenomenon in a SiOC/HfO_2-based ceramic composites derived from a polymethylsiloxane modified by various HfO_2 polymorphs[127]. Wen et al. reported the laser ablation behavior of SiHfC-based ceramics prepared from a single-source precursor[133]. They showed that the incorporation of Hf into the SiC-based ceramics enables the composites to withstand ultrahigh temperature (approx. 3000 °C) in a short period of time (0.5 s) proving the excellent thermal shock resistance of the SiHfC-based ceramics.

The current work aimed to study the effect on the mechanical property and oxidation stability of the as-fabricated mini-composites mentioned in Chapter 3. Preliminary mechanical tests performed on the composites bundle showed that Si(Hf)CN/CF had the highest tensile strength of 790 MPa and elastic modulus of 66.88 GPa among the ceramic mini-composites.

An oxidation study in ambient air of the ceramic mini-composites showed sample stability up to 1500 °C in air. Structural and compositional changes of the oxidized samples were investigated via XPS and SEM analyses.

4.3 Characterization technique

To determine the mechanical properties of composites, tensile tests of the CMCs were performed using a Shimadzu AGS-X Universal Testing Machine with a 5 KN load cell.

To understand the oxidation stability of the CMCs, the samples were heated to 800 °C, 1000 °C, 1200 °C, and 1500 °C in stagnant air in a SentroTechTM box furnace with a heating rate of 5 °C min_{-1}.

4.4 Mechanical properties

Mechanical properties of the CMC mini-composites were determined by tensile test of the composite bundles. Rectangular composite bundle samples were prepared using CF bundles collected from the CF cloth. Each bundle contained 6000 individual carbon fibers. The composites were mounted onto cardboard tabs using epoxy for the tests as reported in previous works[150;151]. Each cardboard tab had a 30 mm slot in the middle, which was the gauge length of the tensile specimens as shown in Figure 4.1(a). The cardboard tabs were cut on the sides after mounting the samples in the tester and prior to load application. During tests the load was applied at a rate of 0.2 mm min^{-1} to maintain a quasi-static tensile condition.

The tensile behavior of the samples is shown in Figure 4.1(b) and the results are reported in Table 4.1. The Si(Hf)CN/CF composite showed the highest average strength of 790 MPa, followed by SiCN/CF and Si(B)CN/CF samples with average strengths of 390 and 110 MPa, respectively. The Si(Hf)CN/CF sample also showed the highest Young's modulus of 66.88 GPa, whereas the SiCN/CF and Si(B)CN/CF composites showed a Young's modulus of 49.89 and 30.58 GPa, respectively. The tensile strength of the uncoated CF bundles was also

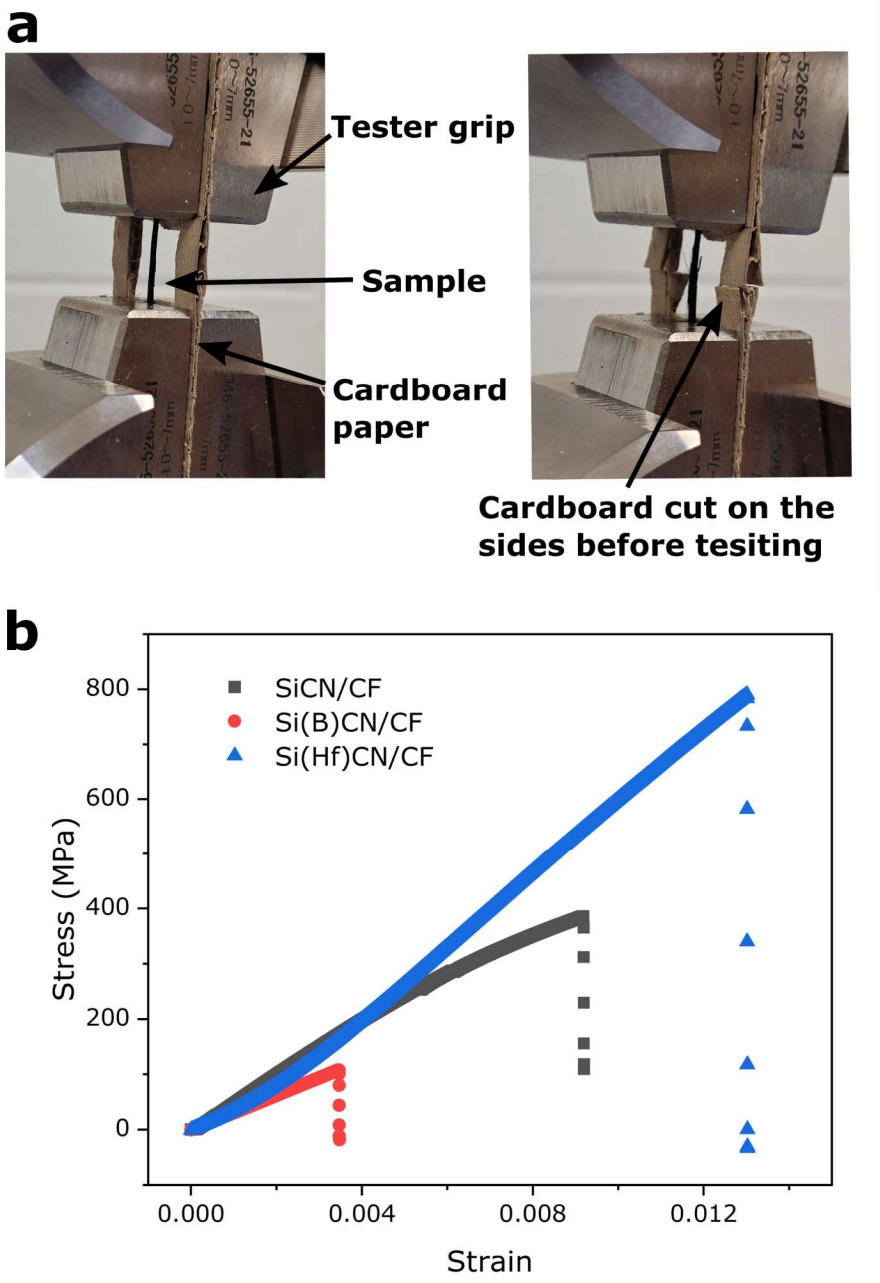

Figure 4.1: *Tensile test of the PDC/CF composites. (a) Tensile test set-up. Samples are mounted on cardboards which are cut prior to the tests, (b) stress vs. strain plots of the CMC samples. The tensile strength of the uncoated CF bundles was also measured for comparison purposes.*

measured for comparison purposes and presented in Figure 4.2. The average tensile strength of the uncoated fibers was measured to be 2.3 GPa, which was higher than the composites. This behavior is typical in PIP-processed composites where the strength of composite is lower than the pristine fibers[114;152]. This behavior is primarily due to localized stress concentration on adjacent fibers induced from the cracks in matrix of a CMC. Crack formation in CMC matrix typically occurs during the hydrogen evolution and transformation into the ceramic phase. In addition, mechanical and thermal damage of the fibers during composite processing results in low strength of the composite[153]. The average tensile strength of the heated CFs (at 800 ℃ in N_2 environment) was 0.45 GPa (presented in Table 4.1), which was almost five times lower than the strength of neat uncoated CFs. The strain-to-failure of the composites (Figure 4.3) was also lower than the uncoated fibers, indicating the abrupt mechanism of fracture of the samples.

Table 4.1: *Tensile properties of the uncoated CFs and PDC/CF CMCs*

Sample	Strength at failure (GPa)	Young's modulus (GPa)	Strain to failure (%)
CF1	2.31	76.41	6.32
CF2	2.46	76.22	8.47
CF3	2.37	72.58	6.06
Heated CF1	0.38	45.75	5.68
Heated CF2	0.37	31.18	4.02
Heated CF3	0.58	31.01	2.01
SiCN/CF1	0.38	24.75	2.21
SiCN/CF2	0.29	61.51	0.53
SiCN/CF3	0.39	49.89	0.92
Si(B)CN/CF1	0.11	30.58	0.34
Si(B)CN/CF2	0.092	30.26	0.36
Si(B)CN/CF3	0.11	21.97	0.58
Si(Hf)CN/CF1	0.79	66.88	1.31
Si(Hf)CN/CF2	0.73	56.91	2.04
Si(Hf)CN/CF3	1.01	59.19	1.55

The oxidation behaviors of PDC/CF mini-composites at various oxidation temperatures are shown in Figure 4.4. The samples were oxidized at 800, 1000, 1200, and 1500 °C in stagnant air, which were labeled PDC/CF800, PDC/CF1000, PDC/CF1200, and PDC/CF1500,

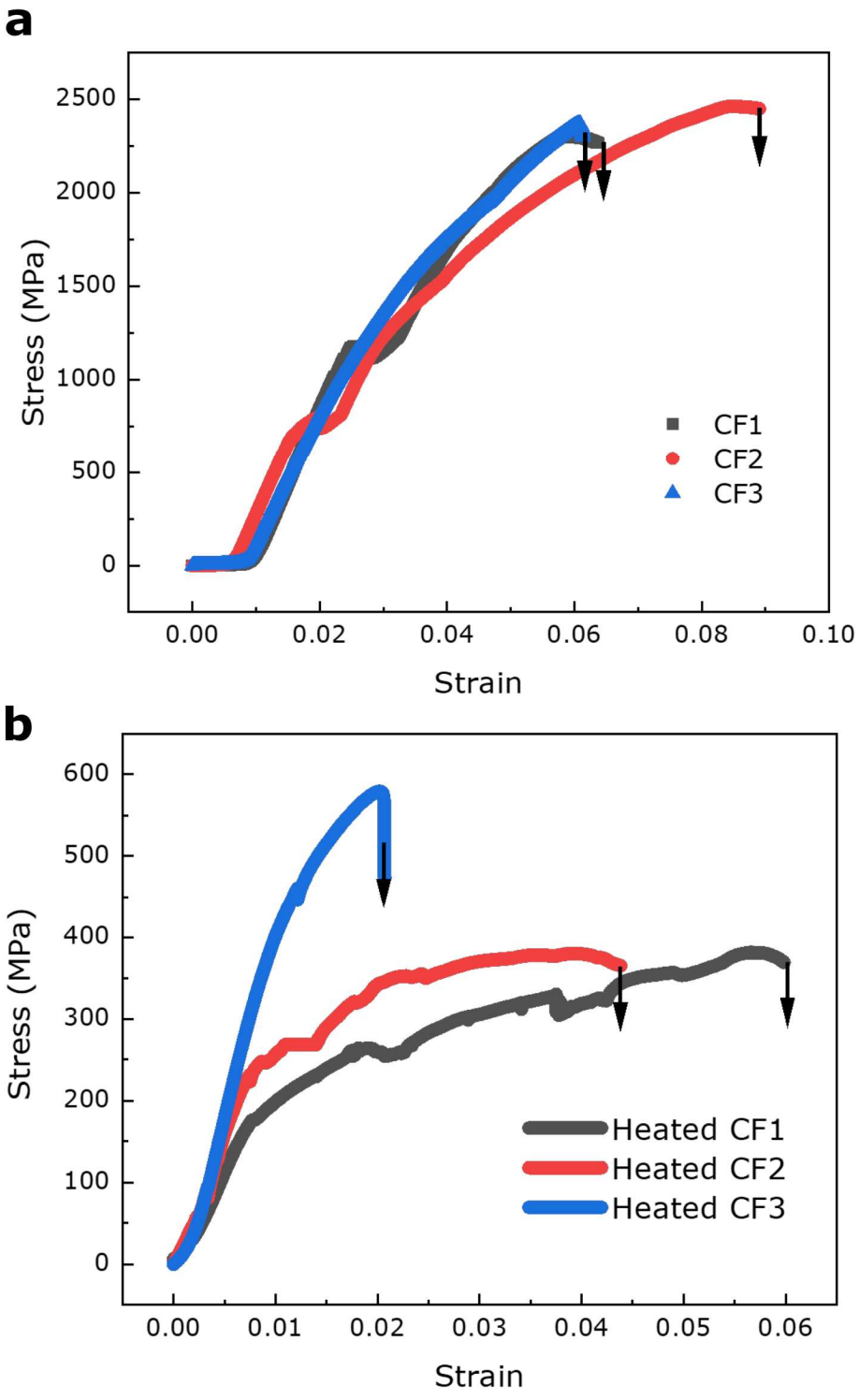

Figure 4.2: *Stress-strain curves of the uncoated CFs samples: (a) before heating and (b) after heating at 800 ℃ in N_2 environment).*

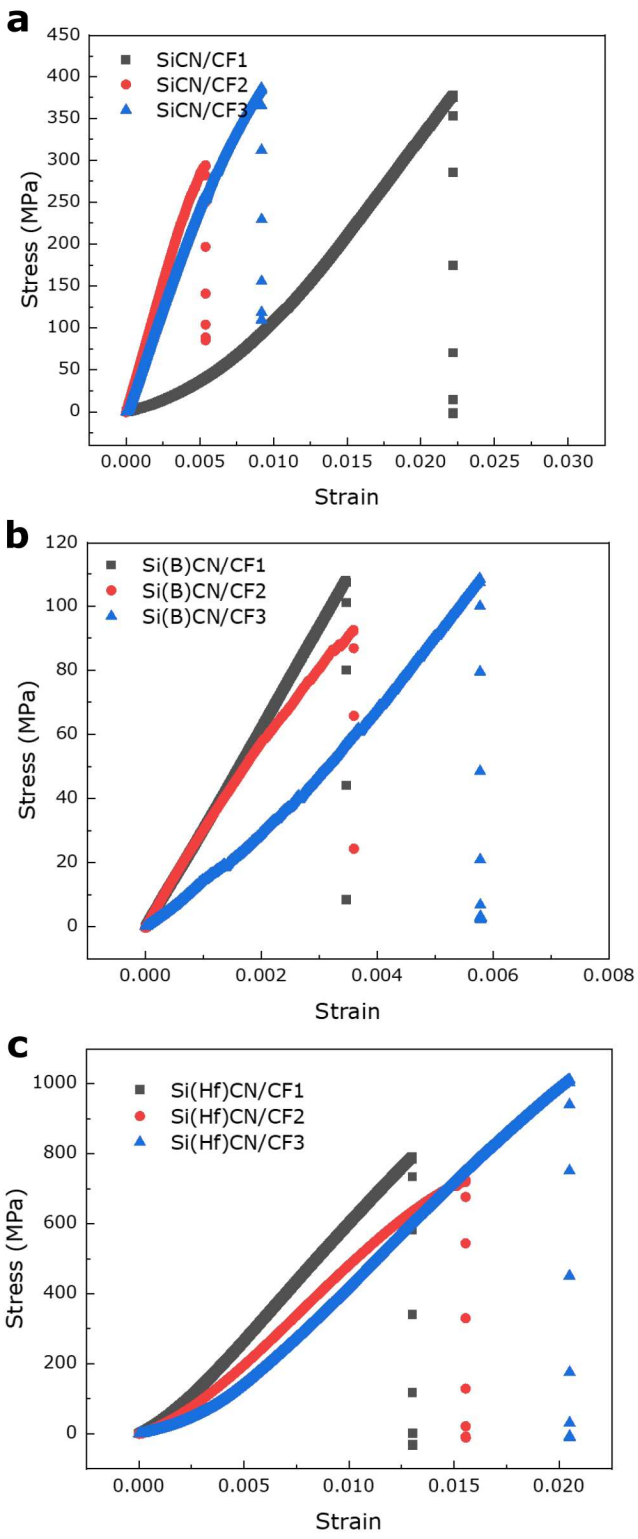

Figure 4.3: *Stress-strain curves of three samples from each type of PDC/CF.*

respectively. The uncoated CFs were used as a contrast sample with the ceramic composites in an oxidation experiment. Results showed that the PDC/CF samples survived the high oxidation environments, whereas the uncoated CFs did not. Figure 8 also shows that the SiCN/CF samples started disintegrating above 1000 ℃, whereas the Si(B)CN/CF samples exhibited deformation in the shape. The Si(Hf)CN/CF sample turned white on the surface indicating the formation of HfO_2[154]. The weight retention of the samples after oxidation is reported in Table 4.2. The Si(B)CN/CF samples showed highest resistance to oxidation in terms of weight retention, while the Si(Hf)CN/CF samples showed less retention with more uniform weight changes and less significant differences at higher temperature.

Table 4.2: *Weight retention (%) of PDC/CF samples after oxidation at various temperatures.*

Oxidized Samples	800 ℃	1000 ℃	1200 ℃	1500 ℃
SiCN/CF	20	20	18	18
Si(B)CN/CF	35	34	33	30
Si(Hf)CN/CF	27	21	20	19

Morphology of the oxidized CMCs were also obtained as shown in Figure 4.5. The SEM of each composite was evaluated to delineate the oxidation behavior of the CMCs after heating. For SiCN/CF samples, the composites began disintegrating and the fibers dispersed after heating at 1000 ℃, as shown in the SEM micrographs of SiCN/CF1200 and SiCN/CF1500 samples in Figure 4.5. These results correspond to the oxidized sample digital images in Figure 4.4. For Si(B)CN/CF samples, the composites showed shape deformation and shrinkage after 1200 ℃. SEM image of the Si(B)CN/CF1500 sample showed that the composite structure melted at 1500 ℃ and formed a thin film. However, Si(Hf)CN/CF samples showed high oxidation resistance up to 1500 ℃, and the fiber-matrix structures of the samples showed minimal damage, even at 1500 ℃.

To validate these results, the oxidation behavior of PDC/CF composites at various oxidation temperatures were also evaluated by XPS. Table 4.3 presents the elemental composition of the oxidized samples at different temperatures. The increased amount of oxygen in all

the samples indicated the oxidation levels of the CMC samples. The most significant increase occurred for the SiCN/CF samples due to the oxidation of SiC and Si_3N_4 in the composites[155], which led to formation of SiO_2 and eventual decreased stability. Oxidation of the Si(B)CN/CF samples resulted in the formation of SiO_2 and B_2O_3[156]. The borosilicate (B_2O_3) melted at higher temperatures (1000 °C), spread on the surface, and combined with SiO_2, preventing further oxidation of the samples. This phenomenon correlated to the high weight retention of Si(B)CN/CF1200 and Si(B)CN/CF1500 samples, although the sample shapes deformed at higher temperatures. For the Si(Hf)CN/CF samples, the formation of HfO_2 and $Si_xO_yHf_z$ during heating contributed to the oxidation resistance of the samples. The $Si_xO_yHf_z$ liquid phase at higher temperatures limited the diffusion of oxygen and the formation of HfO_2 acted as a grip to hold the $Si_xO_yHf_z$ in place preventing further oxidation[157].

Table 4.3: *Comparison of elemental compositions (at.%) of oxidized samples determined by XPS.*

Oxidized Samples	Si	C	N	O	B	Hf
SiCN/CF800	30.88	15.87	0.26	52.99	-	-
SiCN/CF1000	26.07	9.03	0.31	64.59	-	-
SiCN/CF1200	30.85	11.89	0.27	56.98	-	-
SiCN/CF1500	29.58	12.93	0.27	57.21	-	-
Si(B)CN/CF800	20.78	15.12	0.78	51.64	11.69	-
Si(B)CN/CF1000	21.62	14.79	0.44	50.43	12.72	-
Si(B)CN/CF1200	25.01	8.28	0.7	53.05	12.97	-
Si(B)CN/CF1500	26.73	2.06	0.16	60.4	10.65	-
Si(Hf)CN/CF800	22.74	19.7	1.61	51.15	-	4.8
Si(Hf)CN/CF1000	23.87	15.82	1.41	55.01	-	3.89
Si(Hf)CN/CF1200	20.22	22.43	1.72	48.22	-	7.4
Si(Hf)CN/CF1500	24.03	10.67	1.84	56.62	-	6.84

4.5 Conclusions

This study evaluated the as-fabricated mechanical properties and oxidtion stability of the precursor-derived CMC mini-composites. Of the CMC mini-composites, the Si(Hf)CN/CF

sample showed the highest mechanical strength of 790 MPa and elastic modulus of 66.88 GPa. Efficiency of the oxidation resistance was also evident in all the SiCN/CF, Si(B)CN/CF, and Si(Hf)CN/CF CMC samples in spite of the complex architecture of the fiber and matrix damage. However, Si(Hf)CN/CF showed oxidation resistance up to 1500 ℃ due to the formation of $Si_xO_yHf_z$ liquid phase at higher temperatures (1000 °C) with HfO_2.

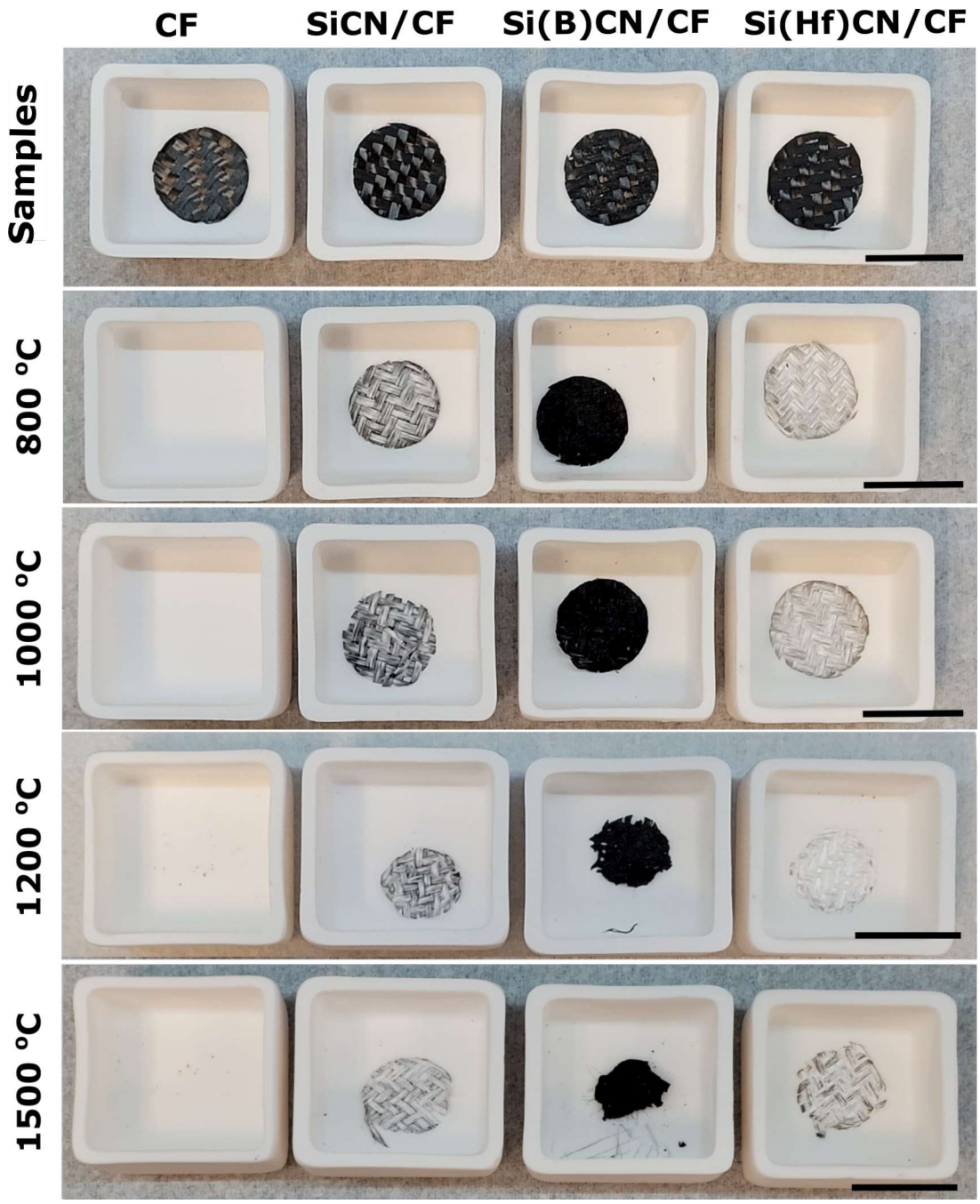

Figure 4.4: *Post-oxidation behavior of the uncoated CF and PDC/CF samples at various temperatures. The PDC/CF samples show high resistance to oxidation up to 1500 ℃. Scale bar is 2 cm.*

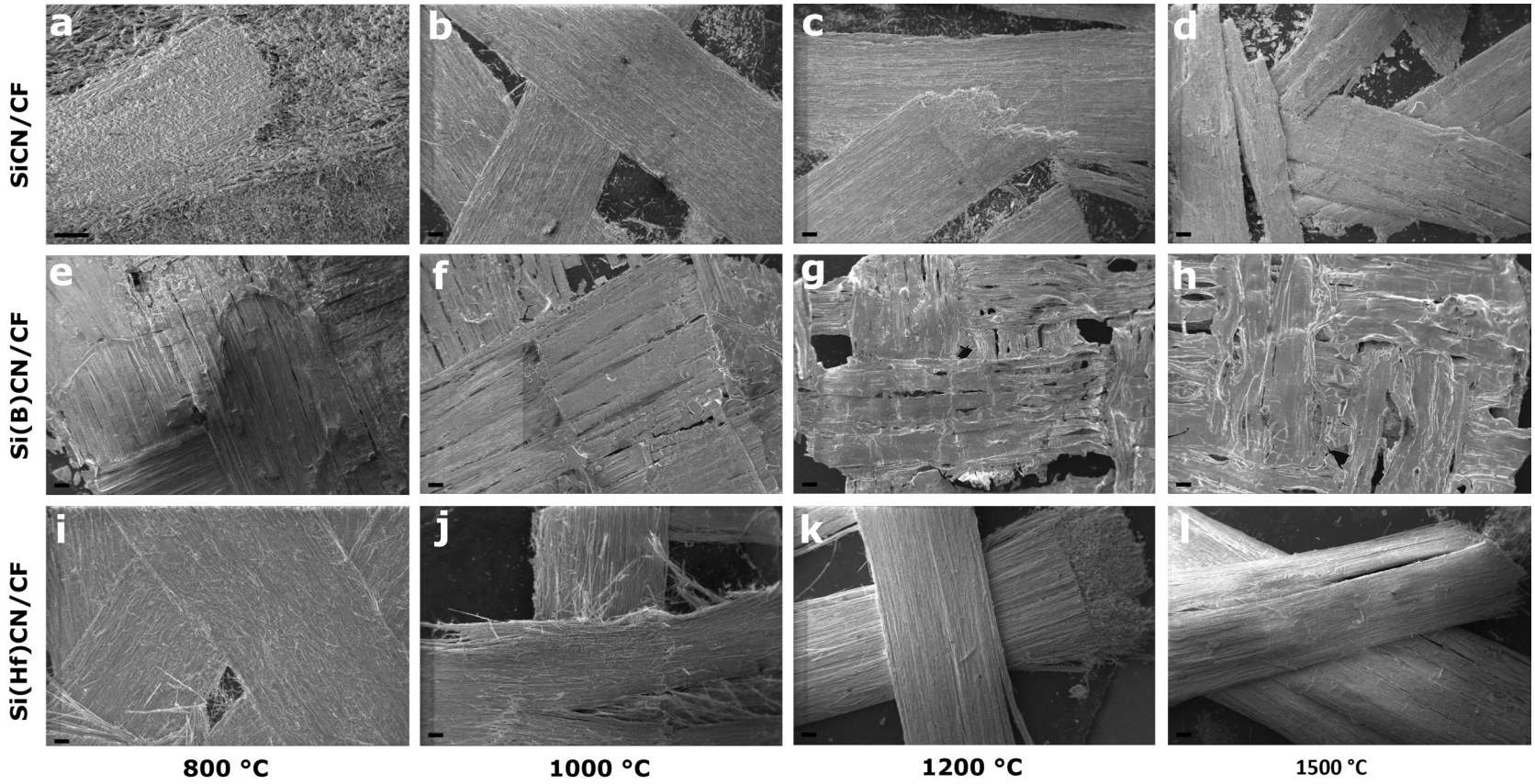

Figure 4.5: *Post-oxidation behavior of the uncoated CF and PDC/CF samples at various temperatures: (a) SiCN/CF800, (b) SiCN/CF1000, (c) SiCN/CF1200, (d) SiCN/CF1500, (e) Si(B)CN/CF800, (f) Si(B)CN/CF1000, (g) Si(B)CN/CF1200, (h) Si(B)CN/CF1500, (i) Si(Hf)CN/CF800, (j) Si(Hf)CN/CF1000, (k) Si(Hf)CN/CF1200, (l) Si(Hf)CN/CF1500. The PDC/CF samples show high resistance to oxidation up to 1500 ℃. Scale bar is 200 μm.*

Chapter 5

Fabrication of self-supporting SiOC ceramic fibermat[1]

5.1 Preview

Fabrication of precursor-derived ceramic fibers as electrode for energy storage applications remains largely unexplored. Within this work, three little known polymer-derived ceramics (PDC)-based fibers are being studied systemically as potential high-capacity electrode materials for electrochemical energy devices. We report fabrication of precursor-derived SiOC fibermats via one-step spinning from varying composition of siloxane oligomers followed by stabilization and pyrolysis at 800 °C. Electron microscopy, Raman, FTIR, XPS, and NMR spectroscopies reveal transformation from polymer to ceramic stages of the various SiOC ceramic fibers. The ceramic samples are few microns in diameter with free carbon phase embedded in the amorphous Si-O-C structure.

[1]Reprinted from Mujib, S. B., Ribot, F., Gervais, C., and Singh, G. (2021). Self-supporting carbon-rich SiOC ceramic electrodes for lithium-ion batteries and aqueous supercapacitors. *RSC advances*, 11(56), 35440-35454.

5.2 Introduction

Efforts related to development and use of nanostructured silicon-based electrodes (utilizing the size effect to achieve fast Li-ion transport, and prevent fracture propagation in electrodes), in the form of nanoparticles[158–161],nanotubes and nanowires[162–166], and composite nanoparticles with carbon[167–172] are now well-documented. Nevertheless, capacity decay over a long period of charge/discharge, high first cycle loss, high cost of material synthesis, and challenges associated with scalability limit their applications as electrodes for commercial applications.

Since the development of electrospinning in 1930s by Formhlas[173;174], the technique has been explored to fabricate a variety of artificial fibers from homogenous polymer solution using high potential electric field. Nanofibers produced by electrospinning can provide large surface area, exceptional tolerance against mechanical deformation with improved electrical conductivity and enhanced electrochemical performance. For example, electrospinning of PAN nanofibers with Si nanoparticles delivered a flexible electrode after carbonization that showed a high capacity of 1600 mAh g^{-1} in LIBs[175]. Xiao et al. reported a stretchable PVDF nanofiber membrane which was coated with Ni and Si to form a Si/Ni/PVDF core-shell structure[176]. This soft silicon electrode showed 56.9% capacity retention after 1000 cycles with 20% stretching capability.

Herein, we report on the fabrication of freestanding, binder-free SiOC electrodes by an electrospinning method using liquid precursor polymer, followed by thermal treatment and pyrolysis. Three new types of SiOC precursors, that are readily available, and easy to draw into low-cost, high-yield ceramic fibers compared to commercial ceramic fibers[177;178], are utilized in this study both for LIBs and supercapacitors. To the best of our knowledge such siloxanes have not been reported before for the fabrication of SiOC ceramic fibermats, that are investigated in electrochemical devices. Scanning- and transmission-electron microscopy reveals uniform, defect-free amorphous structure of the SiOC fibers. Fourier transform infrared spectroscopy (FTIR) and nuclear magnetic resonance (NMR) are utilized to study the polymeric precursor to ceramic transformation of the siloxanes, whereas Raman spectroscopy

and X-ray photoelectron spectroscopy (XPS) confirms the presence of "free carbon" content.

5.3 Experimental

5.3.1 Materialsl

Three types of commercially available oligomers precursors to silicon oxycarbide ceramic were sourced from Gelest, Inc. (Pennsylvania, USA). These SiOC precursors: (1) 1,5-Divinyl-3,3-Diphenyl-1,1,5,5-Tetramethyltrisiloxane (cited as DDTS), (2) 1,3-Divinyltetramethyldisiloxane (cited as DTDS), and (3) 1,3,5-Trivinyl-1,1,3,5,5-Pentamethyltrisiloxane (cited as TPTS) as shown in Figure 5.1 have comparable chemical structures with vinyl groups which are potential crosslinking groups. Figure 5.1 shows the compositions of the precursors where silicon (Si) to oxygen (O) atom ratio for DDTS and TPTS is 3:2 and for DTDS is 2:1.

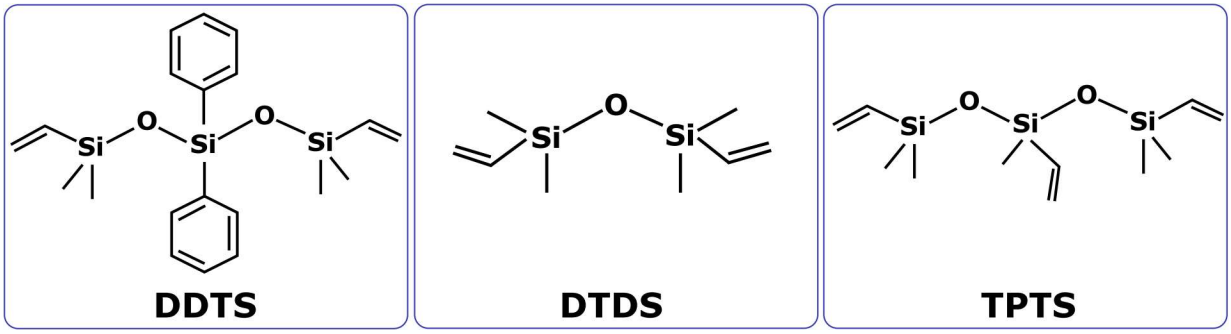

Figure 5.1: *Molecular structure of three pre-ceramic silicon oligomers used in this study.*

To accomplish electrospinning of the preceramic oligomers 10 wt.% of polyvinylpyrrolidone (PVP) with Mw 1,300,000 g mol^{-1} (Sigma Aldrich, Missouri, USA) was used as a spinning agent. Dicumyl peroxide (Sigma Aldrich, Missouri, USA) was used as a crosslinker for the oligomers and Iso-propanol (Fisher Scientific, Massachusetts, USA) was used as a solvent. Ultra-high purity argon (Ar) gas was used for inert environment during pyrolysis which was supplied by Matheson (Kansas, USA).

5.3.2 Electrospinning and synthesis of fibermat

Various SiOC fibermat samples were fabricated via electrospinning of polymer solutions, followed by stabilization and pyrolysis at elevated temperatures. The electrospinning setup that was designed and built in the lab consisted of four major parts[177]: (1) A syringe which is controlled with a stepper motor works as a feeder for polymer solution; (2) A voltage source (up to 30 kV) that controls the amount of electrical charge applied to the solution; (3) An aluminum roller that works as a fibermat collector; and (4) A microcontroller made of Arduino that controls the motors' speed and the sensors. The major parts of the setup are illustrated in Figure 5.2.

The electrospinning solution was prepared by dissolving 10 wt.% of PVP in 7500 mg of Iso-propanol; after that preceramic oligomer was added into the solution with a weight ratio of 3:1 to PVP. DCP as a crosslinking catalyst was already dissolved into the preceramic oligomer, which was 1 wt.% of the siloxane oligomer. The solution was then stirred for about 2 hrs to get a homogenous mixture of PVP and preceramic oligomer. The solution was then poured into the feeder syringe. During electrospinning, the feed rate was set at 5 mL h^{-1} while the voltage supply was maintained at 15 kV. The positive output was connected to the syringe nozzle and the collector was grounded. The nozzle to collector distance was set to 25 cm. The collector was wrapped with an Al foil and a fibermat of 15x15 cm^2 was collected onto the foil after the electrospinning. The electrospun raw or as-spun fibermat is shown in Figure 5.2(b).

5.3.3 Crosslinking and pyrolysis of the fibermat

The electrospun fibermats of the three siloxanes were dried at room temperature overnight and then crosslinked at 300 °C in an oven for 8 h in the presence of air. The crosslinked fibermats (Fig 5.2c) were then pyrolyzed in an alumina tube furnace at approx. 800 °C for 30 min in flowing Ar gas. The heating rate was approx. 2 °C min^{-1} and Ar gas flow rate was 5 mL min^{-1} in the furnace. The crosslinked fibermats were cut into smaller rectangular shape (50x25 mm_2) to fit in the aluminum ceramic boat that was used to hold the samples

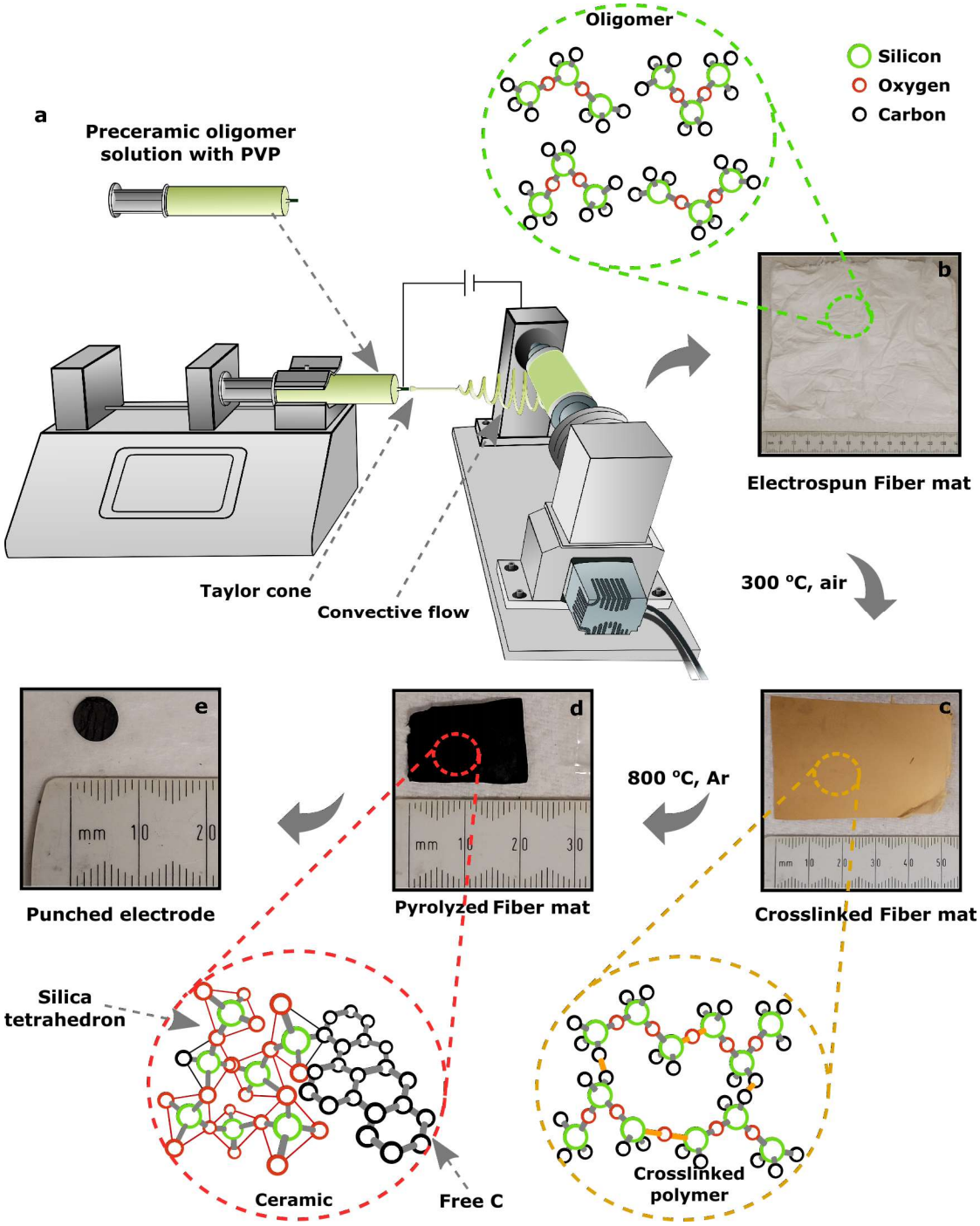

Figure 5.2: *Fabrication of SiOC ceramic fibermats via electrospinning process. (a) Electrospinning set-up, (b) as-spun fibermat collected to from the roller, (c) fibermat after crosslinking at 300°C in air, (d) fiber mat after pyrolysis at 800°C in Ar environment, and (e) a 6.35 mm dia. electrode punched out from the ceramic fibermat.*

in the furnace during pyrolysis. The fibermat polymer-to-ceramic conversion was complete at 800 °C; a representative of SiOC ceramic fibermat is shown in Figure 5.2(d). The lateral shrinkage during polymer-to-ceramic conversion for DDTS-derived SiOC ceramic fibermat was 40%, whereas for DTDS- and TPTS- derived SiOC ceramic fibermats were 60% and 55% respectively.

5.3.4 Characterization techniques

Several material characterization techniques were employed to determine the morphological, compositional, and chemical conversions at various stages of processing of the fibers- as-spun, crosslinked, and pyrolyzed fibermats. The images of surface features, shapes, and diameters of the fibers in the SiOC ceramic fibermats were investigated using a FEI Nova NanoSEM 450 scanning electron microscope (SEM). An FEI Tecnai Osiris 200 kV (scanning) transmission electron microscope (TEM) was used to obtain morphological and crystallographic information as well as energy dispersive X-ray (EDX) mapping analysis of the ceramic fibermats.

To determine the molecular structure and chemical interactions of the ceramic fibermats Raman spectroscopy and Fourier-transform infrared spectroscopy (FTIR) were used. Raman analysis in the range of 800–2000 cm^{-1} was performed to determine mainly the carbon vibrational modes using a confocal micro-Raman microscope (Horiba Jobin Yvon LabRam ARAMIS) equipped with a HeNe laser source (632.8 nm). The presence and evolution of various chemical functional groups of the siloxane precursors in the fibermats were investigated using a Perkin Elmer Spectrum 400 FTIR spectrometer in the range of 500-3500 cm^{-1}.

To further investigate the chemical bonds in each sample, nuclear magnetic resonance (NMR) spectroscopy was used. A Bruker AVANCE 300 spectrometer was used to record solid-state ^{13}C CP MAS and ^{29}Si MAS NMR spectra using following specifications (B_0 = 7.0 T, $\nu_0(^1\text{H})$ = 300.29 MHz, $\nu_0(^{13}\text{C})$ = 75.51 MHz, $\nu_0(^{29}\text{Si})$ = 59.66 MHz), and a 4 mm Bruker probe and spinning frequency of 10 kHz. ^{13}C CP MAS experiments were recorded

with ramped amplitude cross-polarization in the ^{1}H channel to transfer magnetization from ^{1}H to ^{13}C (recycle delay = 3 s, CP contact time = 1 ms, optimized ^{1}H spinal-64 decoupling). Single-pulse ^{29}Si NMR MAS spectra were recorded with recycle delays of 60 s. Liquid-state NMR spectra were recorded on a Bruker AVANCE 300 spectrometer (B_0 = 7.0 T, $\nu_0(^{1}H)$ = 300.13 MHz, $\nu_0(^{13}C)$ = 75.47 MHz, $\nu_0(^{29}Si)$ = 59.63 MHz). Chemical shift values were referenced to tetramethyl silane for ^{13}C and ^{29}Si.

X-ray photoelectron spectroscopy (XPS) was carried out to analyze the surface composition using a Thermo Scientific Al K+ ion beam (beam energy = 1486.6 eV and spot size = 400 µm) XPS. To remove the surface contamination of the ceramic fiber mats, initial sputtering of the surface with Ar+ at 3.0 keV for 2 min was performed.

5.4 Micro-structure and morphology of fibermats

SEM and TEM images of the pyrolyzed samples revealed the surface and internal features of the SiOC fibers. Figure 5.3 shows that SiOC fibermats fabricated from the three siloxane oligomer samples were largely uniform in diameter along the fiber length. For DDTS-derived SiOC fibers (Figure 5.3(a)) the average fiber diameter was between 1-3 µm, whereas for DTDS- and TPTS-derived SiOC fibers (Figure 5.3(b-c)) the average dimeter stayed between 0.2-1.5 µm. SiOC fibers derived from the siloxane oligomer with high molecular weight resulted in large diameter fibers compared to low molecular weight precursors. Furthermore, high molecular weight precursor produced thick and dense fibers as can be seen from the inset of the high-resolution SEM images (Figure 5.4). The thinner and hollow fibers derived from the DTDS and TPTS may have resulted from the steric hindrance, and molecular weight difference with the PVP (spinning agent) during the spinning process[177]. As a result, in our case of single-nozzle electrospinning, the PVP molecules moved to the inner layers and preceramic polymer stayed in the outer layers, and the separation likely occurred during the crosslinking and pyrolysis processes[179]. The core-shell structure of the hollow TPTS-derived SiOC fibers was also confirmed by TEM (Figure 5.5).

In addition, SEM and TEM revealed a smoother surface for DDTS- and DTDS-SiOC

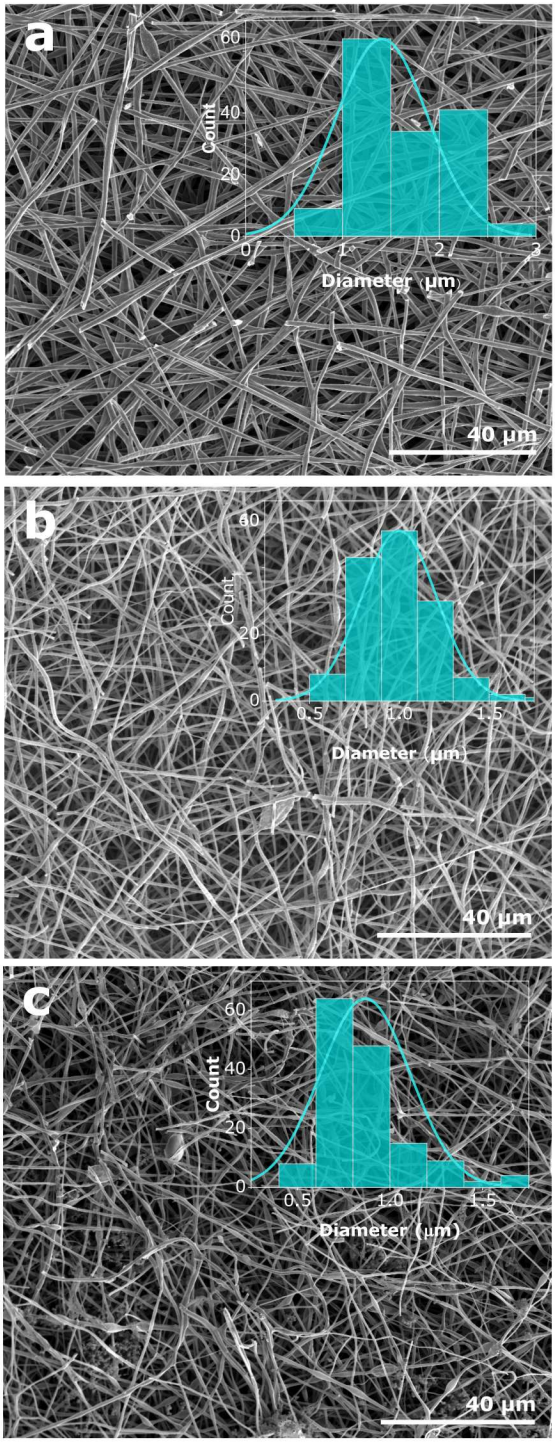

Figure 5.3: *Diameter distribution measured from SEM images of the electrospun SiOC fibermats: (a) DDTS-derived SiOC, (b) TPTS-derived SiOC, (c) DTDS-derived SiOC. For DDTS-derived SiOC fibers the average fiber diameter was between 1-3 µm, whereas for DTDS- and TPTS-derived SiOC fibers the average dimeter stayed between 0.2-1.5 µm.*

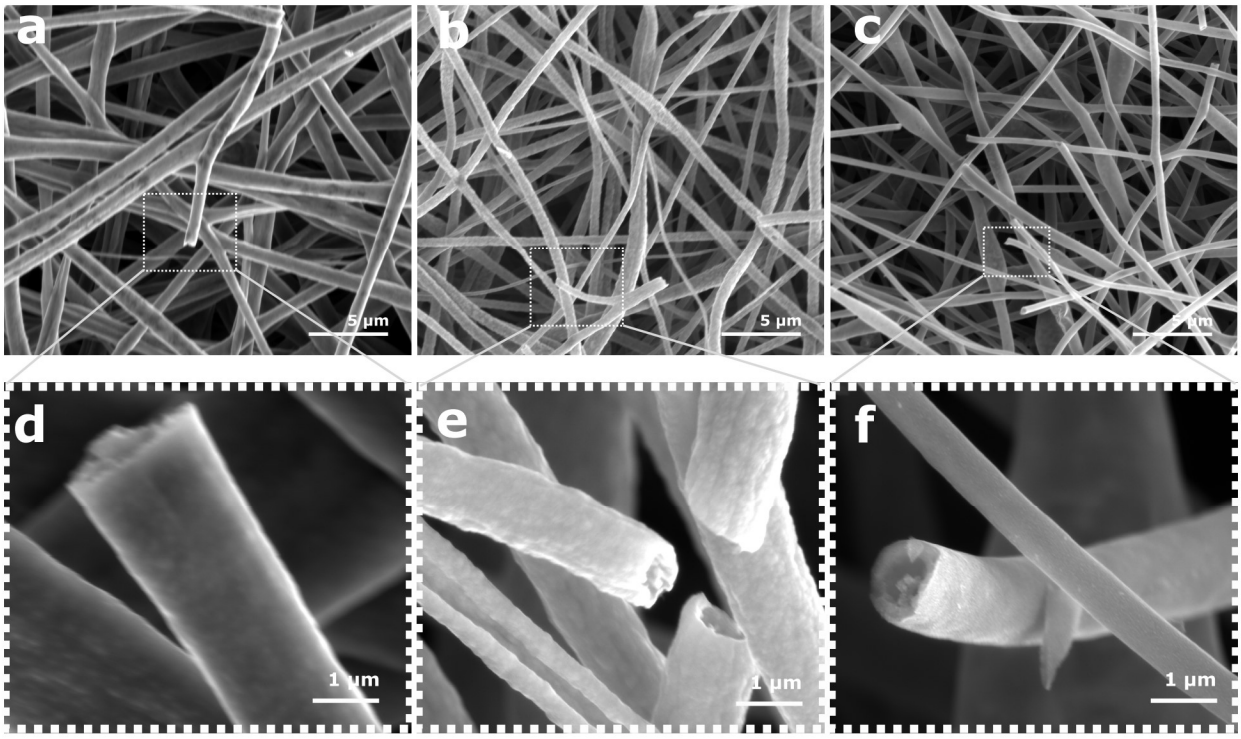

Figure 5.4: *SEM and corresponding high-resolutiuon SEM (bottom) images of the electrospun SiOC fibermats: (a) DDTS-derived SiOC, (b) TPTS-derived SiOC, (c) DTDS-derived SiOC. The images reveal the formation of thick, smooth, and dense fibers for the SiOC samples produced from preceramic Si oligomers with high molecular weight compared to low molecular weights.*

compared to TPTS-SiOC. The hollow fibers with bead-on-string structure of the TPTS-SiOC was attributed to the low molecular weight as well as the concentration and viscosity of the spinning solution[180–182]. High-resolution TEM images of the pyrolyzed fibermats, illustrated in Figure 5.6, suggested the amorphous or featureless structure of the three fiber types. The results of the EDX elemental analyses, also shown in Figure 5.6, confirmed the homogenous distribution of the Si, O, and C elements in the ceramic fibers.

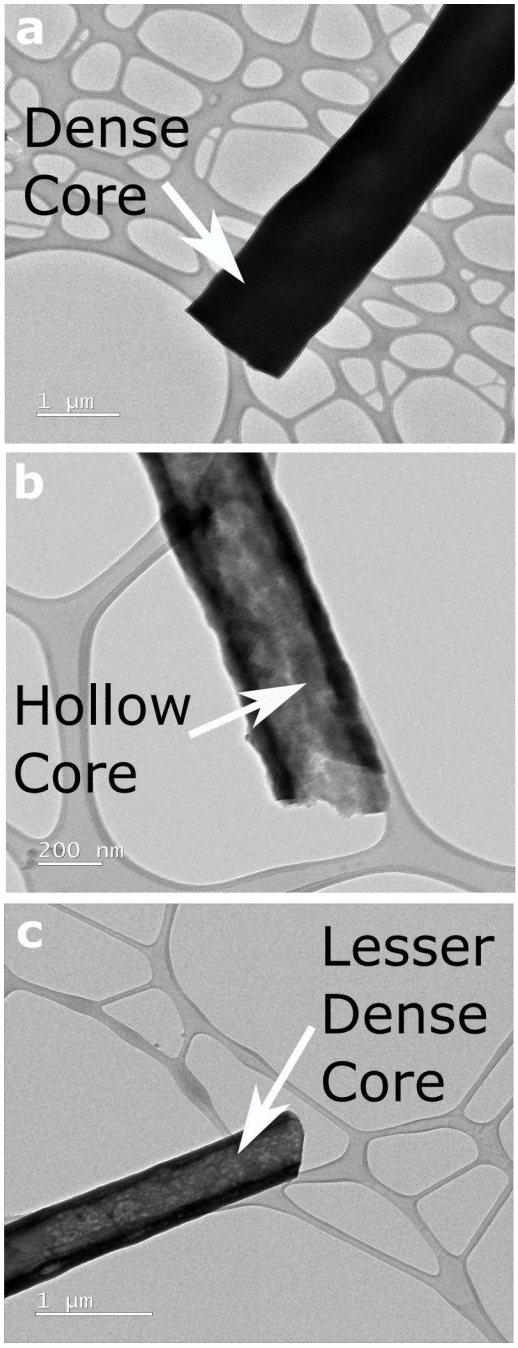

Figure 5.5: *TEM images of the electrospun SiOC fibermats: (a) DDTS-derived SiOC, (b) TPTS-derived SiOC, (c) DTDS-derived SiOC. The images confirm the formation of dense fibers for the SiOC samples produced from preceramic Si oligomers with high molecular weight compared to low molecular weights.*

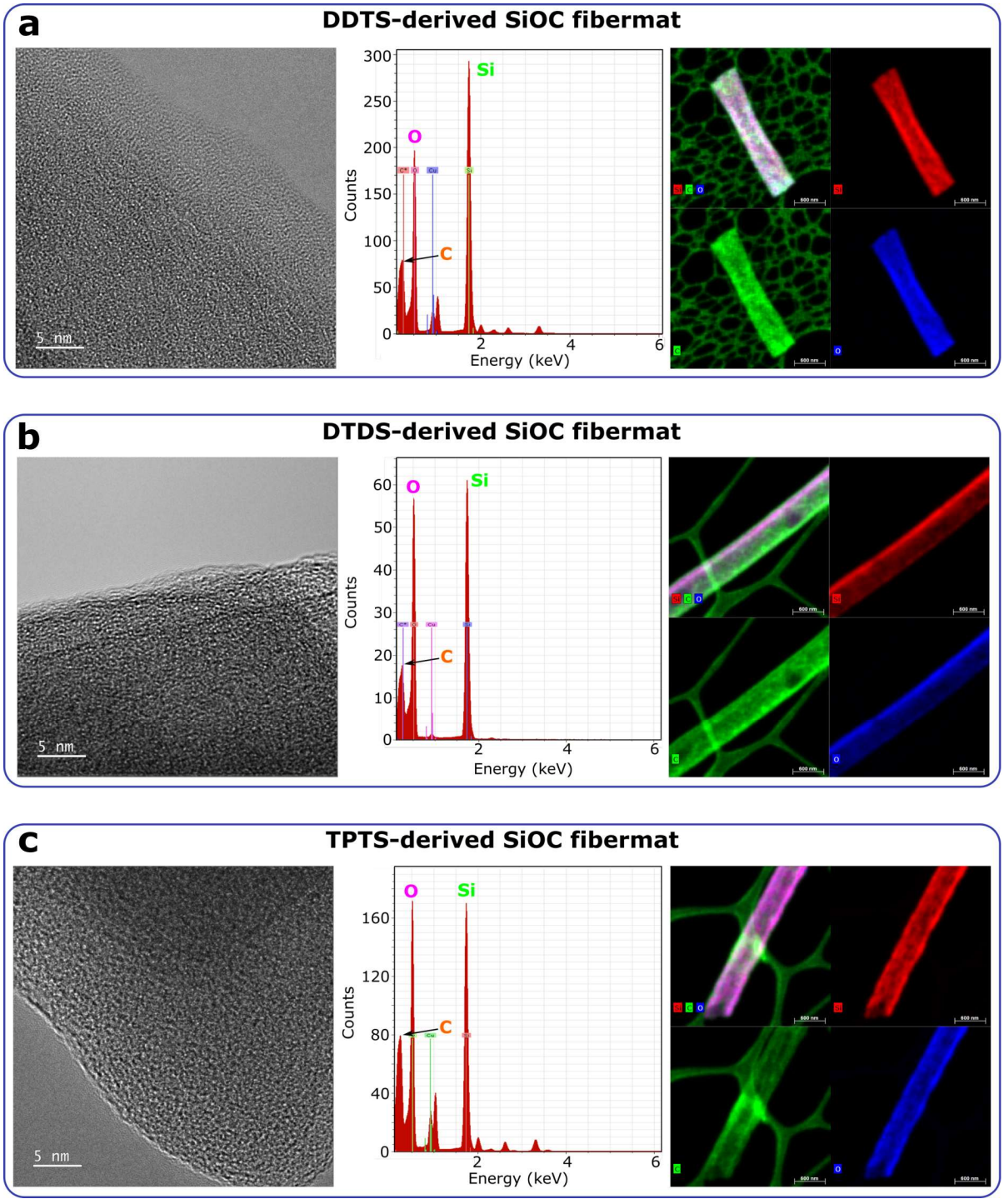

Figure 5.6: *High-res TEM and corresponding EDX mappings of the SiOC fibermats. High-res TEM reveals the amorphous structure of the PDC fibermats. EDX elemental analysis show the presence and homogenous distribution of Si, C, and O in the three polymer-derived SiOC fibermats.*

5.5 Compositional analysis

5.5.1 RAMAN spectroscopy

Raman spectra (Figure 5.7) show the presence of carbon domains which allows to evaluate corresponding microstructures in the ceramic materials. The D and G vibrational bands at 1342 and 1600 cm^{-1} for the DDTS- and DTDS-derived SiOC, suggested the presence of "free carbon" structures i.e., carbon bonded to carbon and not any other elements in the ceramic. The intense D bands suggested the existence of disordered aromatic rings, whereas G bands were associated with the sp^2-hybridized carbon atoms[183]. Additionally, under the fitted curves the T (1424 cm^{-1}) and D" (1490 cm^{-1}) bands indicated the likely presence of disordered sp^2-sp^3 bonds and amorphous carbons in the SiOC fibers, respectively. However, for TPTS-derived SiOC sample, no pronounced D and G peaks were observed as a strong fluorescence background was produced under the visible laser source (HeNe 632.8 nm). The presence of carbon domains in the TPTS-SiOC fibers were later confirmed using XPS analysis.

5.5.2 FTIR spectroscopy

FTIR spectra, plotted in Figure 5.8, shows the characteristic absorption bands of the PVP and polymer-to-ceramic conversion of preceramic Si precursors from the as-spun to pyrolyzed stages. For the PVP, as shown in Figure 5.8(a), as-spun and crosslinked samples exhibited the main peaks at 1660, 1427, 1291, and 570 cm^{-1}, that were assigned to the stretching of C-O, C-H, C-H_2, and N-C=O bonds, respectively[184]. The presence of these peaks in both as-spun and crosslinked PVP fibers suggested no noticeable crosslinking happened during heat treatment at 300 °C, while after pyrolysis at 800 °C these peaks disappeared. DDTS fibers electrospun with PVP (as spinning agent) showed (Figure 5.8b) Si-CH_3 (1260 cm^{-1}), and Si-O-Si (1060 cm^{-1}) stretching bonds in the as-spun fibers indicating the obvious presence of Si precursors in these samples[177;185]. Si-CH=CH_2 (1660 cm^{-1}) are superimposed with the C-O vibration. Reduction of Si-CH_3 and Si-CH=CH_2 peak intensities in the crosslinked

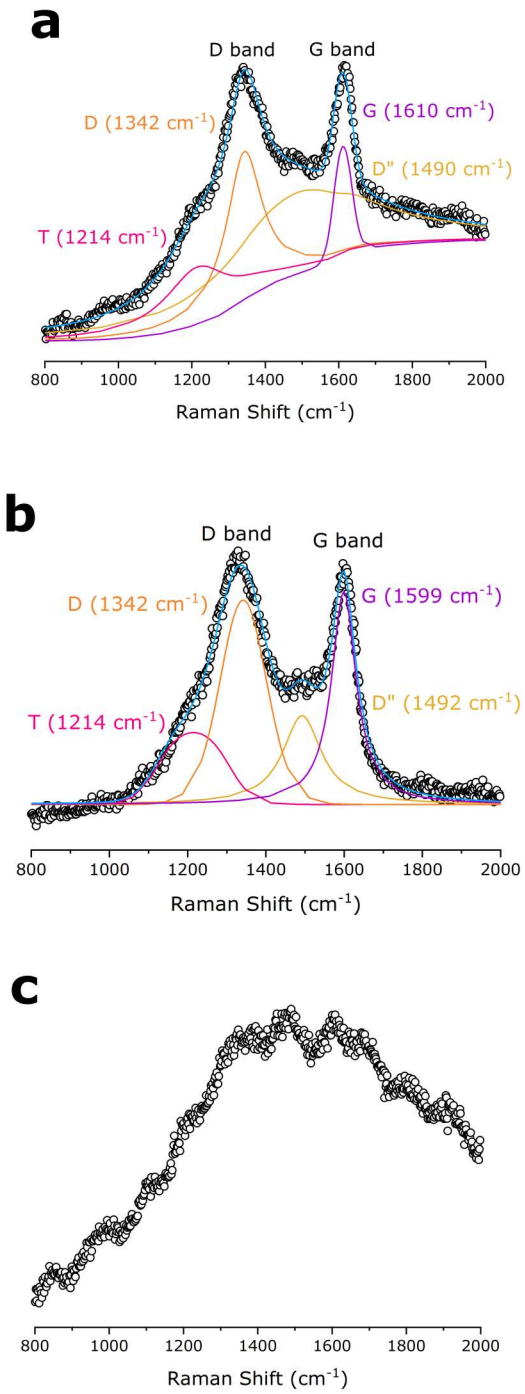

Figure 5.7: *Comparison of Raman spectra for the SiOC samples. (a) DDTS- and (b) DTDS-derived SiOC samples show integrated carbon D and G bonds, whereas (c) TPTS-derived SiOC show strong fluorescence.*

samples suggested crosslinking reactions occurred at approx. 300 °C. After pyrolysis, the two obvious peaks at 1060 and 800 cm^{-1} confirmed the presence of Si-O and Si-C bonds, respectively, in the pyrolyzed SiOC fibers[186]. DTDS- and TPTS-derived SiOC fibers also showed similar characteristic peaks from as-spun to pyrolyzed stages, which are presented in Figure 5.8(c-d). However, Si-O bonds were more intense than Si-C bonds, especially in DTDS-derived SiOC fibers (Figure 5.8c), indicating the presence of more Si-O bonds as compared to Si-C bonds in the ceramic samples. Note the peaks around 3000-3100 cm^{-1} for DDTS, which can be attributed to =C-H stretching of the aromatic phenyl group[187].

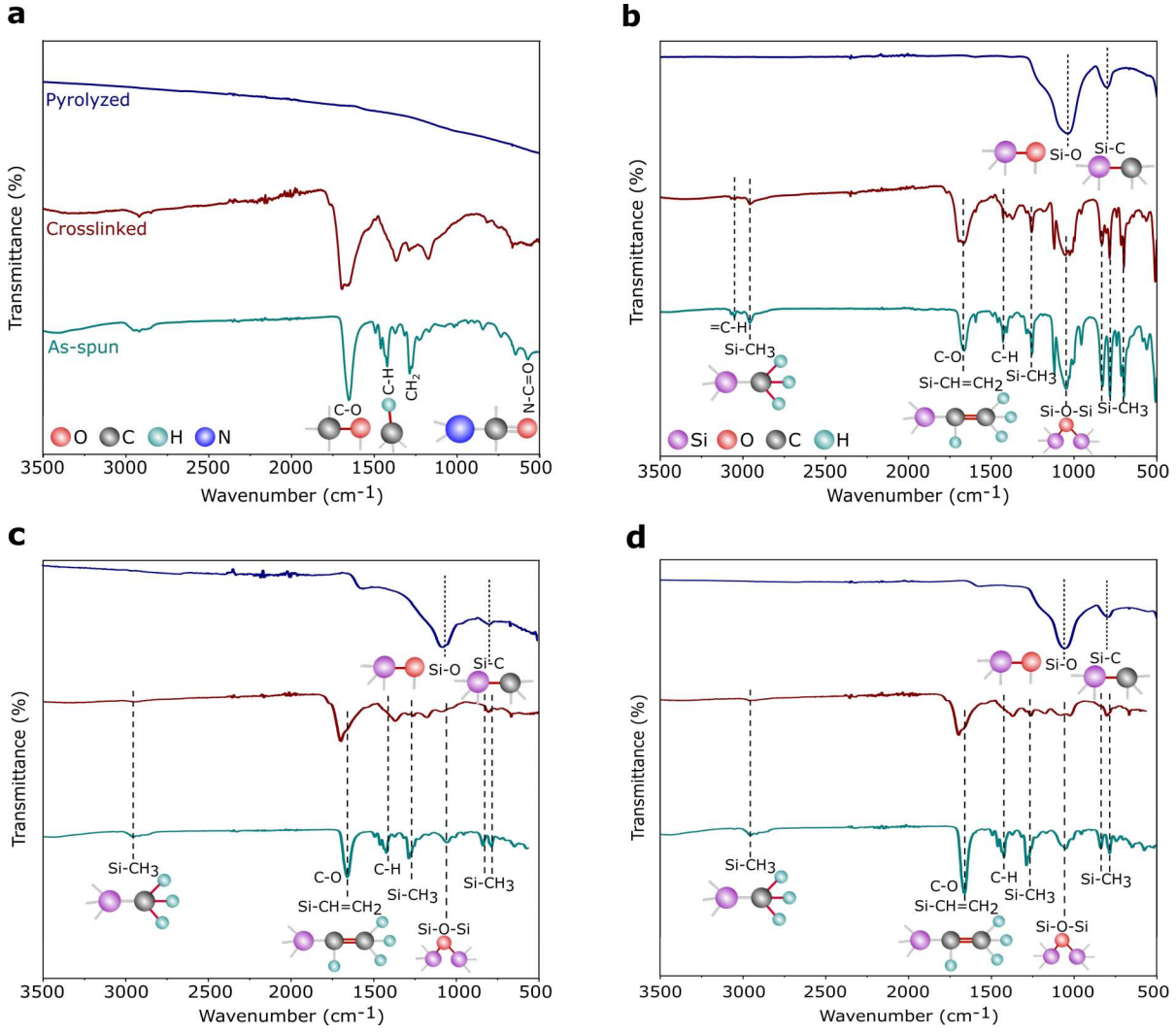

Figure 5.8: *FTIR spectra of electrospun (a) PVP, (b) DDTS-, (c) DTDS-, and (d) TPTS-derived samples show the evolution of chemical bonds from the as-spun to pyrolyzed stages.*

5.5.3 X-ray photoelectron spectroscopy

XPS survey spectra (Figure 5.9) of the electrospun SiOC fibers showed similar Si2p, C1s, and O1s peaks, irrespective of the source of the preceramic polymer. The surface composition of the elements was determined by integrating the area under the respective peaks and presented in Table 5.1. As expected, pyrolyzed PVP fibers mostly showed the presence of carbon (93.06 at.%) after heat treatment. DDTS- and TPTS-derived ceramic fibers shows increased level of oxygen in the pyrolyzed samples indicating the inclusion of oxygen during crosslinking of the fibers. All specimens showed a significant amount of carbon, mainly free carbon, also proposed by Raman analysis. However, pyrolyzed samples presented a little amount of nitrogen, which was suspected to have come from PVP. High-resolution XPS spectra, plotted in Figure 5.10, shows the bonding of the pyrolyzed SiOC samples derived from various siloxane precursors. Curve fittings were done to the Si2p, C1s, and O1s peaks. The spectra under Si2p band indicated the presence of $SiCO_3$ (102.1 eV) and SiO4 (103.5 eV) peaks[188]. Low intensity of $SiCO_3$ compared to SiO_4 for pyrolyzed-DDTS ceramic fibers were due to the low carbon content in the elemental composition. In addition, C-Si (284.0 eV), C-C (284.9 eV), and C=O (287.1 eV) were observed in C1s band[177]. The higher amount of carbon in the pyrolyzed-DTDS and pyrolyzed-TPTS fibers lead to higher intensity of C-C and C-Si peaks. The intense C-C peaks also pointed to increased possibility of free carbon phase in the ceramic fibers. O1s band were fitted with 3 peaks at 532.4, 532.9, and 534.4 eV corresponding to SiO_2, O-Si, and C-O, respectively.

5.5.4 NMR spectroscopy

The initial composition of the electrospinning solution was investigated by liquid state NMR. ^{29}Si spectra (Figure 5.11a) show for all systems a signal around –3 ppm corresponding to $ViMe_2SiO$ environments. In addition, signals are observed at -46.8 ppm and -34.0 ppm in DDTS and TPTS based solutions that can respectively be assigned to Ph_2SiO_2 and $ViMeSiO_2$ groups. This assignment was confirmed by 2D experiments. For example, ^{1}H-^{29}Si HMBC map of DDTS solution (Figure 5.12a) shows that the ^{29}Si signal at -47 ppm

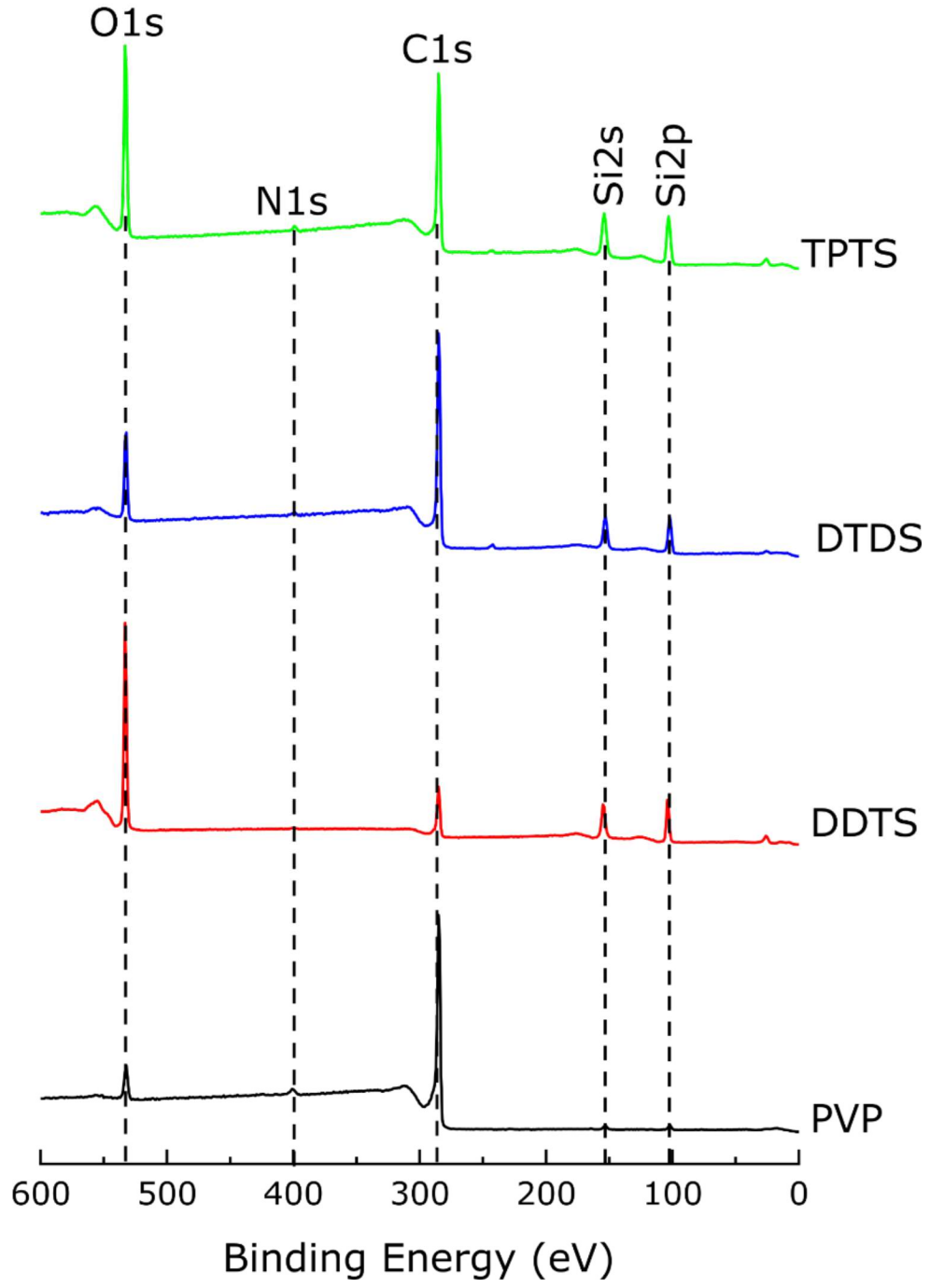

Figure 5.9: *XPS spectra of the various samples pyrolyzed at 800 °C.*

shows cross-peaks with ^{1}H phenyl signals between 7.5 and 8 ppm while the ^{29}Si signal at -34 ppm shows cross-peaks with ^{1}H vinyl signals between 6 and 5.5 ppm. The evolution of the various preceramic siloxane precursor structures during heat treatment and the resulting

Table 5.1: *Elemental composition (at.%) of SiOC ceramic fibers by XPS*

Pyrolyzed samples	C	O	Si	N
Carbonized PVP	93.06	4.84	-	2.10
DDTS-derived SiOC	32.35	37.58	29.70	0.37
DTDS-derived SiOC	73.80	9.42	16.09	0.68
TPTS-derived SiOC	58.00	19.28	21.74	0.98

SiOC samples were also investigated using solid-state NMR. Spectra were recorded on bulk powders instead of fibers to improve the signal/noise ratio.

Figure 5.11(b) shows ^{29}Si MAS NMR spectra for crosslinked (at 300 °C) polymers and compares the key features of the DDTS, DTDS, and TPTS polymers. Appearance of -CHx-Me2SiO- (10 ppm) in the polymers indicated effective crosslinking of the vinyl groups occurred in presence of DCP[189]. On the other hand, a signal appeared at -21 ppm which was characteristic of Me_2SiO_2 units in polydimethylsiloxane (PDMS) chains[190;191]. This would suggest that part of the Si-CH=CH_2 groups were replaced by Si-O-Si bonds during heat-treatment as confirmed by the total disappearance of $ViMeSiO_2$ units at -3 ppm in DTDS and TPTS cross-linked systems. Moreover, in the case of TPTS, $ViMeSiO_2$ units observed at -34 ppm in the initial solution disappeared in the cross-linked system while new signals were present around -70 ppm, a chemical shift range characteristic of $MeSiO_3$ environments. Here again, this suggested the replacement of Si-CH=CH2 groups by Si-O-Si bonds. In the case of DDTS, Me_2SiO_2 units were observed but $ViMeSiO_2$ were also present in small quantity in accordance with IR experiments showing remaining vinyl groups after crosslinking (Figure 5.8b). The signal corresponding to Ph_2SiO_2 units (-48 ppm) was still intense after crosslinking suggesting that Si-Ph bonds were preserved. The ^{29}Si MAS spectra of the samples pyrolyzed at 800 °C showed SiO_4 bonds (-110.0 ppm) (Figure 5.10d), while no Si-C bonds were found[192]. This might be due to the fact mostly free C phase had formed during pyrolysis, and very low Si-C bonds were present in the ceramic samples[177].

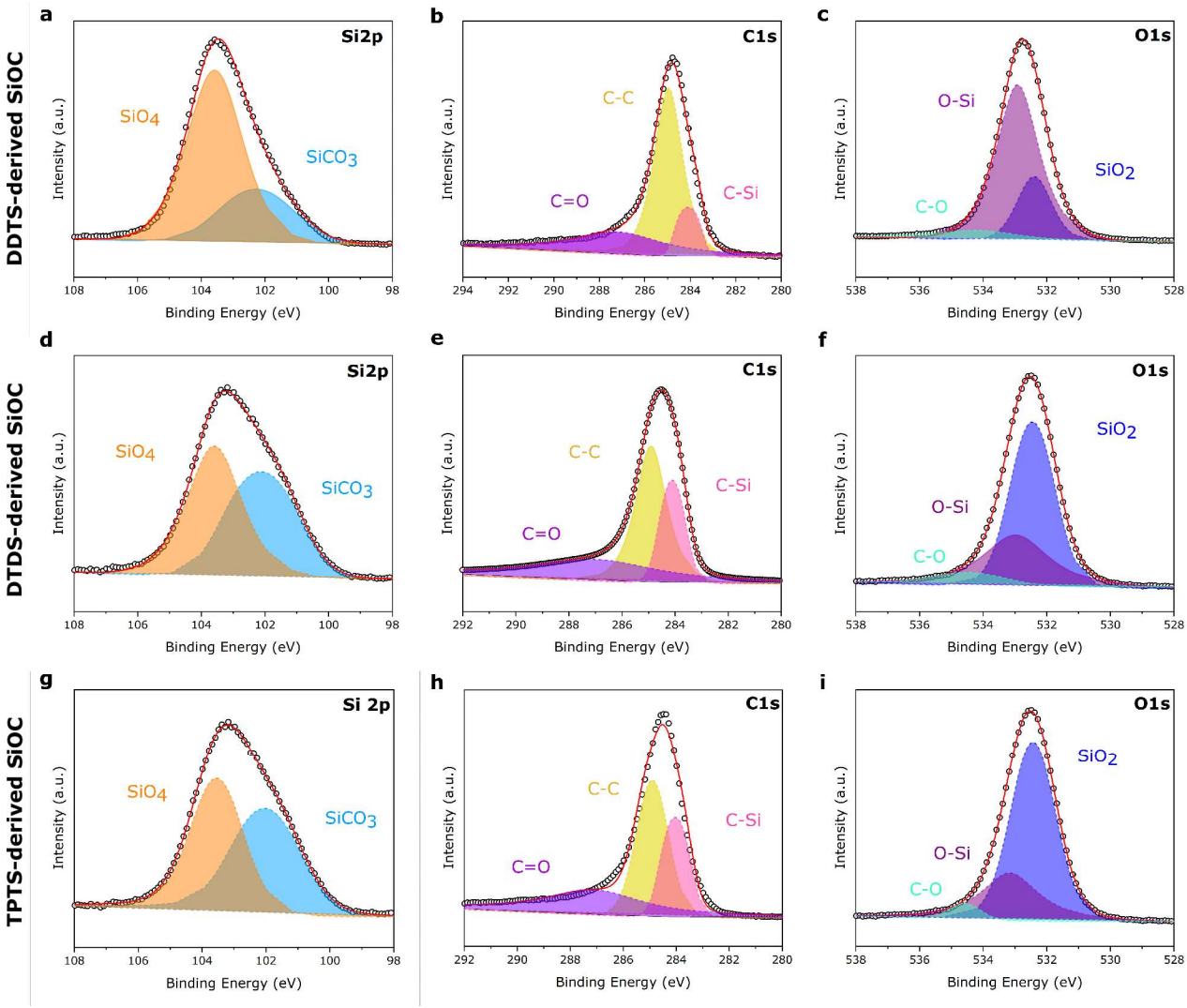

Figure 5.10: *High-res XPS spectra of the three preceramic polymer-derived SiOC fiber samples. (a-c) DDTS-derived SiOC; (d-f) DTDS-derived SiOC; (g-i) TPTS-derived SiOC.*

Nevertheless, high-res XPS of the SiOC fibers indicated the presence of Si-C and C-C bonds in the ceramic fibers.

^{13}C cross polarization (CP) MAS NMR spectra in Figure 5.11(c) show strong peaks of Si-CHx indicating the crosslinking of the Si precursor polymers. In the DTDS polymer, sp^2 carbons were observed around 130 ppm that corresponded mainly to the phenyl groups. Indeed, from ^{1}H-^{13}C HSQC map of DDTS solution (Figure 5.11b) cross-peaks with ^{1}H phenyl signals (between 7.5 and 8 ppm) were observed for carbon signals at 127.6 , 129.7 and 134.4 ppm, while the cross-peaks with ^{1}H vinyl signals (between 6 and 5.5 ppm) were observed

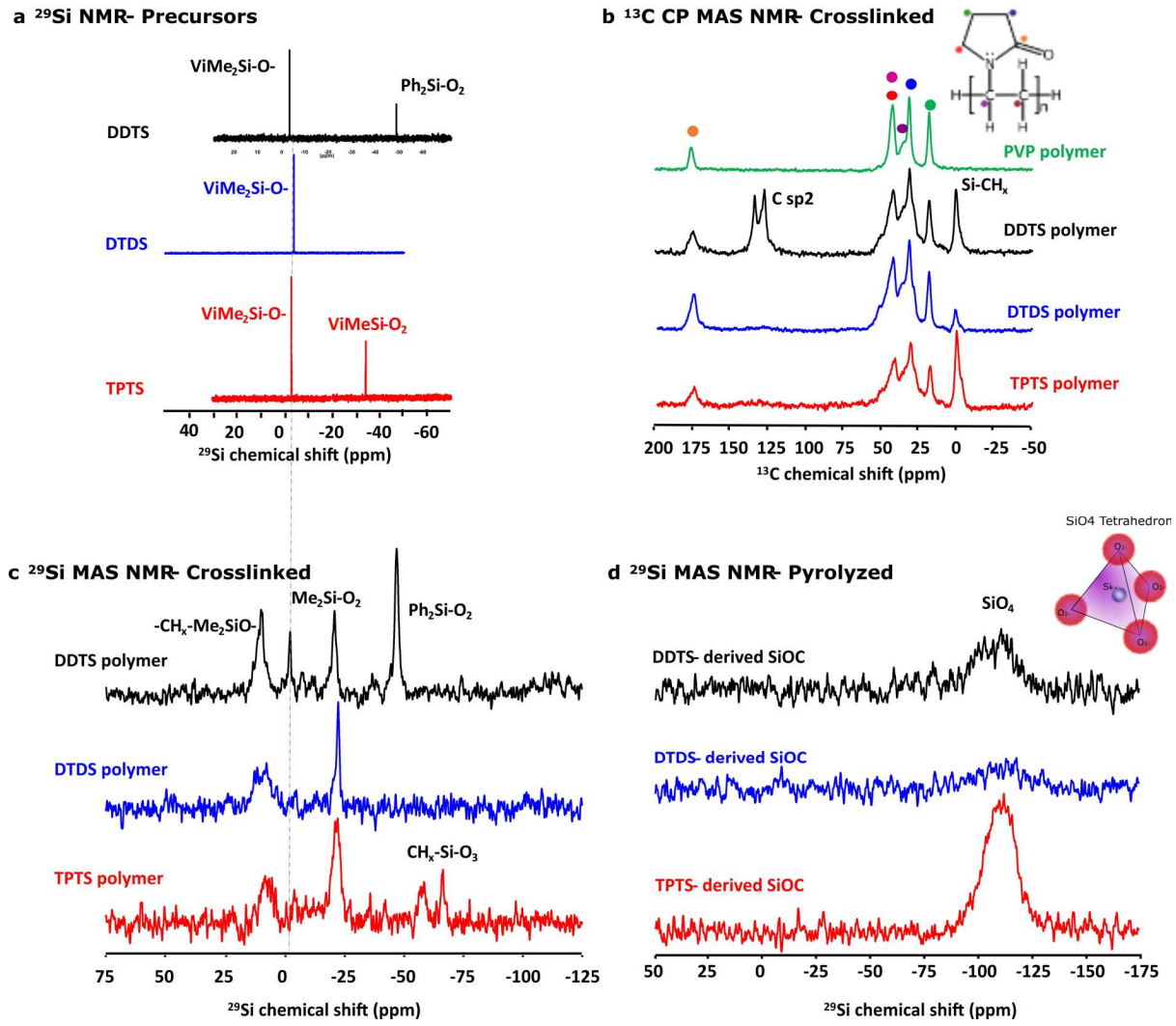

Figure 5.11: *NMR spectra of precursors, crosslinked and pyrolyzed samples. (a) ^{29}Si liquid state NMR of the electrospinning solution, (b) comparison of solid state ^{29}Si MAS NMR spectra of crosslinked polymers of various preceramic Si precursors, (c) ^{13}C CP MAS NMR spectra of crosslinked (at 300 °C) polymers in comparison with PVP, (d) comparison of ^{29}Si MAS NMR spectra of pyrolyzed (at 800 °C) ceramic powders.*

with carbon signals at 132.1 and 139.0 ppm. The absence of a clear ^{13}C peak at 139 ppm in the DTDS cross-linked sample suggested that the proportion of vinyl groups was small compared to phenyl groups. No evidence of crosslinking behavior between PVP molecules and siloxane was observed in all the crosslinked samples when compared with PVP polymer. ^{13}C CP MAS NMR spectrum of the TPTS-derived SiOC confirmed the presence of typical free carbon as shown in Figure 5.13. ^{13}C spectra of the remaining SiOC samples were not

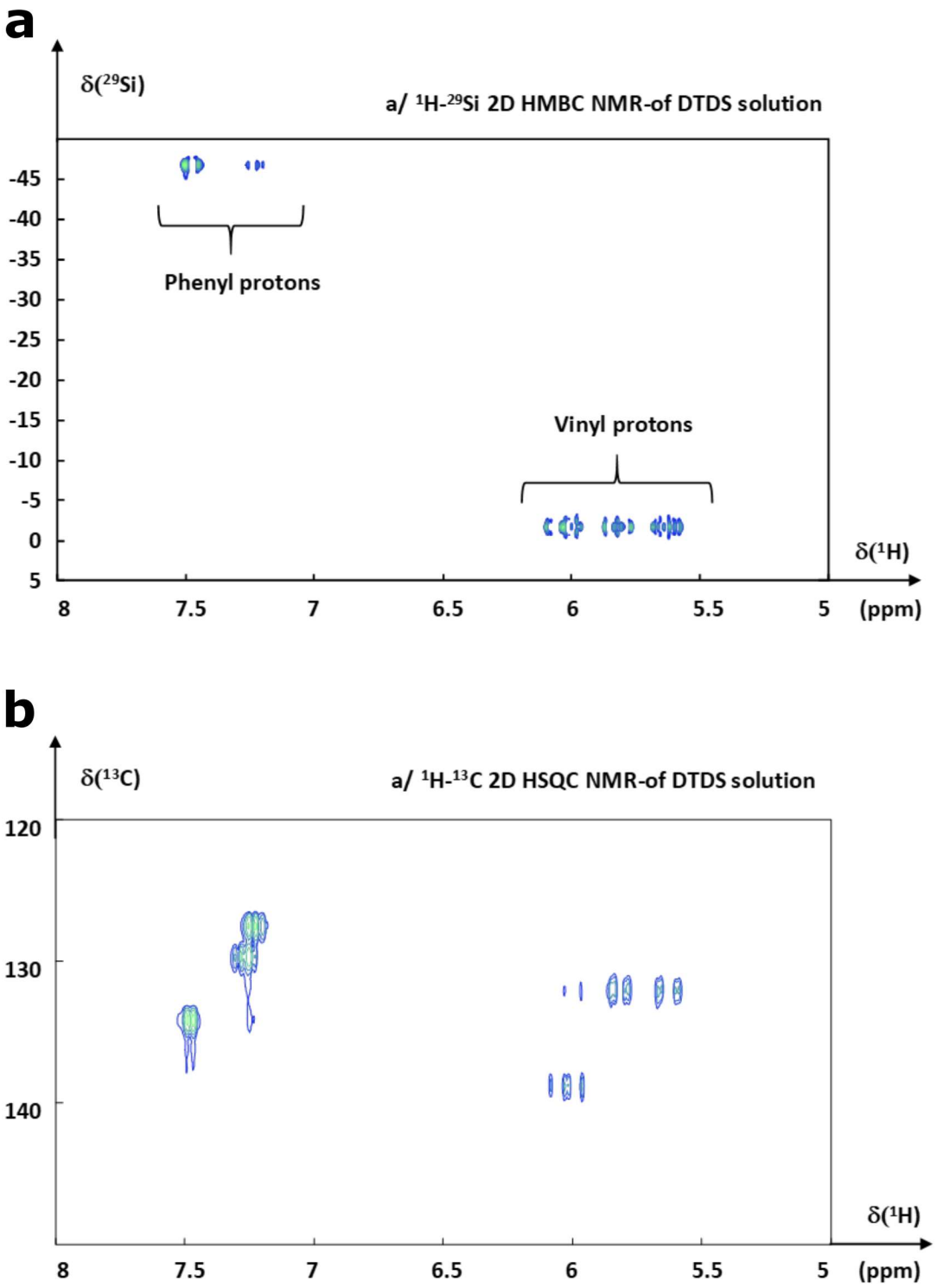

Figure 5.12: *(a) ^{1}H-^{29}SiC and (b) ^{1}H-^{13}C 2D NMR spectra of the DTDS electrospinning solution.*

acquired as it was obvious from the other characterization techniques that all the systems were full of graphite.

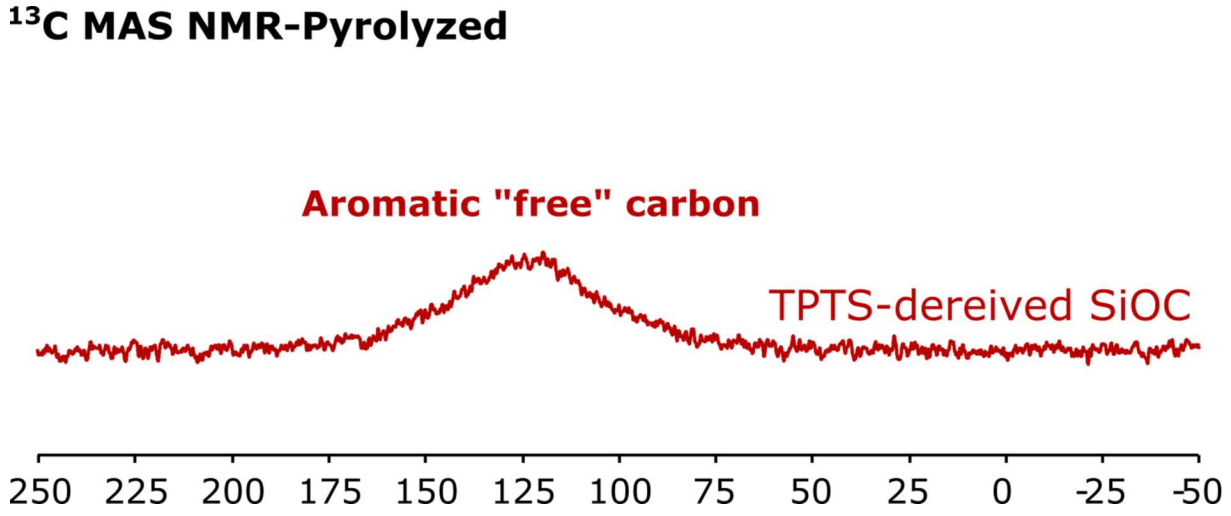

Figure 5.13: ^{13}C *CP MAS NMR spectrum of pyrolyzed (at 800 °C) TPTS-derived SiOC ceramic powders indicates the presence of typical "free carbons".*

5.6 Conclusions

In this study, a method is presented to fabricate scalable, cost-effective, freestanding electrodes from SiOC using three unique siloxane precursors. The electron microscopy of the SiOC fibers featured rigid surface structures and small diameters (0.2-3 µm). Raman, XPS, FTIR, and NMR characterization techniques outlined the polymer to ceramic conversion stages. Further experiment on the properties of the as-prepared SiOC fibers can be found in the following chapter.

Chapter 6

Properties of self-supporting SiOC ceramic fibermat[1]

6.1 Preview

The as-fabricated precursor-derived SiOC fibermats, mentioned in Chapter 5, are used as free-standing, binder-free electrodes in LIBs. Free carbon phase improves the electronic conductivity and provides major sites for Li^+ ion storage, whereas Si-O-C structure contribute to high efficiency. The self-standing electrodes in lithium-ion battery half-cells delivers a charge capacity of 866 mAh $g^{-1}_{electrode}$ with a high initial coulombic efficiency of 72%. As supercapacitor electrode, SiOC fibers maintain 100% capacitance over 5000 cycles at a current density of 3 A g^{-1}.

6.2 Introduction

Despite the exponential rise in research activity on design and development of micro-/nano-structured electrode materials for electrochemical energy storage devices[109;193–195], graphite

[1]Reprinted from Mujib, S. B., Ribot, F., Gervais, C., and Singh, G. (2021). Self-supporting carbon-rich SiOC ceramic electrodes for lithium-ion batteries and aqueous supercapacitors. *RSC advances*, 11(56), 35440-35454.

or carbon-coated metal foil remain the electrode of choice for most capacitors and Li-ion battery (LIB) technologies. Materials with higher charge storage than traditional carbons such as silicon [almost 10X lithium (Li) storage capacity (4.2 Ah g^{-1})] emerged as potential replacement for graphite owing to silicon's large abundance in the earth crust, low toxicity, and well-established manufacturing technology for its large scale production[196–198]. However, drastic volume variation and pulverization during charge/discharge, excessive formation of solid electrolyte interface (SEI), and stress-induced cracks in Si electrode has rendered bulk silicon unusable as an electrode for LIBs[197;199].

To circumvent the issues associated with silicon electrodes, silicon oxycarbide (SiOC) derived from pyrolysis of ceramic precursor polymers has renewed attention in recent years from electrochemical storage point of view[188;200–208]. Potential of polymer-derived ceramic (PDC) (e. g; SiOC, SiCN) materials in energy storage, initially proposed by Dahn et al. in 1990s, largely depends on the chemical structures of the material[209;210]. SiOC is an amorphous ceramic mainly consists of a Si-O-C glass phase with a free carbon region, where the mixed bonds of Si with O and C enable high Li storage[211;212]. According to Graczyk-Zajac et al., mixed bonds in SiOC allows more disordered carbon phase for higher Li capacity (325 mAh g^{-1}) as well as reversible storage sites at the interface of the carbon phase and amorphous network[213]. Kasper et al. showed that the electrical conductivity of SiOC samples improved (0.07 to 2.2 S m^{-1}) with the increasing amount of free carbon phase, in addition to enabling more active sites for Li[214]. The edges of the free carbon phase and the interstitial spaces are major electrochemically active sites for Li ions, whereas micro-/nano-voids and amorphous Si-O-C network contribute to minor Li storage[201;215;216]. Lee et al. reported that controlling the nanovoids in the Si-O-C domain derived from PSS-Octakis(dimethylsilyloxy)silsesquioxane (POSS) provided efficient ion pathway and withstood structural degradation by buffering during lithiation/delithiation[208]. As a result, the authors were able to achieve a capacity of 412 mAh g^{-1} at a high current density of 3600 mA g^{-1}. Furthermore, pyrolysis parameters are always crucial in controlling the microstructure (e. g; free/disordered carbon phase and nanovoids) and thus maintaining the electrochemical properties of SiOC. For example, pyrolysis temperature above 900 °C results in lower capac-

ity and unstable cycling behavior of the SiOC ceramics compared to lower temperature[205;217]. With increasing temperature disordered carbon phase arranges into ordered structure and amorphous Si-O-C phase decomposes to electrochemically inactive SiC crystals. In addition, metal foil-based electrode, conventionally prepared using a doctor blade, carries the inactive weight of polymeric binders, conducting agents (usually carbon black), and the foil itself, which do not contribute towards electrode capacity[188].

Amorphous Si-O-C phase provides chemical stability and host sites for Li storage, and free carbon phase contributes to conductive network as well as the high Li capacity of the fibermat. As a result, as-prepared SiOC electrodes deliver specific capacity as high as 866 mAh $g^{-1}_{electrode}$ (considering total weight of the electrode) with high first cycle coulombic efficiency of 72% in LIBs. Specific capacity of 800 mAh g^{-1} at a current density of 50 mA g^{-1} is achieved with a 100% capacity retention after 50 cycles for a particular SiOC electrode. Further, as supercapacitor electrode SiOC fibers have delivered a high gravimetric capacitance of 55 F g^{-1} at 100 mV s^{-1} and maintained 100% capacitance over 5000 cycles at 3 A g^{-1}.

6.3 Experimental

6.3.1 Electrode preparation and electrochemical measurement

Ceramic fibermats were tested electrochemically both as organic electrolyte-based lithium-ion batteries (LIBs) and aqueous supercapacitors electrodes. Electrospun SiOC ceramic fibermats were used as freestanding electrodes in LIBs half-cells. A disk electrode was punched out from the pyrolyzed fibermat with diameter of about 6.35 mm (1/4 inch), which was used as the working electrode. A glass fiber membrane (19 mm, t 25 µm) (GE, USA) as separator, pure Li metal (14.3 mm, t 75 µm) (Alfa Aesar, USA) as the counter electrode, and approximately 6 drops of 1 M lithium hexafluorophosphate (LiPF6) in (1:1 v/v) dimethyl carbonate (DMC):ethylene carbonate (EC) (Sigma Aldrich, USA) as the electrolyte were used. The cells were assembled in LIR 2032 coin cells in a glove box, and the assembled cells

were tested using a multichannel BT2000 Arbin test system (Texas, USA) between 10 mV to 2.5 V vs. Li/Li^+. The cells were subjected to symmetric cycling at current densities of 50, 100, 200, 400, 800, 400, 200, 100, 50 mA g^{-1} for 5 cycles each.

For supercapacitor testing, a three-electrode setup was used. Ceramic fibermats (as an active material) were mixed with 10 wt.% carbon black (as a conducting agent) (Alfa Aesar, Massachusetts, USA) and 5 wt.% polyvinylidene fluoride (PVDF) (as a binder) (Sigma Aldrich, Missouri, USA) thoroughly; approximately 4-6 drops of N-methyl 2 pyrrolidone (NMP) (Alfa Aesar, Massachusetts, USA) was also added to form a slurry of uniform consistency. The slurry was then pasted on stainless steel (SS) mesh (1x1 cm^2) using a flat paint brush, followed by drying at 80 °C overnight in an oven. The ceramic coated SS was then used as working electrode in the three-electrode setup, where Pt wire and Ag/AgCl were used as the counter and reference electrode, respectively. 1M NaCl was used as an electrolyte. A CHI 660 electrochemical workstation (CH Instruments, Inc., Texas, USA) was used to perform cyclic voltammetry (CV) and galvanostatic charge-discharge (GCD) of the electrodes. CV and GCD were performed in the potential window of 0 to 1 V at various scan rates and current densities, respectively. Electrochemical impedance spectroscopy (EIS) was also carried out from 0.01 Hz to 100 kHz at an amplitude of 5mV. For CV and GCD, the specific capacitance values were calculated using equations 6.1 and 6.2, respectively[161].

$$\begin{aligned} C &= -\frac{1}{m.v(V_f - V_i)} \\ &= -\frac{\Delta G_r}{z.F} \end{aligned} \tag{6.1}$$

$$C = -\frac{I.\Delta t}{m.\Delta V} \tag{6.2}$$

where, C is the specific capacitance, m is the active mass of electrode, v is the scan rate, V_i and V_f are the initial and final voltage, I(V) is response current density, I is charge/discharge current, and ΔV is the potential window.

6.4 Electrochemical performance

The electrochemical energy storage capability of the precursor derived SiOC fibers were analyzed in Li half-cells. The as-prepared ceramic fibermats were used as electrodes. Figure 6.1(a-c) shows the potential vs capacity plots for various SiOC fiber electrodes. A closer look at the charge-discharge profiles of the samples at a current density of 50 mA g^{-1} showed that first cycle had experienced irreversible capacity decay. Among the SiOC electrodes, the DDTS-derived SiOC delivered initial discharge capacity of 1188 and charge capacities of 866 mAh g^{-1}, corresponding to a high coulombic efficiency of over 72%. DTDS-derived SiOC electrode delivered 1332 and 800 mAh g^{-1}, respectively for discharge and charge capacities in the first cycle with 59% efficiency. TPTS-derived SiOC provided 1150 and 636 mAh g^{-1} for discharge and charge capacities, respectively, with 52% coulombic efficiency. DDTS- and DTDS-SiOC electrodes showed stable response with coulombic efficiency of 100% in the second and third cycles, whereas TPTS-SiOC displayed poor reversibility with only 83% efficiency.

Differential capacity plots, presented in Figure 6.2, showed two distinct regions for the SiOC electrodes: a sharp peak around 0.1 V, which corresponded to the Li insertion into the carbons; and a broad region in between 0.2 to 0.6 V, that was related to Li and Si-O-C phase[32]. Figure 6.2(a-c) shows the differential capacity curves of the SiOC electrodes for the initial 3 cycles. The sharp cathodic peak at 0.005 V and the broad anodic peak can be attributed to the lithiation and delithiation of Li^+ ions in the amorphous SiOC structure[166;204]. The cathodic peaks in the range of 0.05 to 0.16 V can be attributed to the irreversible reaction in hard carbon present in the SiOC structure[30;204]. However, cathodic peaks due to formation of SEI (typically at 0.5V) are less pronounced in the dQ/dV plots.

To show the consistent performance of the cells, three Li half-cells of each type were assembled and tested and the performance of all the cells are presented in Figure 6.3. When tested for cycling stability TPTS-SiOC electrode showed poor performance and the charge capacity dropped sharply to 100 mAh g^{-1} after 50 cycles at 50 mA g^{-1}. For DDTS- and DTDS-SiOC electrodes, the capacities after 50 cycles were 580 and 800 mAh g^{-1}, showing

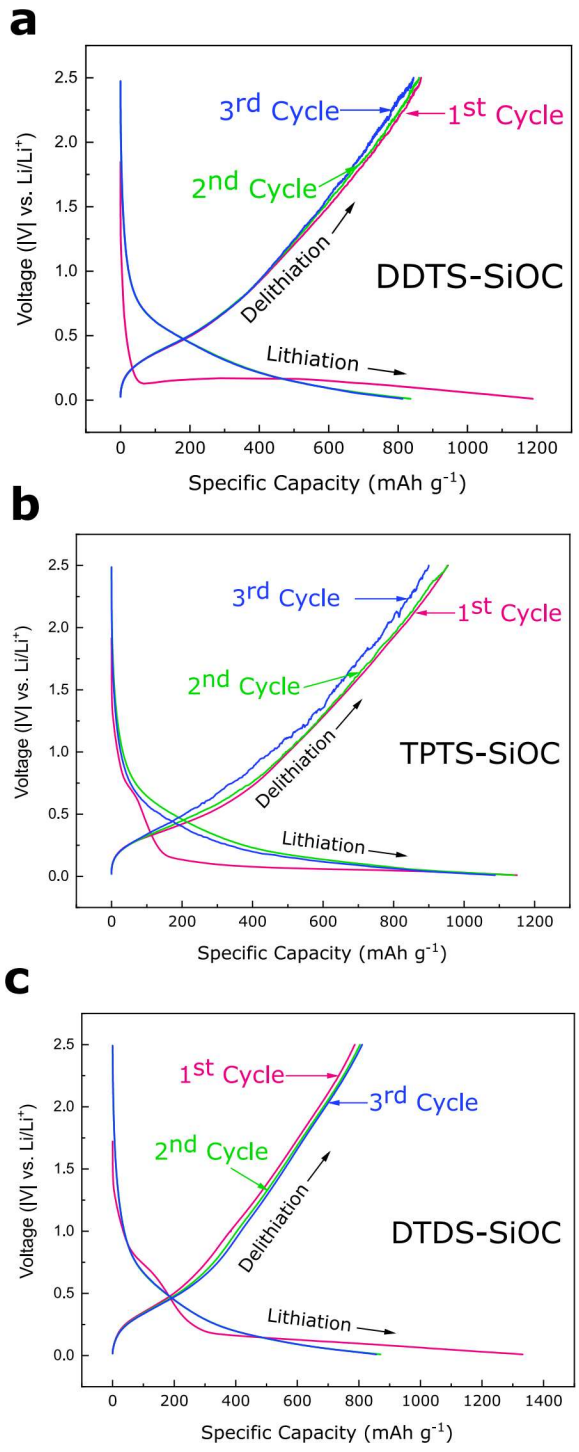

Figure 6.1: *Charge-storage performances of the various precursor-derived SiOC freestanding fibermats in the Li half-cells. (a-c) Voltage profile of the SiOC electrodes show the charge-discharge profiles for the first three cycles.*

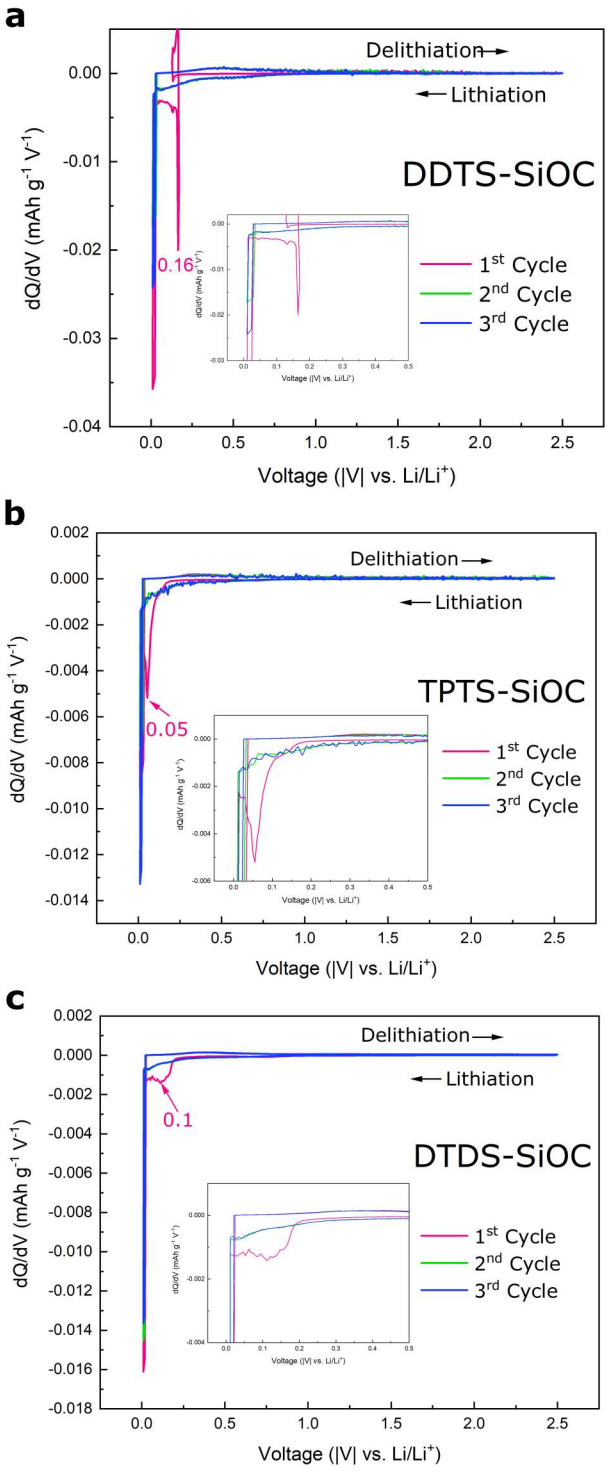

Figure 6.2: *(a-c) Differential capacity curves of various SiOC electrodes show characteristic regions of reversible reactions between Li and SiOC.*

100% capacity retention for the DTDS-derived SiOC fiber electrode. The distinct fiber morphology and the "free C" content in the DTDS-SiOC particles provided additional Li-ion storing sights and improved the electrochemical properties of SiOC fibers[202]. The rate capability performance comparison of the various SiOC electrodes is presented in Figure 6.4. DTDS-SiOC delivered a high capacity of 450 mAh g^{-1} at a high current density of 800 mA g^{-1}. However, thin diameter and hollow structure of the TPTS-SiOC fibers might have been destroyed during Li-ion insertion/extraction process, which resulted in poor cycleability and rate capability[203].

The SEM and TEM images of the SiOC electrodes after cycling in LIBs are shown in Figure 6.5, where the broken fibers of the TPTS-SiOC can be seen post-cycling. Whereas poor rate capability performance of the DDTS-SiOC can be attributed to the low C content as well as dense structure of the fibers which limits the ion diffusion.

The electrochemical storage capabilities of SiOC fibers in supercapacitors were also investigated using three electrode system and 1M H_2SO_4 as electrolyte. CV plots obtained for TPTS-derived SiOC electrode at various scan rates of 2 to 500 mV s^{-1} from 0 to 1 V are shown in Figure 6.6(a). The almost rectangular shape of the voltammogram profiles indicated mostly the electrochemical double layer capacitive behavior (Type A) of the SiOC electrode during charge storage[205]. However, at a low scan rate of 2 mV s^{-1}, a broad redox peak was observed for TPTS-SiOC electrode in between 0.2 and 0.4V (Figure 6.6(b)). The charge storage mechanism at lower scan rate can be contributed to the combination of double-layer capacitance of C in SiOC and pseudocapacitance from Si-O and Si-Si components. The quasi-rectangular shape of the CV plot retained even at higher scan rate of 500 mV s^{-1}, indicating higher ionic diffusivity and charge transfer of the TPTS-SiOC electrode. As a result, the electrode delivered high specific capacitances of 78, 69, 55, 47, and 38 F g^{-1} at the scan rates of 2, 10, 100, 200, and 500 mV s^{-1}. The areal capacitance of the TPTS-SiOC electrode was also calculated and a high capacitance of 474 mF cm^{-2} was achieved at 2 mV s^{-1}.

The cyclic voltammograms of DTDS- and DDTS-derived SiOC supercapacitor electrodes are presented in Figure 6.7. DTDS-SiOC delivered 107 F g^{-1} at a scan rate of 2 mV s^{-1} and

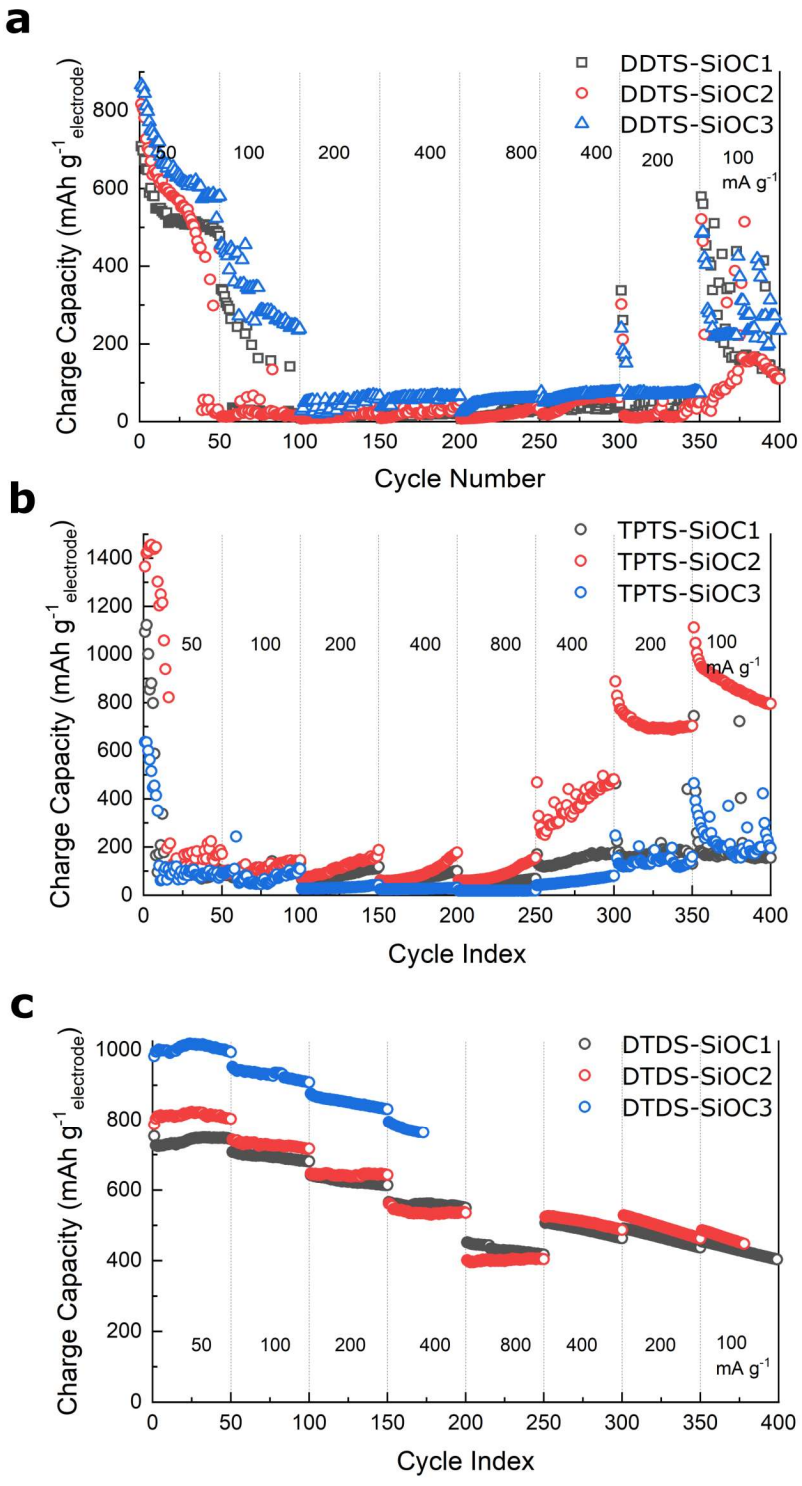

Figure 6.3: *(a-c) Rate capability performance of three SiOC electrodes of each type shows consistent performance.*

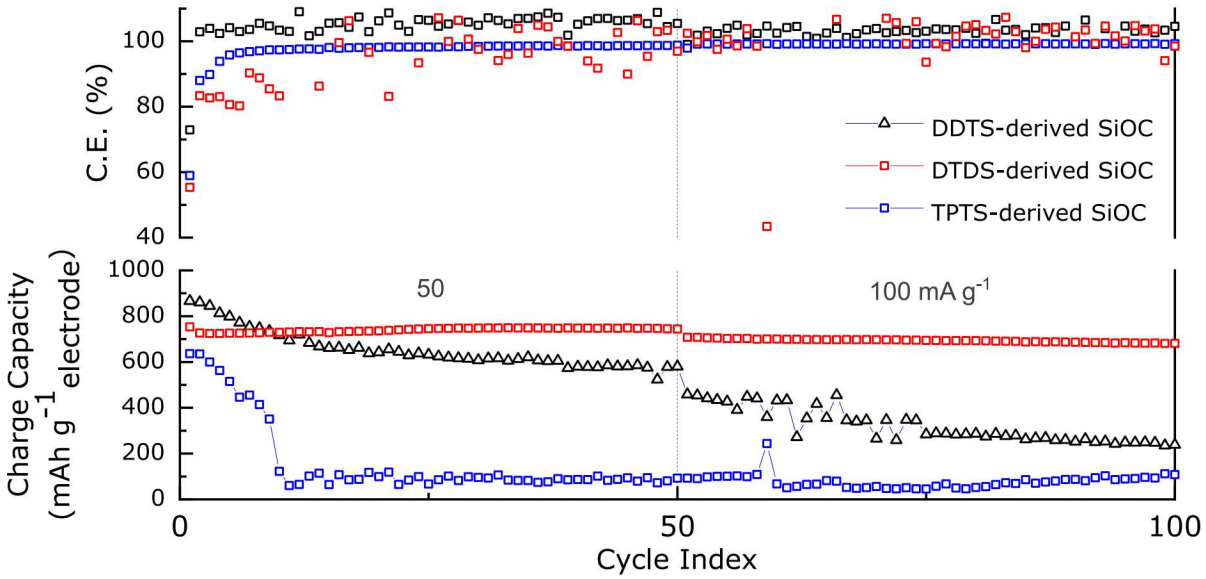

Figure 6.4: *Comparison of cycling stability of the samples for 100 cycles. DTDS-SiOC shows stable performance delivering 680 mAh g^{-1} at 100 mA g^{-1}, whereas DDTS-SiOC and TPTS-SiOC deliver 240 and 110 mAh g^{-1}, respectively after 100 cycles.*

decreased to 31 F g^{-1} at 100 mV s^{-1}, where DDTS-SiOC delivered 25 and 3 F g^{-1} at 2 and 100 mV s^{-1}, respectively. The highest performance of TPTS-SiOC among the three SiOC electrodes was correlated to the lowest diameter and hollow core of the fibers, contributing to a higher electrochemically active area for double-layer capacitor. The BET analysis and avg. pore diameter of the SiOC samples are presented in Table 6.1 and Figure 6.11. As-anticipated the TPTS-SiOC had a high specific surface area of 235 m^2 g^{-1}. In addition, the presence of "free C" contributed to the enhanced electronic conductivity. Figure 6.8 demonstrates the charge/discharge profiles of the best performing TPTS-SiOC electrodes at various current densities from 0 to 1 V. The quasi-triangular shape of the GCD curves without any obvious plateau suggested the dominating double-layer capacitive behavior of the electrode, which was in accord with earlier results[206]. The triangular shape of the GCD is a typical behavior of highly reversible supercapacitor with constant charge/discharge[188]. As a result, TPTS-SiOC delivered 30 F g^{-1} even at a high current density of 10 A g^{-1}. When tested for cycling stability, the TPTS-SiOC electrode demonstrated 100% capacitance retention over 5000 cycles at 3 A g^{-1}. DDTS- and DTDS-derived SiOC electrodes also

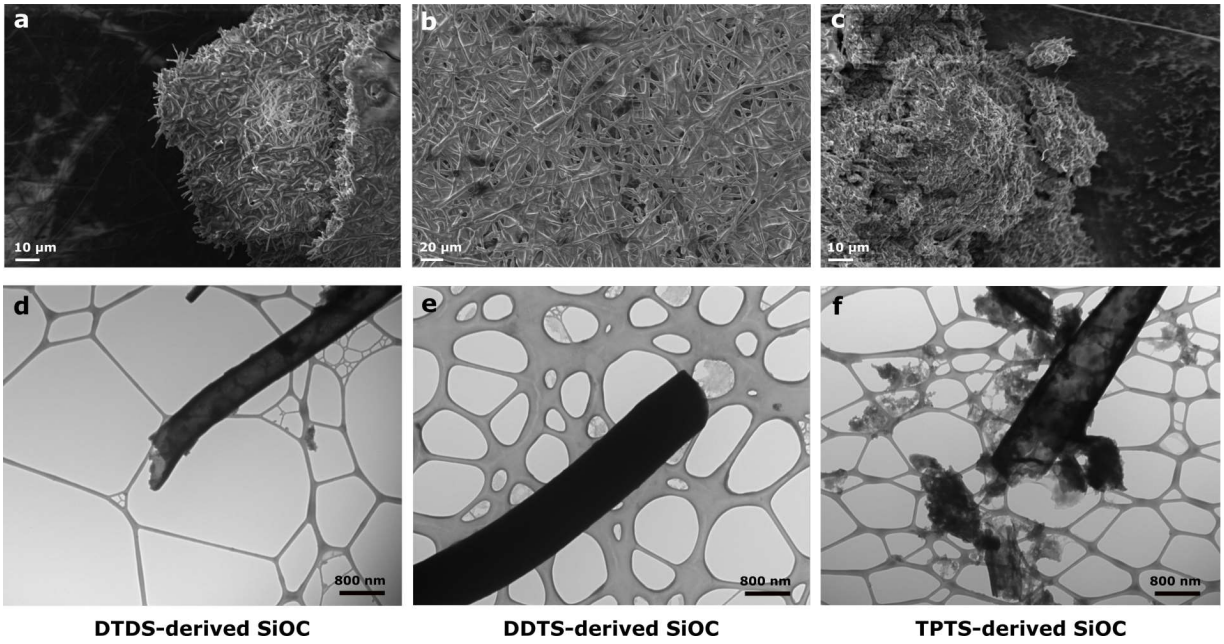

Figure 6.5: *Microscopy analysis of various SiOC electrodes after 400 cycles in LIBs. (a-c) SEM images and (d-f) TEM images. TEM image of TPTS-SiOC shows the broken fiber structure presumably due to the lithiation/delithiation.*

showed stable cycling ability over 5000 cycles as shown in Figure 6.9.

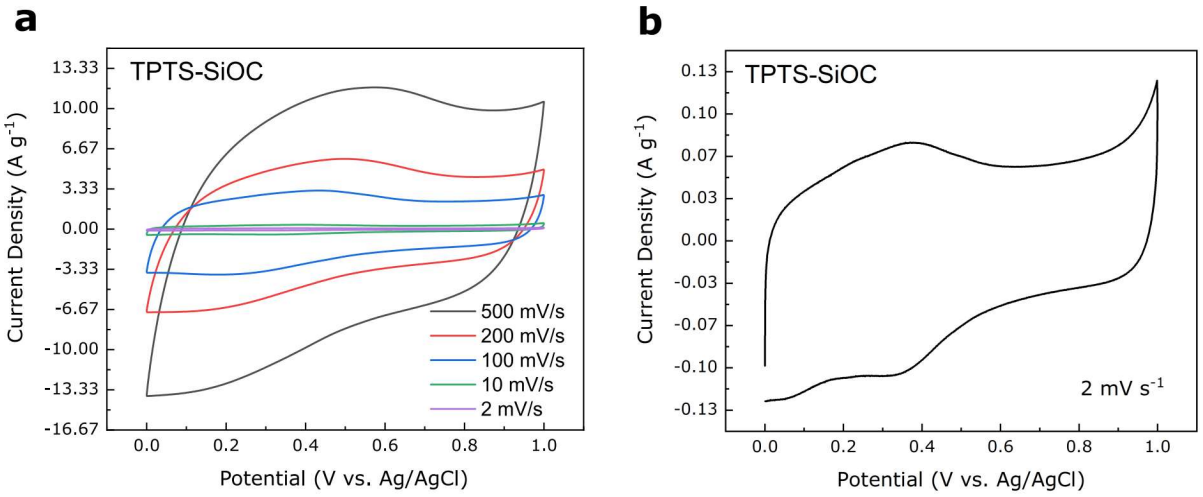

Figure 6.6: *Electrochemical performance of TPTS-derived SiOC supercapacitor electrode in 1M H_2SO_4 aqueous electrolyte. (a) CV profile of the electrode at various scan rate; (b) TPTS-derived SiOC supercapacitor electrodes at a scan rate of 2 mV s^{-1}.*

EIS was done for the various SiOC electrodes to further understand the reaction kinetics of the supercapacitor samples. In Figure 6.10(a), the ohmic resistance, R_s between the

aqueous electrolyte and the electrode was measured in the high frequency region where the curves intercept the Z axis. The semicircle in medium frequency region was attributed to the charge transfer resistance (R_{CT}) of the electrolyte-electrode interface, and the inclined lines in the low frequency region corresponded to the ion diffusion into the SiOC electrode materials[166;207]. An equivalent circuit was obtained for the electrodes, as shown in Figure 6.10(c), from which the calculated RCT for TPTS-SiOC electrode (6) was much lower than the DDTS-SiOC (15) and DTDS-SiOC (50) electrodes. In the low frequency region, the near vertical line to the real axis of the TPTS-SiOC electrode corresponded to the ideal capacitive behavior[208]. Furthermore, the Bode plot (Figure 6.10(b)) showed that TPTS-SiOC had the nearest phase angle (80.5°) to 90°, indicating the best capacitive behavior among the SiOC electrodes[209]. At phase angle of 45°, the relaxation time constant, τ_o ($\tau_o = 1/f_o$) were measured to be 2.61, 6.81, and 56.18 ms for the TPTS-SiOC, DDTS-SiOC, and DTDS-SiOC electrodes, respectively. The significantly lower time constant of the TPTS-SiOC electrode confirmed the fast ion diffusion and transport characteristic as a supercapacitor electrode.

Table 6.1: *BET analysis results*

Pyrolyzed samples	BET surface area ($m^2\ g^{-1}$)	Adsorption avg. pore diameter (Å)
DDTS-derived SiOC	26	39.33
DTDS-derived SiOC	29	42.46
TPTS-derived SiOC	235	18.78

6.5 Conclusions

The amorphous SiOC structures, comprised of free carbon phase and Si-O-C mixed bonds contributed to high reversibility of Li storage. The free carbon phase served as electron conductor as well as the major electrochemically active sites for Li ions, while amorphous Si-O-C network contributed to minor Li storage. In terms of electrochemical properties, the SiOC electrodes displayed excellent capacity with a high coulombic efficiency in LIBs. As supercapacitor electrodes, superior cycleability of 100% capacitance retention over 5000 cycles was achieved. The as-prepared SiOC fiber mats can provide highly efficient, high-

energy, and high-power electrodes and reduce the total weight of the electrochemical energy storage devices.

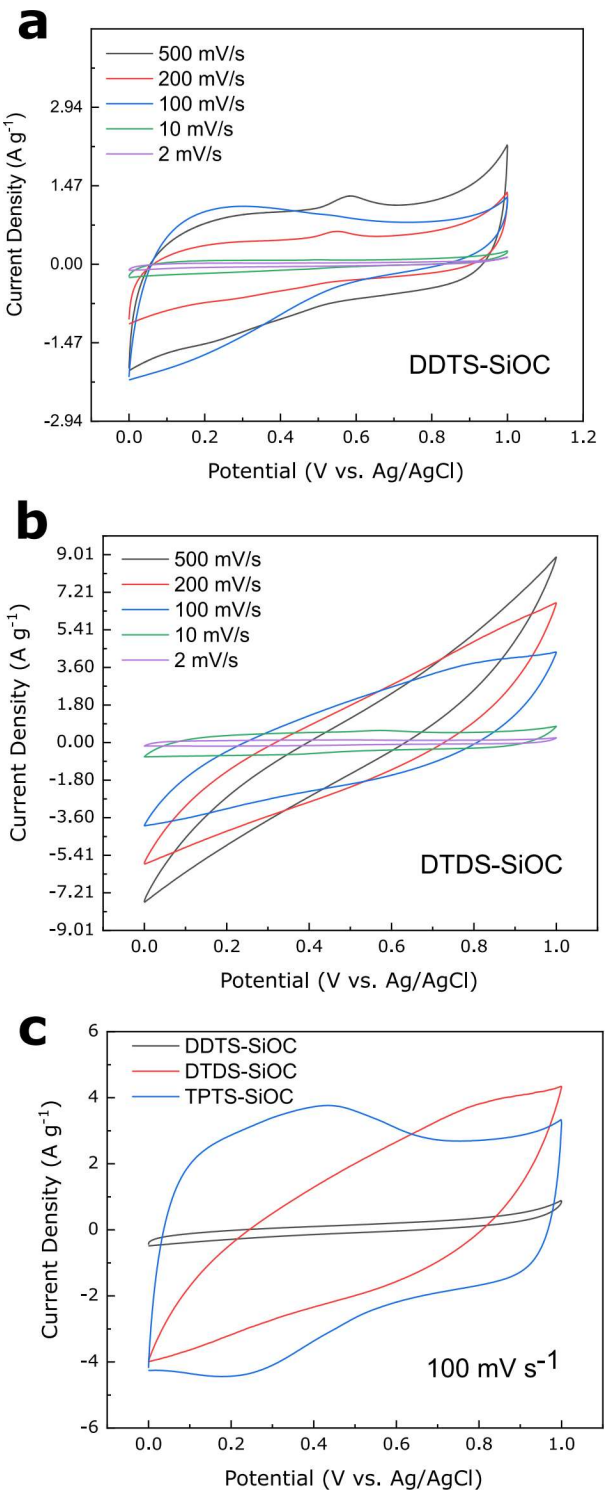

Figure 6.7: *Electrochemical performance of various SiOC supercapacitor electrode in 1M H_2SO_4 aqueous electrolyte. (a-b) CV profiles of the DDTS- and DTDS-derived SiOC supercapacitor electrodes at various scan rate in 1M H_2SO_4 aqueous electrolyte; (c) Comparison of cyclic voltammograms of various electrodes at 100 $mV\ s^{-1}$.*

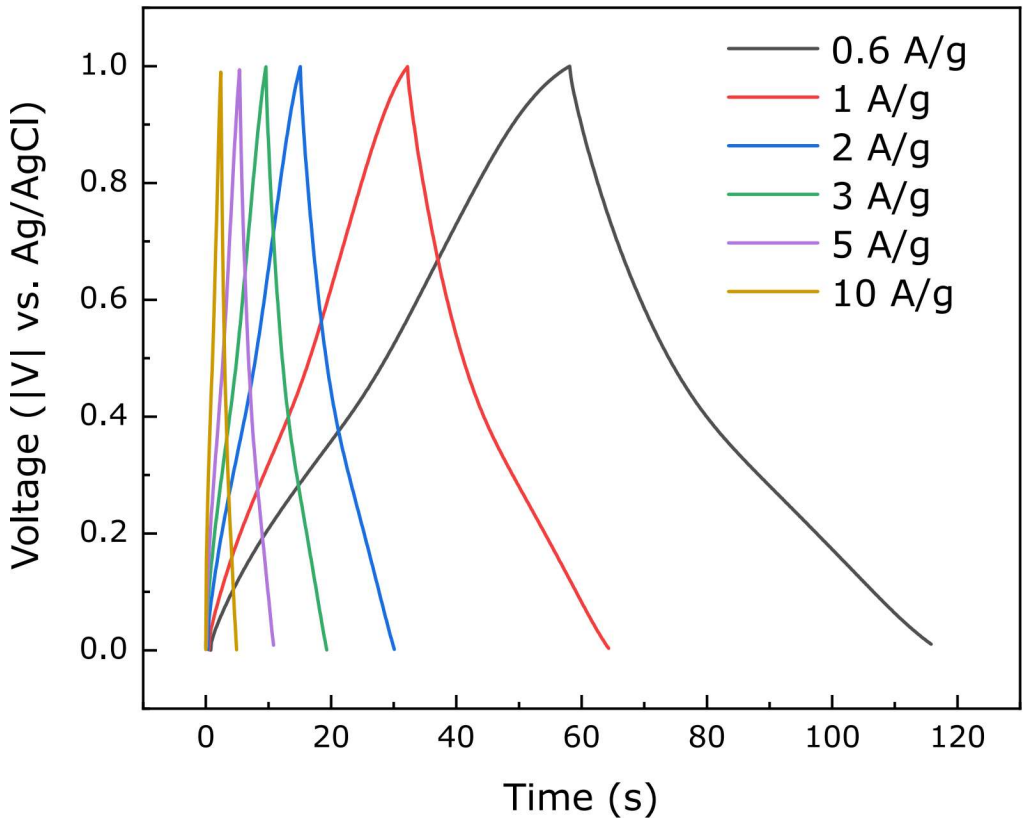

Figure 6.8: *GCD curve of the TPTS-derived SiOC supercapacitor electrode in 1M H_2SO_4 aqueous electrolyte at various current density.*

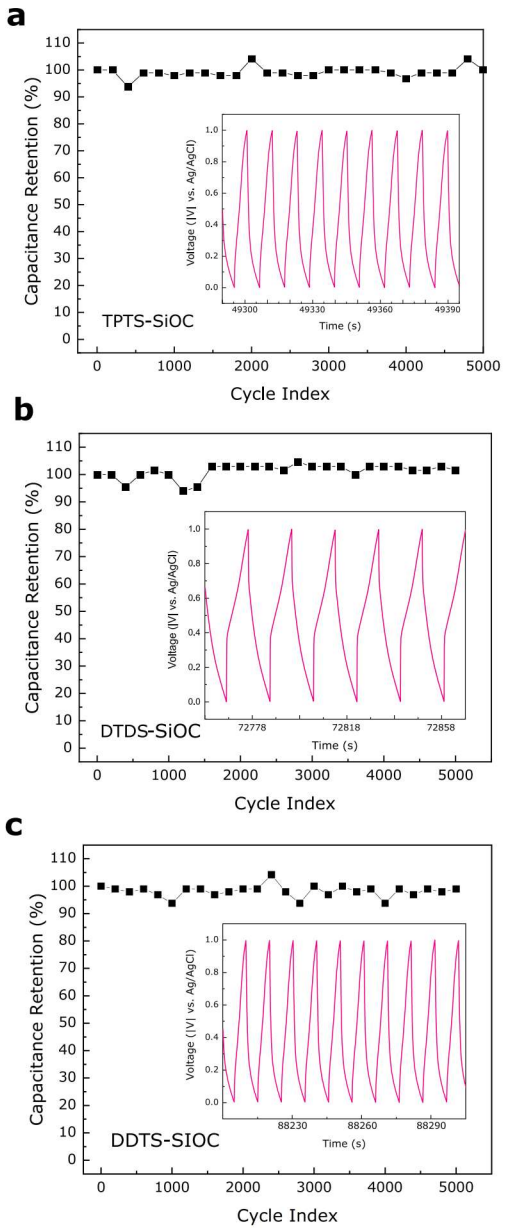

Figure 6.9: *Cycling performance of the precursor-derived SiOC supercapacitor electrodes in 1M H_2SO_4 aqueous electrolyte at 3 A g^{-1}. (a) TPTS-derived SiOC electrode over 5000 cycles shows 100% capacitance retention; (b-c) Capacitance retention trend of DTDS- and DDTS-derived SiOC electrodes also show 100% retention over 5000 cycles.*

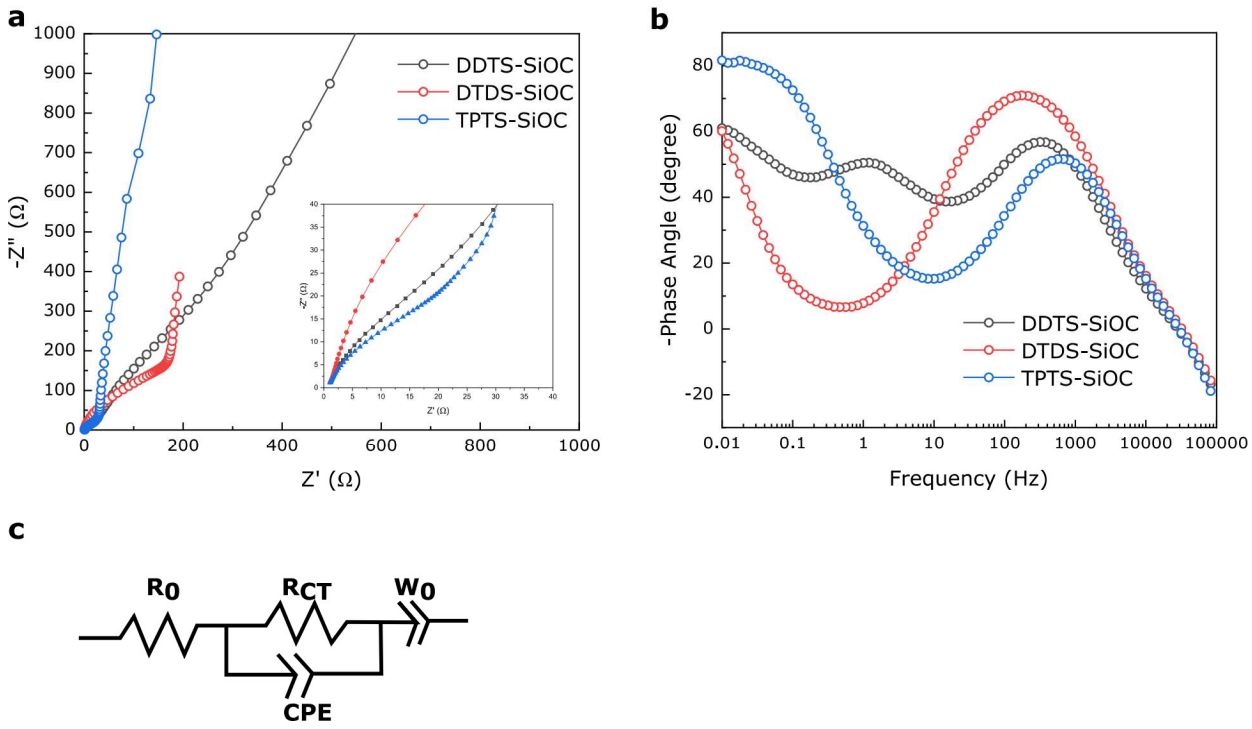

Figure 6.10: *EIS of the various SiOC electrodes in supercapacitors. (a) Comparison of impedance spectra among the various SiOC electrodes; (b) Comparison of Bode plots indicating variation of phase angles among the electrodes; (g) Equivalent circuit derived for the supercapacitor electrodes.*

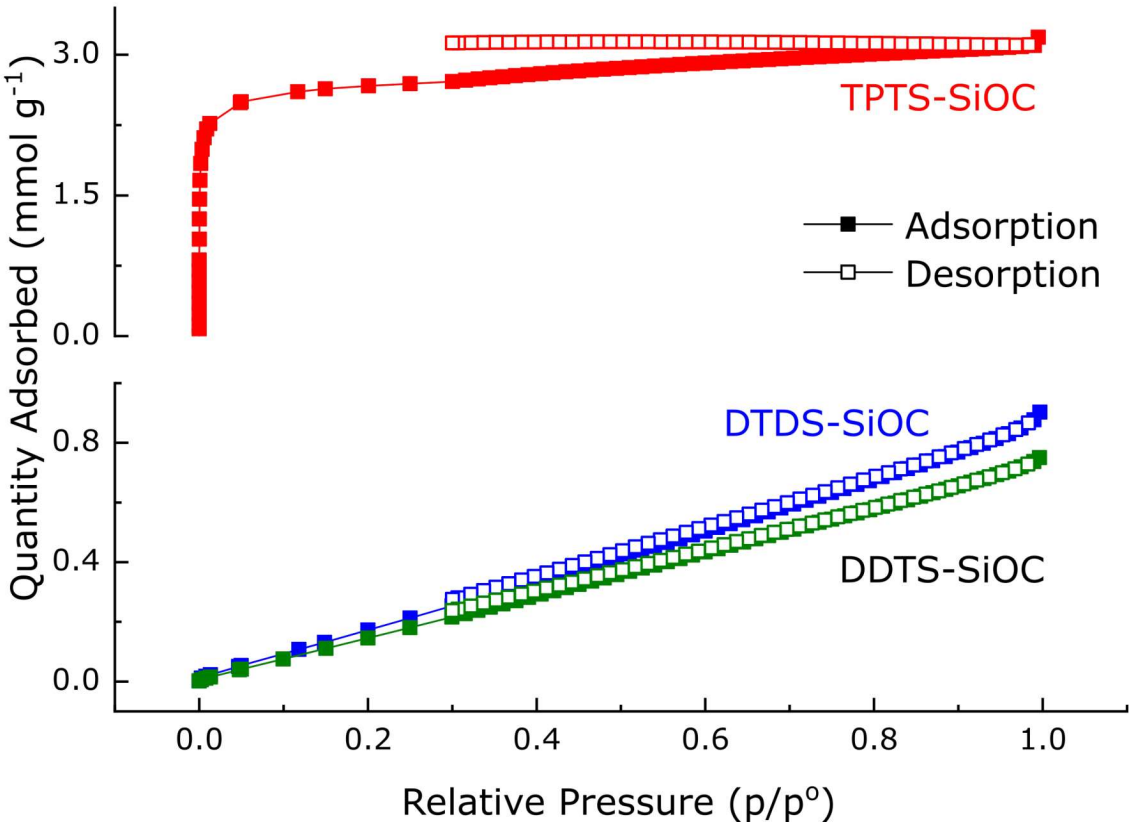

Figure 6.11: *Nitrogen adsorption-desorption isotherms for the BET surface area analysis of various SiOC fibers.*

Chapter 7

Conclusions and Future Directions

The main objective of this dissertation was to understand and characterize the microstructure and properties of the Si-based PDCs. Simple and cost-effective fabrication techniques were used to synthesize PDC fibers and composites from preceramic polymer solutions. This dissertation presented the development of lab-scale fabrication techniques in combination with several microstructure characterization tools for high-temperature PDC materials. Compared to the commercial manufacturing techniques such as melt spinning or wet spinning for fibers, and spark plasma sintering or mechanical alloying and hot-press sintering for CMCs, the reported techniques in this dissertation prposed a simplified synthesis route for PDC fibers and composites in the lab. The role of variability in micrsostructure in affecting the electrochemical properties of the PDC fibers was evaluated through testing as electrodes in LIBs and supercapacitors. The evolution of damage for the PDC mini-composites was evaluated through mechanical loading and oxidation stability experiments.

7.1 Summary

Chapter 1 of this dissertation provided a brief discussion on the material choices for electrochemical energy storage and for high-temperature applications, while motivating the need for further development in PDCs. In this introductory chapter the advantages and challenges

of PDCs as well as CMCs were described and linked to the objectives of this thesis. Replacing traditional electrode materials with PDC fibers in LIBs may improve the capacity and stability of battery. The high-temperature stability of the precursor-derived CMCs provide significant advantage in aerospace applications and allows designing lightweight structural components without compromising the integrity of the structure. The contribution of the thesis can be classified into two objectives: The first objective was focused on the fabrication of PDC fibers and composites and study their microstructures. The second objective was to investigate the properties of the fibers and composites including electrochemical, mechanical, and thermal properties.

Chapter 2 summarizes the previous and current research related to the PDCs and CMCs which are relevant to this dissertation. Materials synthesis and processing, experimental methods, and relation of microstructure to the properties of the PDCs and CMCs were discussed in this chapter. The chapter also highlighted the work of this dissertation within the broader literature of PDCs.

In Chapter 3, a lab-scale drop-coating process was used to fabricate ceramic composites from single-source boron- and hafnium- modified polysilazane precursors. The single-source Si(B)CN and Si(Hf)CN precursors were synthesized by mixing a polysilazane-based precursor with boron- and hafnium-containing precursors, respectively. This chapter studied the efficacy of the infiltration process of carbon fibers cloth and mini-bundles by the preceramic precursor solutions. The infiltrated carbon fibers were then crosslinked and pyrolyzed to achieve Si(B)CN/CF and Si(Hf)CN/CF CMC mini-composites. Morphological and compsoitional analysis of the composites confirmed the presence of ceramics in the samples. The amount of ceramic in the samples were controlled during the infiltration process. Polymer-to-ceramic conversion and microstructures of the samples confirmed the successful fabrication of the ceramic composites by the proposed technique.

To validate the mechanical and thermal stability of the CMC mini-comoposites, tensile and oxidation tests were performed in Chapter 4. Preliminary mechanical tests performed on the composites bundle showed that Si(Hf)CN/CF had the highest tensile strength of 790 MPa and elastic modulus of 66.88 GPa among the ceramic mini-composites. An oxidation

study in ambient air of the Si(Hf)CN/CF ceramic mini-composites showed sample stability up to 1500 °C in air. Si(B)CN/CF samples survived at 1500 °C in air, however, the sample showed shape deformation at temperatures above 1000 °C. Structural and compositional changes of the oxidized samples were investigated via XPS and SEM analyses.

Chapter 5 demonstrated the fabrication process of PDC fibers via electrospinning technique. Three different types of polymeric siloxane precursors were evaluated to fabricate free-standing SiOC fiber mats. The diameter of the fibers were controlled by electrospinning parameters and the produced SiOC fibers had diameters ranging from several microns to hundreds of nanometers. The conditions of the electrospining solutions and process were controlled to achieve high silicon content in the fabricated SiOC fibers. Final compositional analysis confirmed amorphopus SiOC ceramic phase with excessive carbon.

Chapter 6 applied the free-standing SiOC fiber mats as electrodes in LIBs and supercapacitors. These binder-free electrodes were lightweight and improved the electrons and ions transfer within the electrodes materials. Free carbon phase presents in the SiOC structure improved the electronic conductivity and provided active sites for Li^+ ion storage, whereas Si-O-C structure contributed to high efficiency. The self-standing SiOC electrodes in lithium-ion battery half-cells delivered a charge capacity of 866 mAh $g^{-1}_{electrode}$ with a high initial coulombic efficiency of 72%. As supercapacitor electrode, SiOC fibers maintained 100% capacitance over 5000 cycles at a current density of 3 A g^{-1}.

Overall, this dissertation reported scalable and cost-effective methods to fabricate PDC fibers and composites for electrochemical and high-temperature applications. The microsturures of the fabricated samples were correlated with the properties reported in the dissertation. Future studies will need to focus on large sample size and investigate the mechanical properties of the sample at elevated working temperatures.

7.2 Suggested future work

Although the developed techniques and discussed properties of the PDC fibers and composites fill some of the research gaps, new possible areas unfold. Some of the areas that can be

explored in PDCs and CMCs are listed below:

1. To determine the connection in the fiber-matrix interface as well as porosity in the CMCs micro-CT experiments can be conducted. 3D micro-CT segmented images will help to visualize the distribution and orientation of fibers CMCs. micro-CT can also provide information on thickness, porosity, and crack formation in the matrix. The results can be evaluated to improve the density and uniformity of the ceramic coatings. An initial study on the fabricated CMC samples was conducted using an micro-CT. The results are reported in Appendix A.

2. To determine the full potential of CMC mini-composites in aerospace applications, the mechanical testing of the samples should be conducted at high-temperature (1000 °C). High-temperature mechanical testing of a CMC will help to investigate material's change in microstructure and thermal characteristic under tensile load. This test can also provide a comparison between strength and ductility of the CMCs.

3. The fisibility of as-fabricated SiOC ceramic fibers to fabricate CMCs for high-temperature application should be evaluated. A lab-scale polymer infiltration process can be employed to introduce preceramic precursors to the SiOC fibers and accordingly pyrolyzed to fabricate CMCs.

4. Although self-standing carbon-rich SiOC fibers provide excellent capacity performance and stability as an electrode in LIBs, one significant disadvantage of the material is its relatively low first cycle coulombic efficiency (72 %). This is a major hindrance for commercial application of these materials. Future work should focus on improving the first cycle efficiency for PDC materials. One possible solution could be pre-lithiation of the materials during ceramization process.

Bibliography

[1] David Marshall, Brian Cox, Peter Kroll, Greg Hilmas, William Fahrenholtz, Rishi Raj, Robert Ritchie, Qingda Yang, and Frank Zok. National hypersonic science center for materials and structures. Report, TELEDYNE SCIENTIFIC COMPANY THOUSAND OAKS CA, 2014.

[2] S. Schmidt, S. Beyer, H. Knabe, H. Immich, R. Meistring, and A. Gessler. Advanced ceramic matrix composite materials for current and future propulsion technology applications. *Acta Astronautica*, 55(3):409–420, 2004. ISSN 0094-5765. doi: https://doi.org/10.1016/j.actaastro.2004.05.052. URL https://www.sciencedirect.com/science/article/pii/S0094576504001626.

[3] Stephan Schmidt, Steffen Beyer, Hans Immich, Helmut Knabe, Rolf Meistring, and Andreas Gessler. Ceramic matrix composites: A challenge in space-propulsion technology applications. *International Journal of Applied Ceramic Technology*, 2(2):85–96, 2005. ISSN 1546-542X. doi: https://doi.org/10.1111/j.1744-7402.2005.02010.x. URL https://doi.org/10.1111/j.1744-7402.2005.02010.x.

[4] Irene Spitsberg and Jim Steibel. Thermal and environmental barrier coatings for sic/sic cmcs in aircraft engine applications*. *International Journal of Applied Ceramic Technology*, 1(4):291–301, 2004. ISSN 1546-542X. doi: https://doi.org/10.1111/j.1744-7402.2004.tb00181.x. URL https://ceramics.onlinelibrary.wiley.com/doi/abs/10.1111/j.1744-7402.2004.tb00181.x.

[5] S. Yajima, J. Hayashi, M. Omori, and K. Okamura. Development of a silicon carbide fibre with high tensile strength. *Nature*, 261(5562):683–685, 1976. ISSN 1476-4687. doi: 10.1038/261683a0. URL https://doi.org/10.1038/261683a0.

[6] Joachim Bill and Fritz Aldinger. Precursor-derived covalent ceramics*. *Advanced Materials*, 7(9):775–787, 1995. ISSN 0935-9648. doi: https://doi.org/10.1002/adma.19950070903. URL https://onlinelibrary.wiley.com/doi/abs/10.1002/adma.19950070903.

[7] R. Riedel, G. Passing, H. Schönfelder, and R. J. Brook. Synthesis of dense silicon-based ceramics at low temperatures. *Nature*, 355(6362):714–717, 1992. ISSN 1476-4687. doi: 10.1038/355714a0. URL https://doi.org/10.1038/355714a0.

[8] Paolo Colombo, Gabriela Mera, Ralf Riedel, and Gian Domenico Soraru. Polymer-derived ceramics: 40 years of research and innovation in advanced ceramics. *Journal of the American Ceramic Society*, 93(7):1805–1837, 2010. ISSN 0002-7820.

[9] Renjith Devasia, Anil Painuly, Deepa Devapal, and KJ Sreejith. *Continuous fiber reinforced ceramic matrix composites*, pages 669–751. Elsevier, 2021.

[10] Zhongkan Ren, Shakir Bin Mujib, and Gurpreet Singh. High-temperature properties and applications of si-based polymer-derived ceramics: A review. *Materials*, 14(3):614, 2021. ISSN 1996-1944. URL https://www.mdpi.com/1996-1944/14/3/614.

[11] Stephan Trassl, Manfred Puchinger, Ernst Rössler, and Günter Ziegler. Electrical properties of amorphous sicxnyhz-ceramics derived from polyvinylsilazane. *Journal of the European Ceramic Society*, 23(5):781–789, 2003. ISSN 0955-2219. doi: 10.1016/S0955-2219(02)00155-3. URL https://www.sciencedirect.com/science/article/pii/S0955221902001553.

[12] Edwin Kroke, Ya-Li Li, Christoph Konetschny, Emmanuel Lecomte, Claudia Fasel, and Ralf Riedel. Silazane derived ceramics and related materials. *Materials Science and Engineering: R: Reports*, 26(4):97–199, 2000. ISSN 0927-796X. doi: 10.1016/S0927-796X(00)00008-5. URL https://www.sciencedirect.com/science/article/pii/S0927796X00000085.

[13] Emanuel Ionescu, Hans-Joachim Kleebe, and Ralf Riedel. Silicon-containing polymer-derived ceramic nanocomposites (pdc-ncs): preparative approaches and properties. *Chemical Society Reviews*, 41(15):5032–5052, 2012. ISSN 0306-0012. doi: 10.1039/C2CS15319J. URL http://dx.doi.org/10.1039/C2CS15319J.

[14] Paolo Colombo. *Polymer derived ceramics: from nano-structure to applications*. DEStech Publications, Inc, 2010. ISBN 1605950009.

[15] Qingbo Wen, Zhaoju Yu, and Ralf Riedel. The fate and role of in situ formed carbon in polymer-derived ceramics. *Progress in Materials Science*, 109:100623, 2020. ISSN 0079-6425. doi: https://doi.org/10.1016/j.pmatsci.2019.100623. URL https://www.sciencedirect.com/science/article/pii/S0079642519301057.

[16] Gabriela Mera, Alexandra Navrotsky, Sabyasachi Sen, Hans-Joachim Kleebe, and Ralf Riedel. Polymer-derived sicn and sioc ceramics – structure and energetics at the nanoscale. *Journal of Materials Chemistry A*, 1(12):3826–3836, 2013. ISSN 2050-7488. doi: 10.1039/C2TA00727D. URL http://dx.doi.org/10.1039/C2TA00727D.

[17] Dachamir Hotza, Rafael K. Nishihora, Ricardo A. F. Machado, Pierre-Marie Geffroy, Thierry Chartier, and Samuel Bernard. Tape casting of preceramic polymers toward advanced ceramics: A review. *International Journal of Ceramic Engineering & Science*, 1(1):21–41, 2019. doi: https://doi.org/10.1002/ces2.10009. URL https://ceramics.onlinelibrary.wiley.com/doi/abs/10.1002/ces2.10009.

[18] S. Packirisamy, K. J. Sreejith, Deepa Devapal, and B. Swaminathan. *Polymer-Derived Ceramics and Their Space Applications*, pages 1–107. Springer International Publishing, Cham, 2020. ISBN 978-3-319-73255-8. doi: 10.1007/978-3-319-73255-8_31-2. URL https://doi.org/10.1007/978-3-319-73255-8_31-2.

[19] A. Zimmermann, A. Bauer, M. Christ, Y. Cai, and F. Aldinger. High-temperature deformation of amorphous si–c–n and si–b–c–n ceramics derived from polymers. *Acta Materialia*, 50(5):1187–1196, 2002. ISSN 1359-6454. doi: https://doi.org/10.1016/

S1359-6454(01)00420-7. URL https://www.sciencedirect.com/science/article/pii/S1359645401004207.

[20] Anita Müller, Jiangqiang Peng, Hans Jürgen Seifert, Joachim Bill, and Fritz Aldinger. Sibcn ceramic precursors derived from dichlorodivinylsilane and chlorotrivinylsilane. 2. ceramization of polymers and high-temperature behavior of ceramic materials. *Chemistry of Materials*, 14(8):3406–3412, 2002. ISSN 0897-4756. doi: 10.1021/cm021179a. URL https://doi.org/10.1021/cm021179a.

[21] Ralf Hauser, Saifun Nahar-Borchard, Ralf Riedel, Yumi H. Ikuhara, and Yuji Iwamoto. Polymer-derived sibcn ceramic and their potential application for high temperature membranes dedicated to prof. dr.-ing. dr.h.c. hartmut fue223; on the occasion of his 65th birthday. *Journal of the Ceramic Society of Japan*, 114(1330):524–528, 2006. doi: 10.2109/jcersj.114.524.

[22] Song Xie, Yingde Wang, Yongpeng Lei, Bing Wang, Nan Wu, Yanzi Gou, and Dong Fang. A simply prepared flexible siboc ultrafine fiber mat with enhanced high-temperature stability and chemical resistance. *RSC Advances*, 5(80):64911–64917, 2015. doi: 10.1039/C5RA03100A. URL http://dx.doi.org/10.1039/C5RA03100A.

[23] Yang Lyu, Hui Tang, and Guangdong Zhao. Effect of hf and b incorporation on the sioc precursor architecture and high-temperature oxidation behavior of sihfboc ceramics. *Journal of the European Ceramic Society*, 40(2):324–332, 2020. ISSN 0955-2219. doi: https://doi.org/10.1016/j.jeurceramsoc.2019.09.026. URL https://www.sciencedirect.com/science/article/pii/S0955221919306363.

[24] T. Plachký, Z. Lenčéš, Ľ Hric, P. Šajgalík, P. Baláž, R. Riedel, and H. J. Kleebe. Processing and mechanical properties of si3n4 composites employing polymer-derived sialoc as sintering aid. *Journal of the European Ceramic Society*, 30(3):759–767, 2010. ISSN 0955-2219. doi: https://doi.org/10.1016/j.jeurceramsoc.2009.08.014. URL https://www.sciencedirect.com/science/article/pii/S0955221909004130.

[25] Rahul Harshe, Corneliu Balan, and Ralf Riedel. Amorphous si(al)oc ceramic from polysiloxanes: bulk ceramic processing, crystallization behavior and applications. *Journal of the European Ceramic Society*, 24(12):3471–3482, 2004. ISSN 0955-2219. doi: https://doi.org/10.1016/j.jeurceramsoc.2003.10.016. URL https://www.sciencedirect.com/science/article/pii/S0955221903008094.

[26] Yiguang Wang, Yi Fan, Ligong Zhang, Wenge Zhang, and Linan An. Polymer-derived sialcn ceramics resist oxidation at 1400°c. *Scripta Materialia*, 55(4):295–297, 2006. ISSN 1359-6462. doi: https://doi.org/10.1016/j.scriptamat.2006.05.004. URL https://www.sciencedirect.com/science/article/pii/S1359646206003708.

[27] Ganesh Babu Thiyagarajan, Ekaterina Koroleva, Alexey Filimonov, Sergey Vakhrushev, and Ravi Kumar. Tailorable dielectric performance of niobium-modified poly(hydridomethylsiloxane) precursor-derived ceramic nanocomposites. *physica status solidi (a)*, 217(22):2000417, 2020. ISSN 1862-6300. doi: https://doi.org/10.1002/pssa.202000417. URL https://onlinelibrary.wiley.com/doi/abs/10.1002/pssa.202000417.

[28] Emanuel Ionescu, Christoph Linck, Claudia Fasel, Mathis Müller, Hans–Joachim Kleebe, and Ralf Riedel. Polymer-derived sioc/zro2 ceramic nanocomposites with excellent high-temperature stability. *Journal of the American Ceramic Society*, 93 (1):241–250, 2010. ISSN 0002-7820. doi: https://doi.org/10.1111/j.1551-2916.2009.03395.x. URL https://ceramics.onlinelibrary.wiley.com/doi/abs/10.1111/j.1551-2916.2009.03395.x.

[29] Dong Su, Xiao Yan, Ning Liu, Xiaolei Li, and Huiming Ji. Preparation and characterization of continuous sizroc fibers by polyvinyl pyrrolidone-assisted sol–gel process. *Journal of Materials Science*, 51(3):1418–1427, 2016. ISSN 1573-4803. doi: 10.1007/s10853-015-9461-7. URL https://doi.org/10.1007/s10853-015-9461-7.

[30] Rahul Anand, Bibhuti B. Nayak, and Shantanu K. Behera. Coarsening kinetics of nanostructured zro2 in zr-doped sicn ceramic hybrids. *Journal of Alloys and*

Compounds, 811:151939, 2019. ISSN 0925-8388. doi: https://doi.org/10.1016/j.jallcom.2019.151939. URL https://www.sciencedirect.com/science/article/pii/S0925838819331834.

[31] Nicole Hering, Kai Schreiber, Ralf Riedel, Olaf Lichtenberger, and Jörg Woltersdorf. Synthesis of polymeric precursors for the formation of nanocrystalline ti-c-n/amorphous si-c-n composites. *Applied Organometallic Chemistry*, 15(10):879–886, 2001. ISSN 0268-2605. doi: https://doi.org/10.1002/aoc.241. URL https://onlinelibrary.wiley.com/doi/abs/10.1002/aoc.241.

[32] Yuxi Yu, Yadi Guo, Xuan Cheng, and Ying Zhang. Preparation of tio2/sio2 composite fiber by thermal decomposition of polycarbosilane–tetrabutyl titanate hybrid precursor. *Journal of Materials Chemistry*, 19(31):5637–5642, 2009. ISSN 0959-9428. doi: 10.1039/B905860E. URL http://dx.doi.org/10.1039/B905860E.

[33] Ravindran Sujith, Andre Zimmermann, and Ravi Kumar. Crack evolution and estimation of fracture toughness of hfo2/sicn(o) polymer derived ceramic nanocomposites. *Advanced Engineering Materials*, 17(9):1265–1269, 2015. ISSN 1438-1656. doi: https://doi.org/10.1002/adem.201400525. URL https://onlinelibrary.wiley.com/doi/abs/10.1002/adem.201400525.

[34] Xiao Yan, Dong Su, Haozhi Duan, and Fengrui Zhang. Preparation of sioc/hfo2 fibers from silicon alkoxides and tetrachloride hafnium by a sol–gel process. *Materials Letters*, 148:196–199, 2015. ISSN 0167-577X. doi: https://doi.org/10.1016/j.matlet.2015.02.067. URL https://www.sciencedirect.com/science/article/pii/S0167577X15002645.

[35] Ravindran Sujith, Adhimoolam Bakthavachalam Kousaalya, and Ravi Kumar. Synthesis and phase stability of precursor derived hfo2/si–c–n–o nanocomposites. *Ceramics International*, 38(2):1227–1233, 2012. ISSN 0272-8842. doi: https://doi.org/10.1016/j.ceramint.2011.08.053. URL https://www.sciencedirect.com/science/article/pii/S0272884211007656.

[36] Jia Sun, Qing-Bo Wen, Tao Li, Leonore Wiehl, Claudia Fasel, Yao Feng, Dario De Carolis, Zhao-Ju Yu, Qian-Gang Fu, and Ralf Riedel. Phase evolution of sioc-based ceramic nanocomposites derived from a polymethylsiloxane modified by hf- and ti-alkoxides. *Journal of the American Ceramic Society*, 103(2):1436–1445, 2020. ISSN 0002-7820. doi: https://doi.org/10.1111/jace.16817. URL https://ceramics.onlinelibrary.wiley.com/doi/abs/10.1111/jace.16817.

[37] Ralf Riedel. From molecules to materials — a novel route for the synthesis of advanced ceramics. *Naturwissenschaften*, 82(1):12–20, 1995. ISSN 1432-1904. doi: 10.1007/BF01167864. URL https://doi.org/10.1007/BF01167864.

[38] W David Kingery, Harvey Kent Bowen, and Donald R Uhlmann. *Introduction to ceramics*, volume 17. John wiley sons, 1976. ISBN 0471478601.

[39] Robert B Heimann. *Classic and advanced ceramics: from fundamentals to applications*. John Wiley Sons, 2010. ISBN 352763018X.

[40] C Barry Carter and M Grant Norton. *Ceramic materials: science and engineering*, volume 716. Springer, 2007.

[41] Henry George Liddell and Robert Scott. *An intermediate Greek-English lexicon: founded upon the seventh edition of Liddell and Scott's Greek-English lexicon*. Clarendon Press, 1900.

[42] Greg Geiger. Introduction to ceramics. *American Ceramic Society*, 2011.

[43] Joachim Bill and Fritz Aldinger. Precursor-derived covalent ceramics*. *Advanced Materials*, 7(9):775–787, 1995. ISSN 0935-9648. doi: https://doi.org/10.1002/adma.19950070903. URL https://onlinelibrary.wiley.com/doi/abs/10.1002/adma.19950070903.

[44] Ralf Riedel, Gabriela Mera, Ralf Hauser, and Alexander Klonczynski. Silicon-based polymer-derived ceramics: Synthesis properties and applications-a review dedicated to

prof. dr. fritz aldinger on the occasion of his 65th birthday. *Journal of the Ceramic Society of Japan*, 114(1330):425–444, 2006. doi: 10.2109/jcersj.114.425.

[45] Brahma Raju Golla, Amartya Mukhopadhyay, Bikramjit Basu, and Sravan Kumar Thimmappa. Review on ultra-high temperature boride ceramics. *Progress in Materials Science*, 111:100651, 2020. ISSN 0079-6425. doi: https://doi.org/10.1016/j.pmatsci.2020.100651. URL https://www.sciencedirect.com/science/article/pii/S0079642520300153.

[46] David Glass. *Ceramic Matrix Composite (CMC) Thermal Protection Systems (TPS) and Hot Structures for Hypersonic Vehicles*. International Space Planes and Hypersonic Systems and Technologies Conferences. American Institute of Aeronautics and Astronautics, 2008. doi: doi:10.2514/6.2008-268210.2514/6.2008-2682. URL https://doi.org/10.2514/6.2008-2682.

[47] K. Chawla. *Ceramic Matrix Composites*. 2003. doi: 10.1007/978-1-4615-1029-1.

[48] I. W. Donald and P. W. McMillan. Ceramic-matrix composites. *Journal of Materials Science*, 11(5):949–972, 1976. ISSN 1573-4803. doi: 10.1007/BF00542312. URL https://doi.org/10.1007/BF00542312.

[49] Lisa M. Rueschhoff, Carmen M. Carney, Zlatomir D. Apostolov, and Michael K. Cinibulk. Processing of fiber-reinforced ultra-high temperature ceramic composites: A review. *International Journal of Ceramic Engineering Science*, 2(1):22–37, 2020. doi: https://doi.org/10.1002/ces2.10033. URL https://doi.org/10.1002/ces2.10033.

[50] Rebecca Gottlieb, Shannon Poges, Chris Monteleone, Steven L Suib, Steven L Suib, A Tiwari, RA Gerhardt, and M Szutkowska. Continuous fiber-reinforced ceramic matrix composites. *Advanced Ceramic Materials*, pages 146–199, 2016.

[51] Laura Silvestroni, Diletta Sciti, Cesare Melandri, and Stefano Guicciardi. Toughened zrb2-based ceramics through sic whisker or sic chopped fiber additions. *Journal of the European Ceramic Society*, 30(11):2155–2164, 2010. ISSN 0955-2219. doi: https:

//doi.org/10.1016/j.jeurceramsoc.2009.11.012. URL https://www.sciencedirect.com/science/article/pii/S0955221909005688.

[52] I. Crivelli-Visconti and G. A. Cooper. Mechanical properties of a new carbon fibre material. *Nature*, 221(5182):754–755, 1969. ISSN 1476-4687. doi: 10.1038/221754a0. URL https://doi.org/10.1038/221754a0.

[53] M. W. Lindley and D. J. Godfrey. Silicon nitride ceramic composites with high toughness. *Nature*, 229(5281):192–193, 1971. ISSN 1476-4687. doi: 10.1038/229192b0. URL https://doi.org/10.1038/229192b0.

[54] R. A. J. Sambell, A. Briggs, D. C. Phillips, and D. H. Bowen. Carbon fibre composites with ceramic and glass matrices. *Journal of Materials Science*, 7(6):676–681, 1972. ISSN 1573-4803. doi: 10.1007/BF00549379. URL https://doi.org/10.1007/BF00549379.

[55] R. A. J. Sambell, D. H. Bowen, and D. C. Phillips. Carbon fibre composites with ceramic and glass matrices. *Journal of Materials Science*, 7(6):663–675, 1972. ISSN 1573-4803. doi: 10.1007/BF00549378. URL https://doi.org/10.1007/BF00549378.

[56] F. F. Lange. Effect of microstructure on strength of si3n4-sic composite system. *Journal of the American Ceramic Society*, 56(9):445–450, 1973. ISSN 0002-7820. doi: https://doi.org/10.1111/j.1151-2916.1973.tb12520.x. URL https://doi.org/10.1111/j.1151-2916.1973.tb12520.x.

[57] R Kennedy. Ceramic matrix composite technology is ge's centerpiece jet propulsion strategy for the 21st century. *The GE Aviation Blog—Aerospace Flight News.(2019).[online] Available at: https://blog. geaviation. com/technology/42869/[Accessed 18 Oct. 2021]*, 2019.

[58] Michele Ferraiuolo, Roberto Scigliano, Aniello Riccio, Emanuele Bottone, and Marco Rennella. Thermo-structural design of a ceramic matrix composite wing leading

edge for a re-entry vehicle. *Composite Structures*, 207:264–272, 2019. ISSN 0263-8223. doi: https://doi.org/10.1016/j.compstruct.2018.09.024. URL https://www.sciencedirect.com/science/article/pii/S0263822318326606.

[59] D. Kopeliovich. *5 - Advances in the manufacture of ceramic matrix composites using infiltration techniques*, pages 79–108. Woodhead Publishing, 2014. ISBN 978-0-85709-120-8. doi: https://doi.org/10.1533/9780857098825.1.79. URL https://www.sciencedirect.com/science/article/pii/B9780857091208500058.

[60] Manish Patel, Kumar Saurabh, V. V. Bhanu Prasad, and J. Subrahmanyam. High temperature c/c–sic composite by liquid silicon infiltration: a literature review. *Bulletin of Materials Science*, 35(1):63–73, 2012. ISSN 0973-7669. doi: 10.1007/s12034-011-0247-5. URL https://doi.org/10.1007/s12034-011-0247-5.

[61] Günter Motz, Stephan Schmidt, and Steffen Beyer. The pip-process: precursor properties and applications. *Ceramic matrix composites: fiber reinforced ceramics and their applications*, pages 165–186, 2008.

[62] Renato Luiz Siqueira, Inez Valéria Pagotto Yoshida, Luiz Claudio Pardini, and Marco Antônio Schiavon. Poly (borosiloxanes) as precursors for carbon fiber ceramic matrix composites. *Materials Research*, 10:147–151, 2007. ISSN 1516-1439.

[63] R. Jones, A. Szweda, and D. Petrak. Polymer derived ceramic matrix composites. *Composites Part A: Applied Science and Manufacturing*, 30(4):569–575, 1999. ISSN 1359-835X. doi: https://doi.org/10.1016/S1359-835X(98)00151-1. URL https://www.sciencedirect.com/science/article/pii/S1359835X98001511.

[64] T. Ganesh Babu, Anil Painuly, and Renjith Devasia. Novel silazane modified phenol formaldehyde derived cf/pyc/sic-si3n4 composites with improved mechanical strength for thermo-structural applications. *Materials Today: Proceedings*, 5(11, Part 3):25056–25064, 2018. ISSN 2214-7853. doi: https://doi.org/10.1016/j.matpr.2018.10.306. URL https://www.sciencedirect.com/science/article/pii/S2214785318326063.

[65] Aldo Donato, Carlo Alberto Nannetti, Alberto Ortona, Elisabetta Borsella, Sabina Botti, Sergio Casadio, Gianni D'alessandro, Antonio Alessandro Licciulli, Stefano Martelli, Amedeo Masci, et al. Process for producing ceramic matrix composites by liquid infiltration of ceramic polymeric precursors, December 29 1998. US Patent 5,853,653.

[66] Qingbo Wen, Yeping Xu, Binbin Xu, Claudia Fasel, Olivier Guillon, Gerd Buntkowsky, Zhaoju Yu, Ralf Riedel, and Emanuel Ionescu. Single-source-precursor synthesis of dense sic/hfc x n 1 x-based ultrahigh-temperature ceramic nanocomposites. *Nanoscale*, 6(22):13678–13689, 2014.

[67] Qinggang Li, Shaoming Dong, Zhen Wang, Ping He, Haijun Zhou, Jinshan Yang, Bin Wu, and Jianbao Hu. Fabrication and properties of 3-dc f/sic–zrc composites, using zrc precursor and polycarbosilane. *Journal of the American Ceramic Society*, 95(4): 1216–1219, 2012. ISSN 0002-7820.

[68] William B Hillig. Melt infiltration approach to ceramic matrix composites. *Journal of the American Ceramic Society*, 71(2):C-96–C-99, 1988. ISSN 0002-7820.

[69] Yutaro Arai, Tomoki Marumo, and Ryo Inoue. Use of zr–ti alloy melt infiltration for fabricating carbon-fiber-reinforced ultrahigh-temperature ceramic matrix composites. *Journal of Composites Science*, 5(7):186, 2021. ISSN 2504-477X.

[70] Natalie Wali and JM Yang. Reactive melt-infiltration processing of fiber-reinforced ceramic matrix composites. *Ceramics and Composites Processing Methods*, page 351, 2012. ISSN 0470553448.

[71] Marius Kütemeyer, Laura Schomer, Thomas Helmreich, Stefan Rosiwal, and Dietmar Koch. Fabrication of ultra high temperature ceramic matrix composites using a reactive melt infiltration process. *Journal of the European Ceramic Society*, 36(15):3647–3655, 2016. ISSN 0955-2219.

[72] Marius Kütemeyer, Thomas Helmreich, Stefan Rosiwal, and Dietmar Koch. Influence of zirconium-based alloys on manufacturing and mechanical properties of ultra high temperature ceramic matrix composites. *Advances in Applied Ceramics*, 117(sup1): s62–s69, 2018. ISSN 1743-6753.

[73] J. Schulte-Fischedick, A. Zern, J. Mayer, M. Rühle, M. Frieß, W. Krenkel, and R. Kochendörfer. The morphology of silicon carbide in c/c–sic composites. *Materials Science and Engineering: A*, 332(1):146–152, 2002. ISSN 0921-5093. doi: https://doi.org/10.1016/S0921-5093(01)01719-1. URL https://www.sciencedirect.com/science/article/pii/S0921509301017191.

[74] Takuya Aoki, Toshio Ogasawara, Yosuke Okubo, Katsumi Yoshida, and Toyohiko Yano. Fabrication and properties of si hf alloy melt-infiltrated tyranno zmi fiber/sic-based matrix composites. *Composites Part A: Applied Science and Manufacturing*, 66: 155–162, 2014. ISSN 1359-835X.

[75] Huilong Pi, Shangwu Fan, and Yiguang Wang. C/sic–zrb2–zrc composites fabricated by reactive melt infiltration with zrsi2 alloy. *Ceramics International*, 38(8):6541–6548, 2012. ISSN 0272-8842.

[76] Yuki Kubota, Yutaro Arai, Mamoru Yano, Ryo Inoue, Ken Goto, and Yasuo Kogo. Oxidation and recession of plain weave carbon fiber reinforced zrb2-sic-zrc in oxygen–hydrogen torch environment. *Journal of the European Ceramic Society*, 39(9): 2812–2823, 2019. ISSN 0955-2219.

[77] Bernhard Heidenreich. Carbon fibre reinforced sic materials based on melt infiltration. In *6th International Conference on High Temperature Ceramic Matrix Composites HTCMC 6*, 2007.

[78] P McAllister and EE Wolf. Modeling of chemical vapor infiltration of carbon in porous carbon substrates. *Carbon*, 29(3):387–396, 1991. ISSN 0008-6223.

[79] GQ Lu. Modelling the densification of porous structures in cvi ceramic composites processing. *Journal of Materials Processing Technology*, 37(1-4):487–498, 1993. ISSN 0924-0136.

[80] Walter Krenkel. *Ceramic matrix composites: fiber reinforced ceramics and their applications*. John Wiley Sons, 2008. ISBN 3527313613.

[81] A Sayir. Carbon fiber reinforced hafnium carbide composite. *Journal of materials science*, 39(19):5995–6003, 2004. ISSN 1573-4803.

[82] Haijun Zhou, Dewei Ni, Ping He, Jinshan Yang, Jianbao Hu, and Shaoming Dong. Ablation behavior of c/c-zrc and c/sic-zrc composites fabricated by a joint process of slurry impregnation and chemical vapor infiltration. *Ceramics International*, 44(5): 4777–4782, 2018. ISSN 0272-8842.

[83] V. Rubio, P. Ramanujam, and J. Binner. Ultra-high temperature ceramic composite. *Advances in Applied Ceramics*, 117(sup1):s56–s61, 2018. ISSN 1743-6753. doi: 10.1080/17436753.2018.1475140. URL https://doi.org/10.1080/17436753.2018.1475140.

[84] Shangwu Fan, Chuan Yang, Liuyang He, Yong Du, Walter Krenkel, Peter Greil, and Nahum Travitzky. Progress of ceramic matrix composites brake materials for aircraft application. *Rev. Adv. Mater. Sci*, 44:313–325, 2016.

[85] Yoram de Hazan and Dirk Penner. Sic and sioc ceramic articles produced by stereolithography of acrylate modified polycarbosilane systems. *Journal of the European Ceramic Society*, 37(16):5205–5212, 2017. ISSN 0955-2219.

[86] Yuelong Fu, Gang Xu, Zhangwei Chen, Daming Wang, and Changshi Lao. Multiple metals doped polymer-derived sioc ceramics for 3d printing. *Ceramics International*, 44(10):11030–11038, 2018. ISSN 0272-8842.

[87] Zak C Eckel, Chaoyin Zhou, John H Martin, Alan J Jacobsen, William B Carter, and

Tobias A Schaedler. Additive manufacturing of polymer-derived ceramics. *Science*, 351(6268):58–62, 2016. ISSN 0036-8075.

[88] Shan Li, Wenyan Duan, Tong Zhao, Weijian Han, Li Wang, Rui Dou, and Gong Wang. The fabrication of sibcn ceramic components from preceramic polymers by digital light processing (dlp) 3d printing technology. *Journal of the European Ceramic Society*, 38 (14):4597–4603, 2018. ISSN 0955-2219.

[89] Andrea Zocca, Cynthia M Gomes, Andreas Staude, Enrico Bernardo, Jens Günster, and Paolo Colombo. Sioc ceramics with ordered porosity by 3d-printing of a preceramic polymer. *Journal of Materials Research*, 28(17):2243–2252, 2013. ISSN 0884-2914.

[90] Giovanni Pierin, Chiara Grotta, Paolo Colombo, and Cecilia Mattevi. Direct ink writing of micrometric sioc ceramic structures using a preceramic polymer. *Journal of the European Ceramic Society*, 36(7):1589–1594, 2016. ISSN 0955-2219.

[91] Giorgia Franchin, Larissa Wahl, and Paolo Colombo. Direct ink writing of ceramic matrix composite structures. *Journal of the American Ceramic Society*, 100(10):4397–4401, 2017. ISSN 0002-7820. doi: https://doi.org/10.1111/jace.15045. URL https://doi.org/10.1111/jace.15045.

[92] Nasser Kanani. *The Parthian Battery: Electric Current 2000 Years Ago?; the History of Surface Finishing*. Leuze, 2004. ISBN 3874801969.

[93] M. S. Whittingham. History, evolution, and future status of energy storage. *Proceedings of the IEEE*, 100(Special Centennial Issue):1518–1534, 2012. ISSN 1558-2256. doi: 10.1109/JPROC.2012.2190170.

[94] Abolhassan Noori, Maher F. El-Kady, Mohammad S. Rahmanifar, Richard B. Kaner, and Mir F. Mousavi. Towards establishing standard performance metrics for batteries, supercapacitors and beyond. *Chemical Society Reviews*, 48(5):1272–1341, 2019. ISSN 0306-0012. doi: 10.1039/C8CS00581H. URL http://dx.doi.org/10.1039/C8CS00581H.

[95] Rising demand for lithium-ion batteries may lead to shortages in raw material supply. *Roland Berger*, Apr 2022. URL https://rolandberger-com.mynewsdesk.com/pressreleases/rising-demand-for-lithium-ion-batteries-may-lead-to-shortages-in-raw-material-supp

[96] Evan M. Erickson, Chandan Ghanty, and Doron Aurbach. New horizons for conventional lithium ion battery technology. *The Journal of Physical Chemistry Letters*, 5(19):3313–3324, 2014. doi: 10.1021/jz501387m10.1021/jz501387m⟨/p⟩. URL https://doi.org/10.1021/jz501387m.

[97] Maria R. Lukatskaya, Bruce Dunn, and Yury Gogotsi. Multidimensional materials and device architectures for future hybrid energy storage. *Nature Communications*, 7(1): 12647, 2016. ISSN 2041-1723. doi: 10.1038/ncomms12647. URL https://doi.org/10.1038/ncomms12647.

[98] Michel Armand, Peter Axmann, Dominic Bresser, Mark Copley, Kristina Edström, Christian Ekberg, Dominique Guyomard, Bernard Lestriez, Petr Novák, Martina Petranikova, Willy Porcher, Sigita Trabesinger, Margret Wohlfahrt-Mehrens, and Heng Zhang. Lithium-ion batteries – current state of the art and anticipated developments. *Journal of Power Sources*, 479:228708, 2020. ISSN 0378-7753. doi: https://doi.org/10.1016/j.jpowsour.2020.228708. URL https://www.sciencedirect.com/science/article/pii/S0378775320310120.

[99] Yu Miao, Patrick Hynan, Annette von Jouanne, and Alexandre Yokochi. Current li-ion battery technologies in electric vehicles and opportunities for advancements. *Energies*, 12(6), 2019. ISSN 1996-1073. doi: 10.3390/en12061074. URL https://www.mdpi.com/1996-1073/12/6/1074.

[100] Thomas S Kuhn. *The structure of scientific revolutions*, volume 111. Chicago University of Chicago Press, 1970.

[101] Vladimir S Bagotsky, Alexander M Skundin, and Yurij M Volfkovich. *Electrochemical power sources: batteries, fuel cells, and supercapacitors*. John Wiley & Sons, 2015.

[102] Adam Namisnyk and J Zhu. A survey of electrochemical super-capacitor technology. In *Australian Universities Power Engineering Conference*. University of Canterbury, New Zealand, 2003.

[103] Sergio Trasatti and Giovanni Buzzanca. Ruthenium dioxide: A new interesting electrode material. solid state structure and electrochemical behaviour. *Journal of Electroanalytical Chemistry and Interfacial Electrochemistry*, 29(2):A1–A5, 1971. ISSN 0022-0728. doi: https://doi.org/10.1016/S0022-0728(71)80111-0. URL https://www.sciencedirect.com/science/article/pii/S0022072871801110.

[104] Parnia Forouzandeh, Vignesh Kumaravel, and Suresh C. Pillai. Electrode materials for supercapacitors: A review of recent advances. *Catalysts*, 10(9), 2020. ISSN 2073-4344. doi: 10.3390/catal10090969. URL https://www.mdpi.com/2073-4344/10/9/969.

[105] Katlego Makgopa, Letlhogonolo F. Mabena, Cheslin G. Brink, Given N. Chauke, Malesela D. Teffu, Kwena D. Modibane, and Mpitloane J. Hato. *Nanostructured Carbon-Based Electrode Materials for Supercapacitor Applications*, pages 317–355. Springer Singapore, Singapore, 2021. ISBN 978-981-15-7610-2. doi: 10.1007/978-981-15-7610-2_14. URL https://doi.org/10.1007/978-981-15-7610-2_14.

[106] Cheng Zhong, Yida Deng, Wenbin Hu, Jinli Qiao, Lei Zhang, and Jiujun Zhang. A review of electrolyte materials and compositions for electrochemical supercapacitors. *Chem. Soc. Rev.*, 44:7484–7539, 2015. doi: 10.1039/C5CS00303B. URL http://dx.doi.org/10.1039/C5CS00303B.

[107] Shakir Bin Mujib and Gurpreet Singh. Polymer derived sioc and sicn ceramics for electrochemical energy storage: A perspective. *International Journal of Ceramic Engineering Science*, n/a(n/a):1–6, 2021. doi: https://doi.org/10.1002/ces2.10108. URL https://ceramics.onlinelibrary.wiley.com/doi/abs/10.1002/ces2.10108.

[108] Gilvan Barroso, Quan Li, Rajendra K. Bordia, and Günter Motz. Polymeric and ceramic silicon-based coatings – a review. *Journal of Materials Chemistry A*, 7(5): 1936–1963, 2019. ISSN 2050-7488. doi: 10.1039/C8TA09054H. URL http://dx.doi.org/10.1039/C8TA09054H.

[109] Rotem Marom, S. Francis Amalraj, Nicole Leifer, David Jacob, and Doron Aurbach. A review of advanced and practical lithium battery materials. *Journal of Materials Chemistry*, 21(27):9938–9954, 2011. ISSN 0959-9428. doi: 10.1039/C0JM04225K. URL http://dx.doi.org/10.1039/C0JM04225K.

[110] J. C. Zhao and J. H. Westbrook. Ultrahigh-temperature materials for jet engines. *MRS Bulletin*, 28(9):622–630, 2003. ISSN 0883-7694. doi: 10.1557/mrs2003.189. URL https://www.cambridge.org/core/article/ultrahightemperature-materials-for-jet-engines/D1FE91E128EE62C25CE9324881538248.

[111] Nitin P. Padture. Advanced structural ceramics in aerospace propulsion. *Nature Materials*, 15(8):804–809, 2016. ISSN 1476-4660. doi: 10.1038/nmat4687. URL https://doi.org/10.1038/nmat4687.

[112] Yuan Wang and Houzheng Wu. Microstructure of friction surface developed on carbon fibre reinforced carbon–silicon carbide (cf/c–sic). *Journal of the European Ceramic Society*, 32(12):3509–3519, 2012. ISSN 0955-2219. doi: https://doi.org/10.1016/j.jeurceramsoc.2012.03.039. URL https://www.sciencedirect.com/science/article/pii/S0955221912001859.

[113] Anish Paul, Daniel Doni Jayaseelan, Saranya Venugopal, E Zapata-Solvas, JGP Binner, Vaidhy Vaidhyanathan, A Heaton, Peter M Brown, and WE Lee. Uhtc composites for hypersonic applications. 2012.

[114] Min Berbon and Mike Calabrese. Effect of 1600°c heat treatment on c/sic composites fabricated by polymer infiltration and pyrolysis with allylhydridopolycarbosilane.

Journal of the American Ceramic Society, 85(7):1891–1893, 2002. ISSN 0002-7820. doi: https://doi.org/10.1111/j.1151-2916.2002.tb00374.x. URL https://ceramics.onlinelibrary.wiley.com/doi/abs/10.1111/j.1151-2916.2002.tb00374.x.

[115] R. Naslain and F. Christin. Sic-matrix composite materials for advanced jet engines. *MRS Bulletin*, 28(9):654–658, 2003. ISSN 0883-7694. doi: 10.1557/mrs2003.193. URL https://www.cambridge.org/core/article/sicmatrix-composite-materials-for-advanced-jet-engines/C051CFAD3DFF78119D14777D6E0E67FB.

[116] Frank W Zok. Ceramic-matrix composites enable revolutionary gains in turbine engine efficiency. *Am Ceram Soc Bull*, 95(5):22–8, 2016.

[117] Zhongkan Ren and Gurpreet Singh. Nonoxide polymer-derived cmcs for "super" turbines. *Journal Name: American Ceramic Society bulletin; Journal Volume: 98; Journal Issue: 3; Conference: null; Patent File Date: null; Patent Priority Date: null; Other Information: null; Related Information: null*, pages Medium: X; Size: 34–39; Quantity: null; OS: null; Compatibility: null; Other: null, 2019. ISSN null; Journal ID: 0002-7812; RD Project: null; Other: null; TRN: null Country unknown/Code not availablehttps://doi.org/nullJournal ID: 0002-7812; RD Project: null; Other: null; TRN: nullnullOSTI-MSA; nullnull.

[118] Qingbo Wen, Zhaoju Yu, and Ralf Riedel. The fate and role of in situ formed carbon in polymer-derived ceramics. *Progress in Materials Science*, 109:100623, 2020. ISSN 0079-6425. doi: https://doi.org/10.1016/j.pmatsci.2019.100623. URL https://www.sciencedirect.com/science/article/pii/S0079642519301057.

[119] Martin Friess, Joachim Bill, Jerzy Golczewski, Andre Zimmermann, Fritz Aldinger, Ralf Riedel, and Rishi Raj. Crystallization of polymer-derived silicon carbonitride at 1873 k under nitrogen overpressure. *Journal of the American Ceramic Society*, 85 (10):2587–2589, 2002. ISSN 0002-7820. doi: https://doi.org/10.1111/j.1151-2916.2002.

tb00503.x. URL https://ceramics.onlinelibrary.wiley.com/doi/abs/10.1111/j.1151-2916.2002.tb00503.x.

[120] E. Bernardo, I. Ponsot, P. Colombo, S. Grasso, H. Porwal, and M. J. Reece. Polymer-derived sic ceramics from polycarbosilane/boron mixtures densified by sps. *Ceramics International*, 40(9, Part A):14493–14500, 2014. ISSN 0272-8842. doi: https://doi.org/10.1016/j.ceramint.2014.07.008. URL https://www.sciencedirect.com/science/article/pii/S0272884214010414.

[121] Hans-Joachim Kleebe, Giuliano Gregori, Florence Babonneau, Yigal D. Blum, D. Brent MacQueen, and Sylvie Masse. Evolution of c-rich sioc ceramics: Part i. characterization by integral spectroscopic techniques: Solid-state nmr and raman spectroscopy. *International Journal of Materials Research*, 97(6):699–709, 2006. doi: doi:10.3139/ijmr-2006-0115. URL https://doi.org/10.3139/ijmr-2006-0115.

[122] Paolo Colombo, Gabriela Mera, Ralf Riedel, and Gian Domenico Soraru. Polymer-derived ceramics: 40 years of research and innovation in advanced ceramics. *Journal of the American Ceramic Society*, 93(7):1805–1837, 2010. ISSN 0002-7820.

[123] A. Zimmermann, A. Bauer, M. Christ, Y. Cai, and F. Aldinger. High-temperature deformation of amorphous si–c–n and si–b–c–n ceramics derived from polymers. *Acta Materialia*, 50(5):1187–1196, 2002. ISSN 1359-6454. doi: https://doi.org/10.1016/S1359-6454(01)00420-7. URL https://www.sciencedirect.com/science/article/pii/S1359645401004207.

[124] Rahul Harshe, Corneliu Balan, and Ralf Riedel. Amorphous si(al)oc ceramic from polysiloxanes: bulk ceramic processing, crystallization behavior and applications. *Journal of the European Ceramic Society*, 24(12):3471–3482, 2004. ISSN 0955-2219. doi: https://doi.org/10.1016/j.jeurceramsoc.2003.10.016. URL https://www.sciencedirect.com/science/article/pii/S0955221903008094.

[125] Rahul Anand, Bibhuti B. Nayak, and Shantanu K. Behera. Coarsening kinetics

of nanostructured zro2 in zr-doped sicn ceramic hybrids. *Journal of Alloys and Compounds*, 811:151939, 2019. ISSN 0925-8388. doi: https://doi.org/10.1016/j.jallcom.2019.151939. URL https://www.sciencedirect.com/science/article/pii/S0925838819331834.

[126] Xueyuan Tang, Yuxi Yu, and Daxiang Yang. Sio2/tio2 fibers from titanium-modified polycarbosilane. *Journal of Materials Science*, 45(10):2670–2674, 2010. ISSN 1573-4803. doi: 10.1007/s10853-010-4247-4. URL https://doi.org/10.1007/s10853-010-4247-4.

[127] Jia Sun, Qing-Bo Wen, Tao Li, Leonore Wiehl, Claudia Fasel, Yao Feng, Dario De Carolis, Zhao-Ju Yu, Qian-Gang Fu, and Ralf Riedel. Phase evolution of sioc-based ceramic nanocomposites derived from a polymethylsiloxane modified by hf- and ti-alkoxides. *Journal of the American Ceramic Society*, 103(2):1436–1445, 2020. ISSN 0002-7820. doi: https://doi.org/10.1111/jace.16817. URL https://ceramics.onlinelibrary.wiley.com/doi/abs/10.1111/jace.16817.

[128] Zhongkan Ren, Shakir Bin Mujib, and Gurpreet Singh. High-temperature properties and applications of si-based polymer-derived ceramics: A review. *Materials*, 14(3):614, 2021. ISSN 1996-1944. URL https://www.mdpi.com/1996-1944/14/3/614.

[129] See Hoon Lee, Markus Weinmann, and Fritz Aldinger. Processing and properties of c/si–b–c–n fiber–reinforced ceramic matrix composites prepared by precursor impregnation and pyrolysis. *Acta Materialia*, 56(7):1529–1538, 2008. ISSN 1359-6454. doi: https://doi.org/10.1016/j.actamat.2007.12.001. URL https://www.sciencedirect.com/science/article/pii/S1359645407008324.

[130] Markus Weinmann, Jörg Schuhmacher, Horst Kummer, Sabine Prinz, Jianqiang Peng, Hans Jürgen Seifert, Martin Christ, Klaus Müller, Joachim Bill, and Fritz Aldinger. Synthesis and thermal behavior of novel sibcn ceramic precursors. *Chemistry of Materials*, 12(3):623–632, 2000. ISSN 0897-4756. doi: 10.1021/cm9910299. URL https://doi.org/10.1021/cm9910299.

[131] Hui Zhao, Lixin Chen, Xingang Luan, Xiaofei Zhang, Jin Yun, and Tingting Xu. Synthesis, pyrolysis of a novel liquid sibcn ceramic precursor and its application in ceramic matrix composites. *Journal of the European Ceramic Society*, 37(4):1321–1329, 2017. ISSN 0955-2219. doi: https://doi.org/10.1016/j.jeurceramsoc.2016.11.009. URL https://www.sciencedirect.com/science/article/pii/S0955221916305982.

[132] Jia Yuan, Stefania Hapis, Hergen Breitzke, Yeping Xu, Claudia Fasel, Hans-Joachim Kleebe, Gerd Buntkowsky, Ralf Riedel, and Emanuel Ionescu. Single-source-precursor synthesis of hafnium-containing ultrahigh-temperature ceramic nanocomposites (uhtc-ncs). *Inorganic Chemistry*, 53(19):10443–10455, 2014. ISSN 0020-1669. doi: 10.1021/ic501512p. URL https://doi.org/10.1021/ic501512p.

[133] Qingbo Wen, Xingang Luan, Lei Wang, Xinming Xu, Emanuel Ionescu, and Ralf Riedel. Laser ablation behavior of sihfc-based ceramics prepared from a single-source precursor: Effects of hf-incorporation into sic. *Journal of the European Ceramic Society*, 39(6):2018–2027, 2019. ISSN 0955-2219. doi: https://doi.org/10.1016/j.jeurceramsoc.2019.01.040. URL https://www.sciencedirect.com/science/article/pii/S0955221919300524.

[134] Yuquan Wei, Yong Yang, Meng Liu, Qile Li, and Zhengren Huang. Oxidation mechanism and kinetics of sibcn/hfc ceramic composites at high temperatures. *Journal of Materials Research and Technology*, 9(2):2289–2298, 2020. ISSN 2238-7854. doi: https://doi.org/10.1016/j.jmrt.2019.12.060. URL https://www.sciencedirect.com/science/article/pii/S2238785419314206.

[135] Yang Miao, Fengnian Zhang, Zhihua Yang, Dechang Jia, and Yu Zhou. Incorporation of bn-coated carbon fibers into zrb2/sibcn ceramic composites and their ablation behavior. *Journal of the European Ceramic Society*, 40(4):1078–1085, 2020. ISSN 0955-2219. doi: https://doi.org/10.1016/j.jeurceramsoc.2019.12.031. URL https://www.sciencedirect.com/science/article/pii/S0955221919308751.

[136] Gurpreet Singh and Romil Bhandavat. Boron-modified silazanes for synthesis of sibnc ceramics, September 27 2016. US Patent 9,453,111.

[137] Binbin Dong, Yehu Han, Ting Wang, Zhanwu Lei, Yawei Chen, Feihong Wang, Hamidreza Abadikhah, Sayed Ali Khan, Luyuan Hao, Xin Xu, Ruiguo Cao, Liangjun Yin, and Simeon Agathopoulos. Hard sioc microbeads as a high-performance lithium-ion battery anode. *ACS Applied Energy Materials*, 3(10):10183–10191, 2020. doi: 10.1021/acsaem.0c0191010.1021/acsaem.0c01910⟨/p⟩. URL https://doi.org/10.1021/acsaem.0c01910.

[138] Shakir Bin Mujib, François Ribot, Christel Gervais, and Gurpreet Singh. Self-supporting carbon-rich sioc ceramic electrodes for lithium-ion batteries and aqueous supercapacitors. *RSC Advances*, 11(56):35440–35454, 2021. doi: 10.1039/D1RA05968H. URL http://dx.doi.org/10.1039/D1RA05968H.

[139] Qian Zhang, Zhihua Yang, Dechang Jia, Qingqing Chen, and Yu Zhou. Synthesis and structural evolution of dual-boron-source-modified polysilazane derived sibcn ceramics. *New Journal of Chemistry*, 40(8):7034–7042, 2016. ISSN 1144-0546. doi: 10.1039/C5NJ03723A. URL http://dx.doi.org/10.1039/C5NJ03723A.

[140] Kiho Kim, Hyun Ju, and Jooheon Kim. Pyrolysis behavior of polysilazane and polysilazane-coated-boron nitride for high thermal conductive composite. *Composites Science and Technology*, 141:1–7, 2017. ISSN 0266-3538. doi: https://doi.org/10.1016/j.compscitech.2017.01.003. URL https://www.sciencedirect.com/science/article/pii/S026635381631404X.

[141] Ricardo Chavez, Emanuel Ionescu, Corneliu Balan, Claudia Fasel, and Ralf Riedel. Effect of ambient atmosphere on crosslinking of polysilazanes. *Journal of Applied Polymer Science*, 119(2):794–802, 2011. ISSN 0021-8995. doi: https://doi.org/10.1002/app.32777. URL https://onlinelibrary.wiley.com/doi/abs/10.1002/app.32777.

[142] S. L. Ma, B. Xu, K. W. Xu, X. L. Wu, and Paul K. Chu. Annealing behavior and hardness enhancement of amorphous sicn thin films. *Journal of Vacuum Science Technology A*, 25(5):1407–1410, 2007. doi: 10.1116/1.2764080. URL https://avs.scitation.org/doi/abs/10.1116/1.2764080.

[143] R. Bhandavat, A. Feldman, C. Cromer, J. Lehman, and G. Singh. Very high laser-damage threshold of polymer-derived si(b)cn- carbon nanotube composite coatings. *ACS Applied Materials Interfaces*, 5(7):2354–2359, 2013. ISSN 1944-8244. doi: 10.1021/am302755x. URL https://doi.org/10.1021/am302755x.

[144] Seunghyup Lee, Dong-Jin Yun, Shi-Woo Rhee, and Kijung Yong. Atomic layer deposition of hafnium silicate film for high mobility pentacene thin film transistor applications. *Journal of Materials Chemistry*, 19(37):6857–6864, 2009. ISSN 0959-9428. doi: 10.1039/B908216F. URL http://dx.doi.org/10.1039/B908216F.

[145] Gouri Syamala Rao Mullapudi, Gonzalo Alonso Velazquez-Nevarez, Carlos Avila-Avendano, Jorge Alejandro Torres-Ochoa, Manuel Angel Quevedo-López, and Rafael Ramírez-Bon. Low-temperature deposition of inorganic–organic hfo2–pmma hybrid gate dielectric layers for high-mobility zno thin-film transistors. *ACS Applied Electronic Materials*, 1(6):1003–1011, 2019. doi: 10.1021/acsaelm.9b00175. URL https://doi.org/10.1021/acsaelm.9b00175.

[146] Gurpreet Singh and Lamuel David. Aluminum-modified polysilazanes for polymer-derived ceramic nanocomposites, March 6 2018. US Patent 9,908,905.

[147] Gurpreet Singh and Lamuel David. Silicon-based polymer-derived ceramic composites comprising h-bn nanosheets, October 9 2018. US Patent 10,093,584.

[148] Jie Kong, Minjun Wang, Jianhua Zou, and Linan An. Soluble and meltable hyperbranched polyborosilazanes toward high-temperature stable sibcn ceramics. *ACS Applied Materials Interfaces*, 7(12):6733–6744, 2015. ISSN 1944-8244. doi: 10.1021/am509129a. URL https://doi.org/10.1021/am509129a.

[149] Emanuel Ionescu, Benjamin Papendorf, Hans-Joachim Kleebe, and Ralf Riedel. Polymer-derived silicon oxycarbide/hafnia ceramic nanocomposites. part ii: Stability toward decomposition and microstructure evolution at t1000°c. *Journal of the American Ceramic Society*, 93(6):1783–1789, 2010. ISSN 0002-7820. doi: https://doi.org/10.1111/j.1551-2916.2009.03527.x. URL https://ceramics.onlinelibrary.wiley.com/doi/abs/10.1111/j.1551-2916.2009.03527.x.

[150] Evan B. Callaway and Frank W. Zok. Strengths of ceramic fiber bundles: Theory and practice. *Journal of the American Ceramic Society*, 100(11):5306–5317, 2017. ISSN 0002-7820. doi: https://doi.org/10.1111/jace.15062. URL https://ceramics.onlinelibrary.wiley.com/doi/abs/10.1111/jace.15062.

[151] Yoshito Ikarashi, Toshio Ogasawara, Shin-ichi Okuizumi, Takuya Aoki, Ian J. Davies, and Jacques Lamon. Direct comparison between monofilament and multifilament tow testing for evaluating the tensile strength distribution of sic fibers. *Journal of the European Ceramic Society*, 42(5):1928–1937, 2022. ISSN 0955-2219. doi: https://doi.org/10.1016/j.jeurceramsoc.2021.12.051. URL https://www.sciencedirect.com/science/article/pii/S0955221921009468.

[152] Setareh Azarnoush, Franli Laubscher, Luca Zoli, and Rishi Raj. Additive manufacturing of sicn ceramic matrix for sic fiber composites by flash pyrolysis of nanoscale polymer films. *Journal of the American Ceramic Society*, 99(6):1855–1858, 2016. ISSN 0002-7820. doi: https://doi.org/10.1111/jace.14145. URL https://ceramics.onlinelibrary.wiley.com/doi/abs/10.1111/jace.14145.

[153] Narottam P Bansal and Jeffrey I Eldridge. Effects of fiber/matrix interface and its composition on mechanical properties of hi-nicalon/celsian composites. Report, 1999.

[154] Sandeep Kumar, S. B. Rai, and Chandana Rath. Multifunctional role of dysprosium in hfo2: stabilization of the high temperature cubic phase, and magnetic and photoluminescence properties. *Physical Chemistry Chemical Physics*, 19(29):18957–18967,

2017. ISSN 1463-9076. doi: 10.1039/C7CP02800H. URL http://dx.doi.org/10.1039/C7CP02800H.

[155] Rishi Raj, Linan An, Sandeep Shah, Ralf Riedel, Claudia Fasel, and Hans-Joachim Kleebe. Oxidation kinetics of an amorphous silicon carbonitride ceramic. *Journal of the American Ceramic Society*, 84(8):1803–1810, 2001. ISSN 0002-7820. doi: https://doi.org/10.1111/j.1151-2916.2001.tb00918.x. URL https://ceramics.onlinelibrary.wiley.com/doi/abs/10.1111/j.1151-2916.2001.tb00918.x.

[156] Biao Lu and Yue Zhang. Oxidation behavior of sic–sibcn ceramics. *Ceramics International*, 41(1, Part B):1023–1030, 2015. ISSN 0272-8842. doi: https://doi.org/10.1016/j.ceramint.2014.09.025. URL https://www.sciencedirect.com/science/article/pii/S0272884214014102.

[157] C. Verdon, O. Szwedek, A. Allemand, S. Jacques, Y. Le Petitcorps, and P. David. High temperature oxidation of two- and three-dimensional hafnium carbide and silicon carbide coatings. *Journal of the European Ceramic Society*, 34(4):879–887, 2014. ISSN 0955-2219. doi: https://doi.org/10.1016/j.jeurceramsoc.2013.10.019. URL https://www.sciencedirect.com/science/article/pii/S0955221913004792.

[158] Xiao Hua Liu, Li Zhong, Shan Huang, Scott X. Mao, Ting Zhu, and Jian Yu Huang. Size-dependent fracture of silicon nanoparticles during lithiation. *ACS Nano*, 6(2):1522–1531, 2012. ISSN 1936-0851. doi: 10.1021/nn204476h. URL https://doi.org/10.1021/nn204476h.

[159] Thomas M. Higgins, Sang-Hoon Park, Paul J. King, Chuanfang Zhang, Niall McEvoy, Nina C. Berner, Dermot Daly, Aleksey Shmeliov, Umar Khan, Georg Duesberg, Valeria Nicolosi, and Jonathan N. Coleman. A commercial conducting polymer as both binder and conductive additive for silicon nanoparticle-based lithium-ion battery negative electrodes. *ACS Nano*, 10(3):3702–3713, 2016. ISSN 1936-0851. doi: 10.1021/acsnano.6b00218. URL https://doi.org/10.1021/acsnano.6b00218.

[160] Junsu Park, Seokho Suh, Sungho Jeong, and Hyeong-Jin Kim. New approach for the high electrochemical performance of silicon anode in lithium-ion battery: A rapid and large surface treatment using a high-energy pulsed laser. *Journal of Power Sources*, 491:229573, 2021. ISSN 0378-7753. doi: https://doi.org/10.1016/j.jpowsour.2021.229573. URL https://www.sciencedirect.com/science/article/pii/S0378775321001191.

[161] Dingchang Lin, Zhenda Lu, Po-Chun Hsu, Hye Ryoung Lee, Nian Liu, Jie Zhao, Haotian Wang, Chong Liu, and Yi Cui. A high tap density secondary silicon particle anode fabricated by scalable mechanical pressing for lithium-ion batteries. *Energy Environmental Science*, 8(8):2371–2376, 2015. ISSN 1754-5692. doi: 10.1039/C5EE01363A. URL http://dx.doi.org/10.1039/C5EE01363A.

[162] Xiao Hua Liu, Li Qiang Zhang, Li Zhong, Yang Liu, He Zheng, Jiang Wei Wang, Jeong-Hyun Cho, Shadi A. Dayeh, S. Tom Picraux, John P. Sullivan, Scott X. Mao, Zhi Zhen Ye, and Jian Yu Huang. Ultrafast electrochemical lithiation of individual si nanowire anodes. *Nano Letters*, 11(6):2251–2258, 2011. ISSN 1530-6984. doi: 10.1021/nl200412p. URL https://doi.org/10.1021/nl200412p.

[163] Bin Wang, Jaegeon Ryu, Sungho Choi, Xinghao Zhang, Didier Pribat, Xianglong Li, Linjie Zhi, Soojin Park, and Rodney S. Ruoff. Ultrafast-charging silicon-based coral-like network anodes for lithium-ion batteries with high energy and power densities. *ACS Nano*, 13(2):2307–2315, 2019. ISSN 1936-0851. doi: 10.1021/acsnano.8b09034. URL https://doi.org/10.1021/acsnano.8b09034.

[164] Mi-Hee Park, Min Gyu Kim, Jaebum Joo, Kitae Kim, Jeyoung Kim, Soonho Ahn, Yi Cui, and Jaephil Cho. Silicon nanotube battery anodes. *Nano Letters*, 9(11):3844–3847, 2009. ISSN 1530-6984. doi: 10.1021/nl902058c. URL https://doi.org/10.1021/nl902058c.

[165] Xiao Hua Liu, He Zheng, Li Zhong, Shan Huang, Khim Karki, Li Qiang Zhang, Yang Liu, Akihiro Kushima, Wen Tao Liang, Jiang Wei Wang, Jeong-Hyun Cho,

Eric Epstein, Shadi A. Dayeh, S. Tom Picraux, Ting Zhu, Ju Li, John P. Sullivan, John Cumings, Chunsheng Wang, Scott X. Mao, Zhi Zhen Ye, Sulin Zhang, and Jian Yu Huang. Anisotropic swelling and fracture of silicon nanowires during lithiation. *Nano Letters*, 11(8):3312–3318, 2011. ISSN 1530-6984. doi: 10.1021/nl201684d. URL https://doi.org/10.1021/nl201684d.

[166] Candace K. Chan, Hailin Peng, Gao Liu, Kevin McIlwrath, Xiao Feng Zhang, Robert A. Huggins, and Yi Cui. High-performance lithium battery anodes using silicon nanowires. *Nature Nanotechnology*, 3(1):31–35, 2008. ISSN 1748-3395. doi: 10.1038/nnano.2007.411. URL https://doi.org/10.1038/nnano.2007.411.

[167] See-How Ng, Jiazhao Wang, David Wexler, Konstantin Konstantinov, Zai-Ping Guo, and Hua-Kun Liu. Highly reversible lithium storage in spheroidal carbon-coated silicon nanocomposites as anodes for lithium-ion batteries. *Angewandte Chemie International Edition*, 45(41):6896–6899, 2006. ISSN 1433-7851. doi: https://doi.org/10.1002/anie.200601676. URL https://onlinelibrary.wiley.com/doi/abs/10.1002/anie.200601676.

[168] Minseong Ko, Sujong Chae, Jiyoung Ma, Namhyung Kim, Hyun-Wook Lee, Yi Cui, and Jaephil Cho. Scalable synthesis of silicon-nanolayer-embedded graphite for high-energy lithium-ion batteries. *Nature Energy*, 1(9):16113, 2016. ISSN 2058-7546. doi: 10.1038/nenergy.2016.113. URL https://doi.org/10.1038/nenergy.2016.113.

[169] Gemeng Liang, Xianying Qin, Jinshuo Zou, Laiyan Luo, Yunzhe Wang, Mengyao Wu, Hua Zhu, Guohua Chen, Feiyu Kang, and Baohua Li. Electrosprayed silicon-embedded porous carbon microspheres as lithium-ion battery anodes with exceptional rate capacities. *Carbon*, 127:424–431, 2018. ISSN 0008-6223. doi: https://doi.org/10.1016/j.carbon.2017.11.013. URL https://www.sciencedirect.com/science/article/pii/S0008622317311168.

[170] Kai Wang, Shien Pei, Zhishun He, Liang-ai Huang, Shasha Zhu, Jianfeng Guo, Haibo Shao, and Jianming Wang. Synthesis of a novel porous silicon microsphere@carbon

core-shell composite via in situ mof coating for lithium ion battery anodes. *Chemical Engineering Journal*, 356:272–281, 2019. ISSN 1385-8947. doi: https://doi.org/10.1016/j.cej.2018.09.027. URL https://www.sciencedirect.com/science/article/pii/S1385894718317352.

[171] Peng Li, Jang-Yeon Hwang, and Yang-Kook Sun. Nano/microstructured silicon–graphite composite anode for high-energy-density li-ion battery. *ACS Nano*, 13(2):2624–2633, 2019. ISSN 1936-0851. doi: 10.1021/acsnano.9b00169. URL https://doi.org/10.1021/acsnano.9b00169.

[172] Lei Zhang, Chengrui Wang, Yuhai Dou, Ningyan Cheng, Dandan Cui, Yi Du, Porun Liu, Mohammad Al-Mamun, Shanqing Zhang, and Huijun Zhao. A yolk–shell structured silicon anode with superior conductivity and high tap density for full lithium-ion batteries. *Angewandte Chemie International Edition*, 58(26):8824–8828, 2019. ISSN 1433-7851. doi: https://doi.org/10.1002/anie.201903709. URL https://onlinelibrary.wiley.com/doi/abs/10.1002/anie.201903709.

[173] Formhals Anton. Process and apparatus for preparing artificial threads, October 2 1934. US Patent 1,975,504.

[174] Formhals Anton. Method and apparatus for spinning, June 6 1939. US Patent 2,160,962.

[175] Yunhua Xu, Yujie Zhu, Fudong Han, Chao Luo, and Chunsheng Wang. 3d si/c fiber paper electrodes fabricated using a combined electrospray/electrospinning technique for li-ion batteries. *Advanced Energy Materials*, 5(1):1400753, 2015. ISSN 1614-6832. doi: https://doi.org/10.1002/aenm.201400753. URL https://onlinelibrary.wiley.com/doi/abs/10.1002/aenm.201400753.

[176] Qizhen Xiao, Qing Zhang, Yu Fan, Xinghui Wang, and Rahmat Agung Susantyoko. Soft silicon anodes for lithium ion batteries. *Energy Environmental Science*, 7(7):

2261–2268, 2014. ISSN 1754-5692. doi: 10.1039/C4EE00768A. URL http://dx.doi.org/10.1039/C4EE00768A.

[177] Zhongkan Ren, Christel Gervais, and Gurpreet Singh. Fabrication and characterization of silicon oxycarbide fibre-mats via electrospinning for high temperature applications. *RSC Advances*, 10(63):38446–38455, 2020. doi: 10.1039/D0RA04060F. URL http://dx.doi.org/10.1039/D0RA04060F.

[178] Zhongkan Ren and Gurpreet Singh. Nonoxide polymer-derived cmcs for "super" turbines. *American Ceramic Society bulletin*, 98(3), 2019.

[179] Shahin Homaeigohar, Yalda Davoudpour, Youssef Habibi, and Mady Elbahri. The electrospun ceramic hollow nanofibers. *Nanomaterials (Basel, Switzerland)*, 7(11):383, 2017. ISSN 2079-4991. doi: 10.3390/nano7110383. URL https://pubmed.ncbi.nlm.nih.gov/29120403https://www.ncbi.nlm.nih.gov/pmc/articles/PMC5707600/.

[180] Jeong F. Kim, Ji Hoon Kim, Young Moo Lee, and Enrico Drioli. Thermally induced phase separation and electrospinning methods for emerging membrane applications: A review. *AIChE Journal*, 62(2):461–490, 2016. ISSN 0001-1541. doi: https://doi.org/10.1002/aic.15076. URL https://aiche.onlinelibrary.wiley.com/doi/abs/10.1002/aic.15076.

[181] Y. Y. Zhao, Q. B. Yang, X. F. Lu, C. Wang, and Y. Wei. Study on correlation of morphology of electrospun products of polyacrylamide with ultrahigh molecular weight. *Journal of Polymer Science Part B: Polymer Physics*, 43(16):2190–2195, 2005. ISSN 0887-6266. doi: https://doi.org/10.1002/polb.20506. URL https://onlinelibrary.wiley.com/doi/abs/10.1002/polb.20506.

[182] A. Koski, K. Yim, and S. Shivkumar. Effect of molecular weight on fibrous pva produced by electrospinning. *Materials Letters*, 58(3):493–497, 2004. ISSN 0167-577X. doi: https://doi.org/10.1016/S0167-577X(03)00532-9. URL https://www.sciencedirect.com/science/article/pii/S0167577X03005329.

[183] Binbin Dong, Yehu Han, Ting Wang, Zhanwu Lei, Yawei Chen, Feihong Wang, Hamidreza Abadikhah, Sayed Ali Khan, Luyuan Hao, Xin Xu, Ruiguo Cao, Liangjun Yin, and Simeon Agathopoulos. Hard sioc microbeads as a high-performance lithium-ion battery anode. *ACS Applied Energy Materials*, 3(10):10183–10191, 2020. doi: 10.1021/acsaem.0c0191010.1021/acsaem.0c01910⟨/p⟩. URL https://doi.org/10.1021/acsaem.0c01910.

[184] Kamaruddin, D. Edikresnha, I. Sriyanti, M. M. Munir, and Khairurrijal. Synthesis of polyvinylpyrrolidone (pvp)-green tea extract composite nanostructures using electrohydrodynamic spraying technique. *IOP Conference Series: Materials Science and Engineering*, 202:012043, 2017. ISSN 1757-8981 1757-899X. doi: 10.1088/1757-899x/202/1/012043. URL http://dx.doi.org/10.1088/1757-899X/202/1/012043.

[185] Yan Zhang, Yongqiang Li, Jianzhong Shao, and Chao Zou. Fabrication of superhydrophobic fluorine-free films on cotton fabrics through plasma-induced grafting polymerization of 1,3,5,7-tetravinyl-1,3,5,7-tetramethylcyclotetrasiloxane. *Surface and Coatings Technology*, 276:16–22, 2015. ISSN 0257-8972. doi: https://doi.org/10.1016/j.surfcoat.2015.06.050. URL https://www.sciencedirect.com/science/article/pii/S0257897215300852.

[186] M. Naviroj, S. M. Miller, P. Colombo, and K. T. Faber. Directionally aligned macroporous sioc via freeze casting of preceramic polymers. *Journal of the European Ceramic Society*, 35(8):2225–2232, 2015. ISSN 0955-2219. doi: https://doi.org/10.1016/j.jeurceramsoc.2015.02.013. URL https://www.sciencedirect.com/science/article/pii/S0955221915000655.

[187] Jinwei Wang, Chaobin He, Yuhui Lin, and T. S. Chung. Studies on the thermal stability of f- and non-f-containing ladder polyepoxysilsesquioxanes by tga–ftir. *Thermochimica Acta*, 381(1):83–92, 2002. ISSN 0040-6031. doi: https://doi.org/10.1016/S0040-6031(01)00644-X. URL https://www.sciencedirect.com/science/article/pii/S004060310100644X.

[188] Lamuel David, Romil Bhandavat, Uriel Barrera, and Gurpreet Singh. Silicon oxycarbide glass-graphene composite paper electrode for long-cycle lithium-ion batteries. *Nature Communications*, 7(1):10998, 2016. ISSN 2041-1723. doi: 10.1038/ncomms10998. URL https://doi.org/10.1038/ncomms10998.

[189] Stéphanie Roualdes, René Berjoan, and Jean Durand. 29si nmr and si2p xps correlation in polysiloxane membranes prepared by plasma enhanced chemical vapor deposition. *Separation and Purification Technology*, 25(1):391–397, 2001. ISSN 1383-5866. doi: https://doi.org/10.1016/S1383-5866(01)00067-3. URL https://www.sciencedirect.com/science/article/pii/S1383586601000673.

[190] Beatriz Julián, Christel Gervais, Eloisa Cordoncillo, Purificación Escribano, Florence Babonneau, and Clément Sanchez. Synthesis and characterization of transparent pdmsmetal-oxo based organicinorganic nanocomposites. *Chemistry of Materials*, 15(15):3026–3034, 2003. ISSN 0897-4756. doi: 10.1021/cm031054l. URL https://doi.org/10.1021/cm031054l.

[191] R. K. Harris and M. L. Robins. 29si nuclear magnetic resonance studies of oligomeric and polymeric siloxanes: 4. chemical shift effects of end-groups. *Polymer*, 19(10):1123–1132, 1978. ISSN 0032-3861. doi: https://doi.org/10.1016/0032-3861(78)90057-5. URL https://www.sciencedirect.com/science/article/pii/0032386178900575.

[192] Ding-Shan Ruan, Ya-Li Li, Lei Wang, Dong Su, and Feng Hou. Fabrication of silicon oxycarbide fibers from alkoxide solutions along the sol–gel process. *Journal of Sol-Gel Science and Technology*, 56(2):184–190, 2010. ISSN 1573-4846. doi: 10.1007/s10971-010-2292-8. URL https://doi.org/10.1007/s10971-010-2292-8.

[193] Muhammad-Sadeeq Balogun, Weitao Qiu, Yang Luo, Hui Meng, Wenjie Mai, Amos Onasanya, Titus K. Olaniyi, and Yexiang Tong. A review of the development of full cell lithium-ion batteries: The impact of nanostructured anode materials. *Nano Research*, 9(10):2823–2851, 2016. ISSN 1998-0000. doi: 10.1007/s12274-016-1171-1. URL https://doi.org/10.1007/s12274-016-1171-1.

[194] Poonam, Kriti Sharma, Anmol Arora, and S. K. Tripathi. Review of supercapacitors: Materials and devices. *Journal of Energy Storage*, 21:801–825, 2019. ISSN 2352-152X. doi: https://doi.org/10.1016/j.est.2019.01.010. URL https://www.sciencedirect.com/science/article/pii/S2352152X18306339.

[195] Ander González, Eider Goikolea, Jon Andoni Barrena, and Roman Mysyk. Review on supercapacitors: Technologies and materials. *Renewable and Sustainable Energy Reviews*, 58:1189–1206, 2016. ISSN 1364-0321. doi: https://doi.org/10.1016/j.rser.2015.12.249. URL https://www.sciencedirect.com/science/article/pii/S1364032115016329.

[196] Tae Hoon Hwang, Yong Min Lee, Byung-Seon Kong, Jin-Seok Seo, and Jang Wook Choi. Electrospun core–shell fibers for robust silicon nanoparticle-based lithium ion battery anodes. *Nano Letters*, 12(2):802–807, 2012. ISSN 1530-6984. doi: 10.1021/nl203817r. URL https://doi.org/10.1021/nl203817r.

[197] Md. Arafat Rahman, Guangsheng Song, Anand I. Bhatt, Yat Choy Wong, and Cuie Wen. Nanostructured silicon anodes for high-performance lithium-ion batteries. *Advanced Functional Materials*, 26(5):647–678, 2016. ISSN 1616-301X. doi: https://doi.org/10.1002/adfm.201502959. URL https://onlinelibrary.wiley.com/doi/abs/10.1002/adfm.201502959.

[198] Xin Su, Qingliu Wu, Juchuan Li, Xingcheng Xiao, Amber Lott, Wenquan Lu, Brian W. Sheldon, and Ji Wu. Silicon-based nanomaterials for lithium-ion batteries: A review. *Advanced Energy Materials*, 4(1):1300882, 2014. ISSN 1614-6832. doi: https://doi.org/10.1002/aenm.201300882. URL https://onlinelibrary.wiley.com/doi/abs/10.1002/aenm.201300882.

[199] Wei Tao, Ping Wang, Ya You, Kyusung Park, Cao-Yu Wang, Yong-Ke Li, Fei-Fei Cao, and Sen Xin. Strategies for improving the storage performance of silicon-based anodes in lithium-ion batteries. *Nano Research*, 12(8):1739–1749, 2019. ISSN 1998-0000. doi: 10.1007/s12274-019-2361-4. URL https://doi.org/10.1007/s12274-019-2361-4.

[200] Fukui Hiroshi, Ohsuka Hisashi, Hino Takakazu, and Kanamura Kiyoshi. Preparation of microporous si–o–c composite material and its lithium storage capability. *Chemistry Letters*, 38(1):86–87, 2009. doi: 10.1246/cl.2009.86. URL https://www.journal.csj.jp/doi/abs/10.1246/cl.2009.86.

[201] Hiroshi Fukui, Hisashi Ohsuka, Takakazu Hino, and Kiyoshi Kanamura. A sioc composite anode: High capability and proposed mechanism of lithium storage associated with microstructural characteristics. *ACS Applied Materials Interfaces*, 2(4):998–1008, 2010. ISSN 1944-8244. doi: 10.1021/am100030f10.1021/am100030f⟨/p⟩. URL https://doi.org/10.1021/am100030f.

[202] J. Shen, D. Ahn, and R. Raj. C-rate performance of silicon oxycarbide anodes for li+ batteries enhanced by carbon nanotubes. *Journal of Power Sources*, 196(5):2875–2878, 2011. ISSN 0378-7753. doi: https://doi.org/10.1016/j.jpowsour.2010.11.009. URL https://www.sciencedirect.com/science/article/pii/S0378775310019130.

[203] Xiang Liu, Man-Chun Zheng, and Kai Xie. Mechanism of lithium storage in si–o–c composite anodes. *Journal of Power Sources*, 196(24):10667–10672, 2011. ISSN 0378-7753. doi: https://doi.org/10.1016/j.jpowsour.2011.08.072. URL https://www.sciencedirect.com/science/article/pii/S0378775311016181.

[204] Sabyasachi Sen, Scarlett J. Widgeon, Alexandra Navrotsky, Gabriela Mera, Amir Tavakoli, Emanuel Ionescu, and Ralf Riedel. Carbon substitution for oxygen in silicates in planetary interiors. *Proceedings of the National Academy of Sciences*, 110(40): 15904–15907, 2013. doi: 10.1073/pnas.1312771110. URL https://www.pnas.org/content/pnas/110/40/15904.full.pdf.

[205] Jan Kaspar, Magdalena Graczyk-Zajac, and Ralf Riedel. Lithium insertion into carbon-rich sioc ceramics: Influence of pyrolysis temperature on electrochemical properties. *Journal of Power Sources*, 244:450–455, 2013. ISSN 0378-7753. doi: https://doi.org/10.1016/j.jpowsour.2012.11.086. URL https://www.sciencedirect.com/science/article/pii/S0378775312017612.

[206] Pengpeng Lv, Hailei Zhao, Chunhui Gao, Zhihong Du, Jie Wang, and Xin Liu. Siox–c dual-phase glass for lithium ion battery anode with high capacity and stable cycling performance. *Journal of Power Sources*, 274:542–550, 2015. ISSN 0378-7753. doi: https://doi.org/10.1016/j.jpowsour.2014.10.077. URL https://www.sciencedirect.com/science/article/pii/S0378775314016863.

[207] Martin Halim, Chairul Hudaya, A. Young Kim, and Joong Kee Lee. Phenyl-rich silicone oil as a precursor for sioc anode materials for long-cycle and high-rate lithium ion batteries. *Journal of Materials Chemistry A*, 4(7):2651–2656, 2016. ISSN 2050-7488. doi: 10.1039/C5TA09973K. URL http://dx.doi.org/10.1039/C5TA09973K.

[208] Se Hun Lee, Changyong Park, Kwanghyun Do, and Heejoon Ahn. Maximizing the utilization of active sites through the formation of native nanovoids of silicon oxycarbide as anode materials in lithium-ion batteries. *Energy Storage Materials*, 35:130–141, 2021. ISSN 2405-8297. doi: https://doi.org/10.1016/j.ensm.2020.11.018. URL https://www.sciencedirect.com/science/article/pii/S240582972030430X.

[209] Jeffery R Dahn, Alf M Wilson, Weibing Xing, and Gregg A Zank. Electrodes for lithium ion batteries using polysilazanes ceramic with lithium, May 20 1997. US Patent 5,631,106.

[210] Jeffery Raymond Dahn, Katsuya Eguchi, Alf M Wilson, Weibing Xing, and Gregg Alan Zank. Electrodes for lithium ion batteries using polysiloxanes, October 20 1998. US Patent 5,824,280.

[211] Pedro E. Sanchez-Jimenez and Rishi Raj. Lithium insertion in polymer-derived silicon oxycarbide ceramics. *Journal of the American Ceramic Society*, 93(4): 1127–1135, 2010. ISSN 0002-7820. doi: https://doi.org/10.1111/j.1551-2916.2009.03539.x. URL https://ceramics.onlinelibrary.wiley.com/doi/abs/10.1111/j.1551-2916.2009.03539.x.

[212] Dongjoon Ahn and Rishi Raj. Cyclic stability and c-rate performance of amorphous sil-

icon and carbon based anodes for electrochemical storage of lithium. *Journal of Power Sources*, 196(4):2179–2186, 2011. ISSN 0378-7753. doi: https://doi.org/10.1016/j.jpowsour.2010.09.086. URL https://www.sciencedirect.com/science/article/pii/S0378775310016927.

[213] Magdalena Graczyk-Zajac, Dragoljub Vrankovic, Philipp Waleska, Christian Hess, Pradeep Vallachira Sasikumar, Stefan Lauterbach, Hans-Joachim Kleebe, and Gian Domenico Sorarù. The li-storage capacity of sioc glasses with and without mixed silicon oxycarbide bonds. *Journal of Materials Chemistry A*, 6(1):93–103, 2018. ISSN 2050-7488. doi: 10.1039/C7TA09236A. URL http://dx.doi.org/10.1039/C7TA09236A.

[214] Jan Kaspar, Magdalena Graczyk-Zajac, Soumyadip Choudhury, and Ralf Riedel. Impact of the electrical conductivity on the lithium capacity of polymer-derived silicon oxycarbide (sioc) ceramics. *Electrochimica Acta*, 216:196–202, 2016. ISSN 0013-4686. doi: https://doi.org/10.1016/j.electacta.2016.08.121. URL https://www.sciencedirect.com/science/article/pii/S0013468616318576.

[215] Magdalena Graczyk-Zajac, Lukas Mirko Reinold, Jan Kaspar, Pradeep Vallachira Warriam Sasikumar, Gian-Domenico Soraru, and Ralf Riedel. New insights into understanding irreversible and reversible lithium storage within sioc and sicn ceramics. *Nanomaterials*, 5(1):233–245, 2015. ISSN 2079-4991. URL https://www.mdpi.com/2079-4991/5/1/233.

[216] Seung-Ho Baek, Lukas Mirko Reinold, Magdalena Graczyk-Zajac, Ralf Riedel, Franziska Hammerath, Bernd Büchner, and Hans-Joachim Grafe. Lithium dynamics in carbon-rich polymer-derived sicn ceramics probed by nuclear magnetic resonance. *Journal of Power Sources*, 253:342–348, 2014. ISSN 0378-7753. doi: https://doi.org/10.1016/j.jpowsour.2013.12.065. URL https://www.sciencedirect.com/science/article/pii/S0378775313020430.

[217] Jan Kaspar, Magdalena Graczyk-Zajac, and Ralf Riedel. Carbon-rich sioc anodes for

lithium-ion batteries: Part ii. role of thermal cross-linking. *Solid State Ionics*, 225: 527–531, 2012. ISSN 0167-2738. doi: https://doi.org/10.1016/j.ssi.2012.01.026. URL https://www.sciencedirect.com/science/article/pii/S0167273812000392.

[218] K. SCHLADITZ. Quantitative micro-ct. *Journal of Microscopy*, 243(2):111–117, 2011. doi: https://doi.org/10.1111/j.1365-2818.2011.03513.x. URL https://onlinelibrary.wiley.com/doi/abs/10.1111/j.1365-2818.2011.03513.x.

[219] Yanjian Feng, Zude Feng, Siwei Li, Weihua Zhang, Xingan Luan, Yongsheng Liu, Laifei Cheng, and Litong Zhang. Micro-ct characterization on porosity structure of 3d cf/sicm composite. *Composites Part A: Applied Science and Manufacturing*, 42(11):1645–1650, 2011. ISSN 1359-835X. doi: https://doi.org/10.1016/j.compositesa.2011.07.015. URL https://www.sciencedirect.com/science/article/pii/S1359835X11002211.

[220] Yifu Ding, Daniel J Vanselow, Maksim A Yakovlev, Spencer R Katz, Alex Y Lin, Darin P Clark, Phillip Vargas, Xuying Xin, Jean E Copper, Victor A Canfield, Khai C Ang, Yuxin Wang, Xianghui Xiao, Francesco De Carlo, Damian B van Rossum, Patrick La Riviere, and Keith C Cheng. Computational 3d histological phenotyping of whole zebrafish by x-ray histotomography. *eLife*, 8:e44898, may 2019. ISSN 2050-084X. doi: 10.7554/eLife.44898. URL https://doi.org/10.7554/eLife.44898.

Appendix A

micro-CT of the CMCs

X-ray micro-computed tomography (micro-CT or µ-CT) imaging has become a standard tool to generate quantitative 3D images of an object. micro-CT is a non-destructive imaging technique that uses tomographic reconstruction from projection images to create a 3D image of the the sample[218]. X-rays emitted from an X-ray source pass through a sample and are recorded by a detector on the opposite side of the source to produce projection images as shown in Figure A.1. The sample is then rotated by a fraction of degree until the samples has rotated 180°or 360°and projection images are taken at every angle. The recorded projection images are then processed using a reconstruction algorithm to show the geometry and internal structure of the sample (Figure A.2). The versatility of micro-CT can be used to analyze the structure of the fabricated CMCs. Visualizing the complex 3D microstructure as well as the internal defects and damage of the CMCs provides insight for quality control and failure analysis[219].

An initial study on the fabricated CMC samples was conducted using an micro-CT. Figure A.3 shows the reconstructed 3D image of the Si(B)CN/CF CMC mini-composite. In the reconstructed cross-sections, the microstructure and internal porosity of the Si(B)CN/CF sample could be determined. The micro-CT images provided a visible distinction between the fibers and the matrix. Single fibers and pore sizes were also distinguishable in the image. The sectional view shows the distribution of fiber bundles in the XY-plane. Presence of

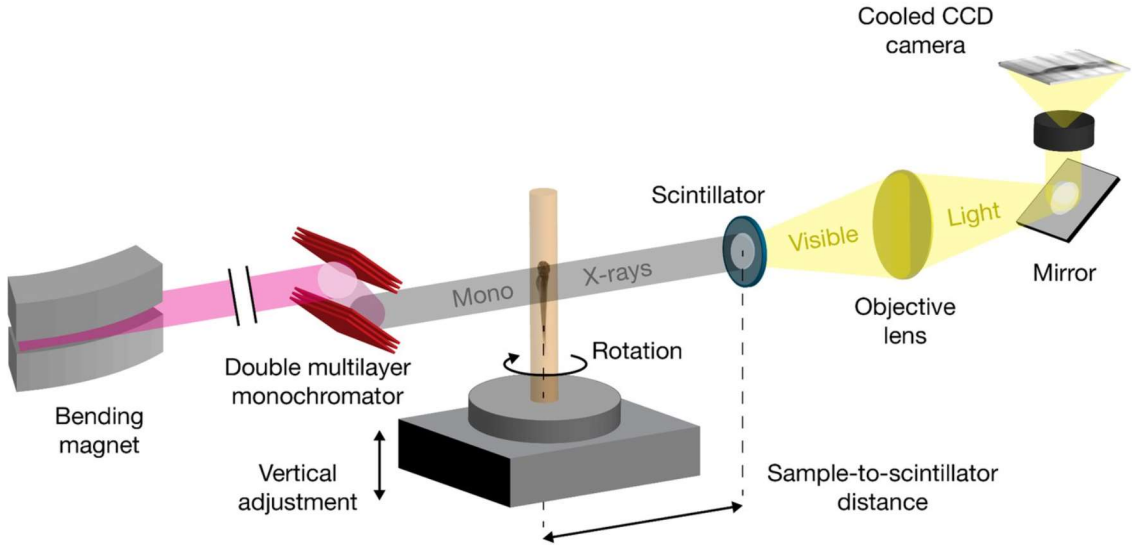

Figure A.1: *Schematic for synchrotron X-ray micro-tomography of an object. Reproduced with permission from*[220]*. Copyright 2019 eLife*

various sizes of porosity indicated the imhomogeneous distribution of matrix phase in the composite. Many cracks were also observed in the Si(B)CN matrix. These cracks were few micrometer in sizes and presumably formed due to the shrinkage of matrix and gas diffusion during pyrolysis process.

This initial study demonstrates that micro-CT can facilitate characterization of fiber morphology, density of matrix phases and defects in CMC composites. The relation of multiple polymer infiltration of composites with the matrix density and porosity can be determined using micro-CT. This knowledge can be used to correlate the effect of porsosity on the thermal and mechanical properties of CMCs. In addition, in-situ tensile testing setups with micro-CT have been reported in literature. This setup will allow for real time X-ray imaging of the samples under mechanical load in different environments such as temperatures greater than 1000 °C.

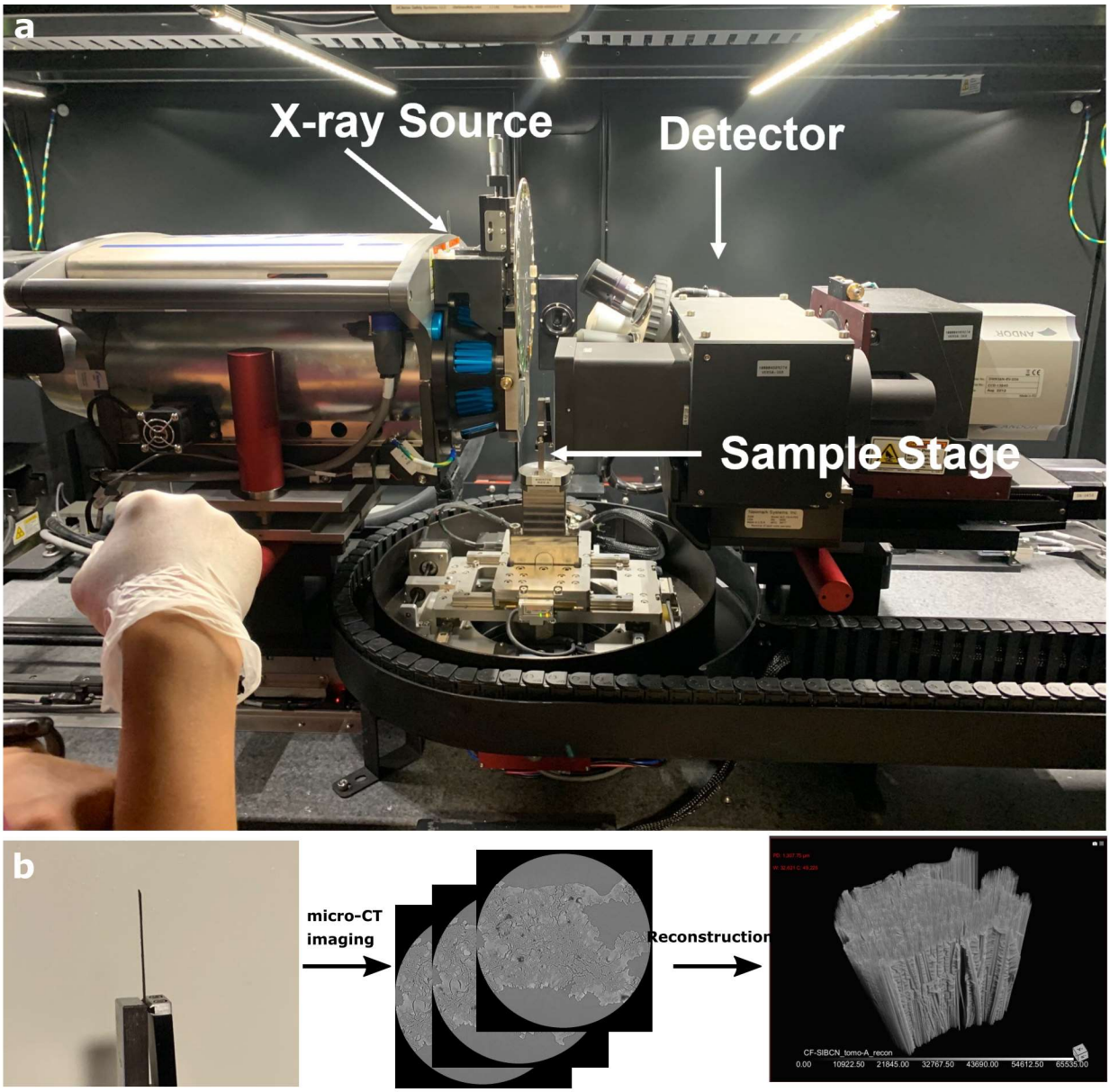

Figure A.2: *(a) A lab-based micro-CT equipment: Zeiss Versa Xradia 520. (b) Tomographic reconstruction of X-ray projection images to create a 3D image of the object.*

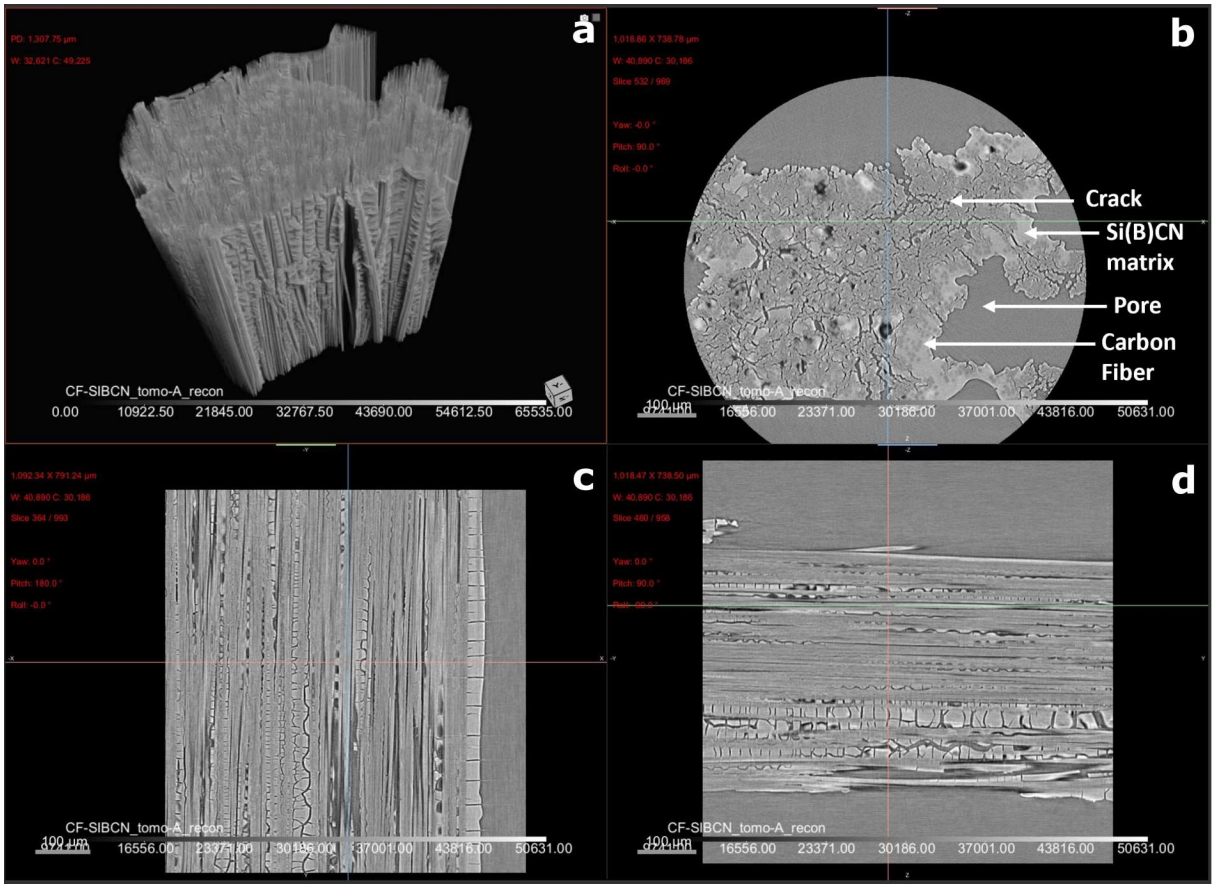

Figure A.3: *micro-CT scanning of the Si(B)CN/CF CMC mini-composite. (a) Stereogram, (b) cross-section, (c) longitudinal section and (d) oblique section.*